2009

Estimation of grid-induced errors in computational fluid dynamics solutions using a discrete error transport equation

Brandon Williams
Iowa State University

Estimation of grid-induced errors in computational fluid dynamics solutions using a discrete error transport equation

by

Brandon Riley Williams

A dissertation submitted to the graduate faculty

in partial fulfillment of the requirements for the degree of

DOCTOR OF PHILOSOPHY

Major: Aerospace Engineering

Program of Study Committee:
Tom I-P. Shih, Major Professor
Mark Bryden
Ambar Mitra
Thomas Rudolphi
Zhi J. Wang

Iowa State University

Ames, Iowa

2009

Table of Contents

List of Figures ..... **v**

List of Tables ..... **viii**

Abstract ..... **ix**

Chapter 1. Overview **1**

Introduction 1

Error-Estimation Methods 2

Classifications 2

Richardson Extrapolation 3

Adjoint Variable Method 4

Error Transport Equation Method 6

DETE Residual Modeling 8

Research Objective & Approach 9

Chapter 2. Navier-Stokes Finite Volume Scheme **10**

Navier-Stokes Equations 10

Finite Volume Formulation 11

Numerical Fluxes 11

Reconstruction 13

Time Integration 13

Boundary Conditions 14

No-slip Wall 14

Symmetry 15

Far Field 15

Verification of Numerical Accuracy 16

Isentropic Vortex 17

Poiseuille Flow 17

Chapter 3. DETE Finite Volume Scheme 19

DETE Equations 19

Linearization 19

Boundary Conditions 20

No-slip Wall 21

Symmetry 22

Far Field 22

Chapter 4. Validation of DETE Solutions 25

Steady Flow 25

Circular Cylinder 25

Transonic Airfoil 27

Unsteady Flow 28

Isentropic Vortex 29

Unsteady Circular Cylinder 30

Chapter 5. Residual Modeling 34

Approximate Modified Equation (AME) Model 38

PDE Model 40

Extrapolation Model 41

Chapter 6. Evaluation of Residual Models 43

Steady Flow 43

Circular Cylinder 43

Transonic Airfoil 55

Unsteady Flow 61

Isentropic Vortex 61

Unsteady Circular Cylinder 67

Chapter 7. Summary 71

Appendix A **74**

Appendix B **79**

References **81**

Acknowledgements **84**

List of Figures

Figure 2.1. Schematic of face neighbor cells; ● – cell centers; ■ – face center 12
Figure 4.1. Streamlines of steady laminar flow past a circular cylinder, $Re_D = 40$ 25
Figure 4.2. Grid 1 for steady cylinder Case 1 25
Figure 4.3. Comparison of DETE solution and actual error of x-momentum (kg/m-s) for steady cylinder Case 1 26
Figure 4.4. Grid 2D for steady cylinder Case 2 27
Figure 4.5. Comparison of DETE solution and actual error of x-momentum (kg/m-s) for steady cylinder Case 2 27
Figure 4.6. Contours of pressure for transonic airfoil at $\alpha = 1^{\circ}$ 28
Figure 4.7. Grid 1 for transonic airfoil problem 28
Figure 4.8. Comparison of DETE solutions and actual error of x-momentum (kg/m-s) for transonic airfoil problem 28
Figure 4.9. Comparison of DETE solutions and actual error of x-momentum (kg/m-s) for isentropic vortex problem 29
Figure 4.10. Contours of vorticity for $Re_D = 300$ flow past a circular cylinder 31
Figure 4.11. Grid 1 for unsteady cylinder problem 31
Figure 4.12. Comparison of DETE solution on Grid 1 and actual error of x-momentum (kg/m-s) relative to Grid 2 flow solution for unsteady cylinder problem 32
Figure 4.13. Comparison of time history of lift coefficient for unsteady cylinder problem 33
Figure 5.1. Residual of x-momentum for grid with localized defect 34
Figure 5.2. Error of x-momentum for grid with localized defect 34
Figure 5.3. Trends of residual magnitude vs. absolute value of error gradient for steady cylinder problem with uniformly refined grids 35
Figure 5.4. Trend of residual magnitude vs. absolute value of error gradient for steady cylinder problem with localized grid defect 35
Figure 5.5. Residual relative to a single level of refinement vs. grid spacing 37
Figure 5.6. Residual relative to finest grid vs. grid spacing 37
Figure 5.7. Schematic of face neighbor geometry for AME Model; ● – cell centers; ■ – face center 40
Figure 5.8. Computational stencils for least square polynomial fit 41
Figure 6.1. DETE solutions using AME residual model and actual error in x-momentum (kg/m-s) for steady cylinder problem 45

Figure 6.2. Pressure coefficient on surface of cylinder, DETE results on Grid 1 using AME residual model 46
Figure 6.3. Pressure coefficient on surface of cylinder, DETE results on Grid 2 using AME residual model 46
Figure 6.4. Pressure coefficient on surface of cylinder, DETE results on Grid 3 using AME residual model 47
Figure 6.5. DETE solutions using PDE residual model and actual error in x-momentum (kg/m-s) for steady cylinder problem....48
Figure 6.6. Pressure coefficient on surface of cylinder, DETE results on Grid 1 using PDE residual model 49
Figure 6.7. Pressure coefficient on surface of cylinder, DETE results on Grid 2 using PDE residual model 49
Figure 6.8. Pressure coefficient on surface of cylinder, DETE results on Grid 3 using PDE residual model 50
Figure 6.9. DETE solutions using extrapolation residual model and actual error in x-momentum (kg/m-s) for steady cylinder problem 51
Figure 6.10. Pressure coefficient on surface of cylinder, DETE results on Grid 2 using extrapolation residual model....52
Figure 6.11. Pressure coefficient on surface of cylinder, DETE results on Grid 3 using extrapolation residual model....52
Figure 6.12. Comparison of DETE solutions and actual error in x-momentum (kg/m-s) with various residual models along Y/D = 0 53
Figure 6.13. Comparison of DETE solutions and actual error in x-momentum (kg/m-s) with various residual models along transverse cuts through wake region....54
Figure 6.14. DETE solutions using AME residual model and actual error in x-momentum (kg/m-s) for transonic airfoil problem....56
Figure 6.15. Pressure coefficient on surface of airfoil, DETE results on Grid 1 using AME residual model 57
Figure 6.16. Pressure coefficient on surface of airfoil, DETE results on Grid 2 using AME residual model 57
Figure 6.17. Pressure coefficient on surface of airfoil, DETE results on Grid 3 using AME residual model 57

Figure 6.18. DETE solutions using PDE residual model and actual error in x-momentum (kg/m-s) for transonic airfoil problem....58
Figure 6.19. Pressure coefficient on surface of airfoil, DETE results on Grid 1 using PDE residual model....59
Figure 6.20. Pressure coefficient on surface of airfoil, DETE results on Grid 2 using PDE residual model....59
Figure 6.21. Pressure coefficient on surface of airfoil, DETE results on Grid 3 using PDE residual model....59
Figure 6.22. DETE solutions using extrapolation residual model and actual error in x-momentum (kg/m-s) for transonic airfoil problem....60
Figure 6.23. Pressure coefficient on surface of airfoil, DETE results on Grid 2 using extrapolation residual model....61
Figure 6.24. Pressure coefficient on surface of airfoil, DETE results on Grid 3 using extrapolation residual model....61
Figure 6.25. DETE solutions on Grid 1 using AME residual model and actual error in x-momentum (kg/m-s) for unsteady isentropic vortex problem....62
Figure 6.26. DETE solutions on Grid 2 using AME residual model and actual error in x-momentum (kg/m-s) for unsteady isentropic vortex problem....63
Figure 6.27. DETE solutions on Grid 1 using PDE residual model and actual error in x-momentum (kg/m-s) for unsteady isentropic vortex problem....64
Figure 6.28. DETE solutions on Grid 2 using PDE residual model and actual error in x-momentum (kg/m-s) for unsteady isentropic vortex problem....65
Figure 6.29. DETE solutions on Grid 2 using extrapolation residual model and actual error in x-momentum (kg/m-s) for unsteady isentropic vortex problem....66
Figure 6.30. DETE solutions on Grid 1 using AME residual model and actual error in x-momentum (kg/m-s) for unsteady cylinder problem....68
Figure 6.31. DETE solutions on Grid 1 using PDE residual model and actual error in x-momentum (kg/m-s) for unsteady cylinder problem....69
Figure 6.32. Time history of lift coefficient, DETE solutions on Grid 1 using AME and PDE residual models....70
Figure 6.33. Time history of lift coefficient, DETE solutions on Grid 2 using AME and PDE residual models....70

List of Tables

Table 2.1. Error norms and order of accuracy for isentropic vortex propagation problem 17
Table 2.2. Error norms and order of accuracy for Poiseuille flow problem 18

Abstract

Computational fluid dynamics (CFD) has become a widely used tool in research and engineering for the study of a wide variety of problems. However, confidence in CFD solutions is still dependent on comparisons with experimental data. In order for CFD to become a trusted resource, a quantitative measure of error must be provided for each generated solution. Although there are several sources of error, the effects of the resolution and quality of the computational grid are difficult to predict à priori. This grid-induced error is most often attenuated by performing a grid refinement study or using solution adaptive grid refinement. While these methods are effective, they can also be computationally expensive and even impractical for large, complex problems.

This work presents a method for estimating the grid-induced error in CFD solutions of the Navier-Stokes and Euler equations using a single grid and solution or a series of increasingly finer grids and solutions. The method is based on the discrete error transport equation (DETE), which is derived directly from the discretized PDE and provides a value of the error at every cell in the computational grid. The DETE is developed for two-dimensional, laminar Navier-Stokes and Euler equations within a generalized unstructured finite volume scheme, such that an extension to three dimensions and turbulent flow would follow the same approach.

The usefulness of the DETE depends on the accuracy with which the source term, the grid-induced residual, can be modeled. Three different models for the grid-induced residual were developed: the AME model, the PDE model, and the extrapolation model. The AME model consists of the leading terms of the remainder of a simplified modified equation. The PDE model creates a polynomial fit of the CFD solution and then uses the original PDE in differential form to calculate the residual. Both the AME and PDE are used with a single grid and solution. The extrapolation model uses a fine grid solution to calculate the grid-induced residual on the coarse grid and then extrapolates that residual back to the fine grid.

The DETE and residual models were then evaluated for four flow problems: (1) steady flow past a circular cylinder; (2) steady, transonic flow past an airfoil; (3) unsteady flow of an isentropic vortex; (4) unsteady flow past a circular cylinder with vortex shedding. Results demonstrate the fidelity of the DETE with each residual model as well as usefulness of the DETE as a tool for predicting the grid-induced error in CFD solutions.

Chapter 1. Overview

Introduction

Computational fluid dynamics (CFD) has become a prevalent tool in research and engineering applications for the study of a wide variety of flow problems. Due to continuing advancements in computational technology and algorithm development, it is possible to use CFD to model ever larger (e.g., whole aircraft) and more complex (e.g., multi-physics) flows. However, the confidence in computational models is still very much tied to comparison with experimental data. In order for CFD to become a useful and widely accepted tool for design and analysis, a quantitative measure of error must be provided for each generated solution.

The sources of error in CFD can be attributed to (1) inadequate modeling of the underlying physics or material properties of the problem; (2) insufficient information at the domain boundaries; (3) non-physical effects generated by the numerical method of solution; (4) poor-quality and/or low-resolution computational grids. The first three sources are well-documented for various governing equations, boundary conditions, and numerical schemes during the development and validation process. As with any other analysis tool, the end-user has no control of these limitations but must be knowledgeable of them in order to properly pose the problem to be studied. On the other hand, the quality and resolution of the computational grid are directly influenced by the experience of the user who generates it and can have large effects on the solution accuracy. The grid must be sufficiently fine to represent the geometry of the problem being studied, as well as allow the numerical scheme to resolve the physics of the governing equations. The geometric quality of the cells (i.e. skewness, aspect ratio, etc.) can also introduce error in the numerical solution. Therefore, if we accept the limitations of current CFD algorithms and models, it is especially important to minimize the grid-induced error in order to ensure the best possible solution.

The main types of numerical error are round-off and discretization errors [1]. Round-off error is the result of a limited number of significant digits available in computer memory and can be mitigated by ensuring that the numerical scheme is stable so that round-off errors do not grow as the solution proceeds. It is also common to use as many significant digits as possible (or is practical) and to normalize data in order to avoid creating round-off error during mathematical operations. Discretization error is defined as the difference between the exact solution to the original differential equation and the exact solution to the discretized equation for a given computational grid. Discretization error contains both the error due to the reformulation of the differential equation into a discretized form (i.e., the result of truncation error) and the grid-induced error. The grid-induced

error can be described as the difference between the grid-independent solution of the discretized equation and the solution on any given computational grid. While the grid-induced error will approach zero in the limit as the grid is continually refined, the truncation error may remain. To eliminate discretization error entirely, the numerical scheme must be both stable and consistent. In this case, in the limit as the grid spacing and time step approach zero, the discretization error will disappear.

Traditionally, attenuating the effects of grid-induced error has been accomplished through a grid-refinement study using r- and/or h-refinement methods. In r-refinement methods, the nodes of the computational cells are moved to increase resolution where necessary, keeping the overall number of degrees of freedom in the problem the same. The simplest r-refinement procedure treats the grid nodes as a system of linear springs, where the spring constants are often a function of the local flow solution and its gradients. When using h-refinement, existing cells are sub-divided in order to increase resolution, which in turn increases the number of degrees of freedom in the problem. Again, refinement takes place in cells which are typically "marked" as a function of local flow gradients. Both types of refinement may be performed globally or locally within the domain, but in either case, care must be taken to preserve the geometric quality of the grid. These methods can also be computationally intensive and may require several solutions to be generated in order to reach a grid-independent solution that minimizes grid-induced error. Often, especially for large, complex problems, time and computational resource limits restrict the use of grid refinement, making it infeasible to find a grid-independent solution. In this situation, it is especially important to have a measure of the solution accuracy.

Error-Estimation Methods

Classifications

Several researchers have developed different approaches to estimate the error present in CFD solutions. Roache [2] has reviewed and classified these methods into two categories: those based on multiple grids, and those based on a single grid. Methods based on multiple grids most commonly employ Richardson extrapolation [3-5], which requires multiple solutions to be generated on a series of increasingly finer grids (at least three). While these methods give very definitive and accurate information on the grid-induced error, they may become prohibitively expensive for large, complex problems.

Single-grid methods can further be subclassified as either algebraic or PDE. Algebraic methods have mostly been developed in relation to solution-adaptive grid refinement [6-13], and typically only consider gradients of the scalar fields (e.g., the second derivative of pressure or velocity scaled by the cell volume). Shih, et al. [14] and Gu, et al. [15,16] have also proposed grid quality measures that account for the vector and tensor nature of the flow field and link the solution to the geometry and size of cells in the grid.

Single-grid PDE methods, first proposed by Babuska, et al. [17,18], recognize that errors can be transported by advection and diffusion from the point where they are generated in the grid. Therefore, a transport equation for error was needed to describe the generation and evolution of errors. This error transport equation method is the subject of ongoing research and is the focus of the work presented here.

The following sections will outline the most prominent contemporary error estimation methods: Richardson extrapolation, the adjoint variable method, and the error transport equation method.

Richardson Extrapolation

As an error estimation method, Richardson extrapolation [19] exploits the monotone convergence behavior of smooth solutions to predict a refined solution based on at least two solutions on two grids, one fine and one coarse. For a problem domain represented by a grid Ω_h, where h is the characteristic length (i.e., grid spacing), the error, e_h, between the exact solution, Q, and the numerical solution, Q_h, may be represented as [3]:

$$e_h = Q - Q_h = a_1 h + a_2 h^2 + a_3 h^3 \ldots \tag{1.1}$$

The coefficients a_1, a_2, etc. are local functions of the coordinates, but are assumed to not depend on the grid spacing. For a solution in the asymptotic range, where the leading term dominates, the error can be expressed as

$$e_{\alpha h} = Q - Q_{\alpha h} = C\left(\alpha h\right)^P \tag{1.2}$$

where P is order of the discretization, α is the grid refinement factor, and C is a coefficient which may be a local function of the coordinates [3]. If solutions on two uniformly and successively coarser grids having grid spacing of $2h$ and $4h$ ($\alpha = 2$ and 4) are available, it is possible to solve for the three unknowns in Eq. (1.2):

$$P = \ln\left[\left(Q_{2h} - Q_{4h}\right)/\left(Q_h - Q_{2h}\right)\right]/\ln\left(2\right) \tag{1.3}$$

$$Q_{ext} = \left(2^P Q_h - Q_{2h}\right) \Big/ \left(2^P - 1\right) \tag{1.4}$$

$$C = \left(Q_{ext} - Q_h\right) \Big/ h^p \tag{1.5}$$

Here, Q_{ext} denotes the extrapolated estimate for the exact solution, Q. From Eq. (1.4), an estimate of the error can be written as

$$e_h = \frac{Q_h - Q_{2h}}{2^P - 1} \tag{1.6}$$

Although it is not strictly necessary to double the grid spacing for each successive grid, in practice, this method is used in order to simplify the grid generation as well as the Richardson extrapolation analysis.

The Richardson extrapolation method requires that the numerical solution be within the asymptotic range; that is, the solution must be monotonically approaching a unique solution. Therefore, the computational grid must still adequately resolve the flow characteristics in order to provide any meaningful error estimates. As noted previously, Richardson extrapolation provides accurate information about the error present in the numerical solution, but at least three solutions on sufficiently fine grids must be stored. For large, complex problems, the computational resources required may make this approach infeasible. If, however, the main interest of the problem is only a functional output of the solution, such as lift or drag, Richardson extrapolation can easily be applied to provide error estimation of the function using only that data. Another limitation is the manner in which the information about error is provided. The value of the error is given locally but does not provide any indication of how or where it is produced.

Adjoint Variable Method

More recently, the adjoint variable method has been presented as a sort of hybrid between multiple grid methods and single grid algebraic methods and has become popular as an error estimation and grid refinement tool. The adjoint variable method generally seeks to quantify the uncertainty in a functional output of the solution, such as lift or drag, rather than local values of error in the flow variables. These methods make use of the concept of duality, where an equivalent (adjoint) formulation of the primary flow problem is utilized. By using the dual problem, the error in the functional output of interest can be related to local errors of the primary flow solution through the adjoint variables. The following overview is based on a discrete approach to the adjoint variable method [12,20].

Consider a problem domain represented by grid Ω_H, where H is the characteristic length for the discretization (e.g. grid spacing), which is too coarse to generate a grid-independent solution, but still resolves most flow features. The functional output of interest is denoted by the integral quantity $f(Q)$ where Q is the exact solution to the system of PDEs that govern the flow problem. The approximation of this solution and integral on Ω_H is denoted by $f_H(Q_H)$. In addition, there exists a grid Ω_h which is created by uniformly subdividing each cell in Ω_H; however, no solution will be generated on this finer grid. Rather, the goal is to estimate the functional output on the finer grid, $f_h(Q_h)$. First, the functional output is expanded in a Taylor series about the coarse grid solution,

$$f_h\left(Q_h\right) = f_h\left(Q_h^H\right) + \left.\frac{\partial f_h}{\partial Q_h}\right|_{Q_h^H}\left(Q_h - Q_h^H\right) + \ldots \tag{1.7}$$

The quantity Q_h^H represents the coarse grid solution mapped onto the fine grid through some interpolation operator:

$$Q_h^H \equiv I_h^H Q_H \tag{1.8}$$

The interpolation operator, I_h^H, must be chosen carefully depending on the type of discretization used and the characteristics of the governing equations.

The nonlinear residual operator that represents the discretization of the governing equations on the fine grid is written as:

$$F_h\left(Q_h\right) = 0 \tag{1.9}$$

Linearizing this residual operator about the coarse grid solution,

$$F_h\left(Q_h\right) \approx F_h\left(Q_h^H\right) + \left.\frac{\partial F_h}{\partial Q_h}\right|_{U_h^H}\left(Q_h - Q_h^H\right) + \ldots \tag{1.10}$$

Isolating the $(Q_h - Q_h^H)$ term in Eq. (1.10) and substituting into Eq. (1.7) provides an approximation for the functional output on the fine grid:

$$f_h\left(Q_h\right) \approx f_h\left(Q_h^H\right) - \left(\Psi_h\big|_{Q_h^H}\right)^T F_h\left(Q_h^H\right) \tag{1.11}$$

Here, Ψ_h is the adjoint variable solution which satisfies the following relation,

$$\left[\left.\frac{\partial F_h}{\partial Q_h}\right|_{Q_h^H}\right]^T \Psi_h\big|_{Q_h^H} = \left(\left.\frac{\partial f_h}{\partial Q_h}\right|_{Q_h^H}\right)^T \tag{1.12}$$

In order to evaluate Eq. (1.11), the adjoint variable solution would need to be calculated on the fine grid. To avoid this expense, the fine grid adjoint variable solution is replaced by the interpolated coarse grid solution:

$$f_h\left(Q_h\right) \approx f_h\left(Q_h^H\right) - \left(\Psi_h^H\right)^T F_h\left(Q_h^H\right) \tag{1.13}$$

Again, the adjoint variable solution is mapped to the fine grid through an interpolation operator, Υ_h^H,

$$\Psi_h^H \equiv \Upsilon_h^H \Psi_H \tag{1.14}$$

where Ψ_H is obtained from the solution of the adjoint equations on the coarse grid:

$$\left[\frac{\partial F_H}{\partial Q_H}\right]^T \Psi_H = \left(\frac{\partial f_H}{\partial Q_H}\right)^T \tag{1.15}$$

Although the actual discretized flow equations are not solved on the fine grid, it *is* used to evaluate the functional output using the interpolated flow solution and adjoint solution, so there must be sufficient additional computational resources available to hold the fine grid geometric information. Another barrier to implementing this method with existing flow solvers is the requirement to compute the Jacobians of the residual and functional operators, which could be quite complicated and time consuming depending on the structure of the code.

In addition to providing an estimate of the error in the functional output, the adjoint variable solution may also be used for grid refinement. The local value of the adjoint variables have been used as a refinement indicator, since relatively large values have been associated with areas with high sensitivity to grid spacing [12].

Error Transport Equation Method

Babuska, et al. [17,18] first proposed a method for deriving equations to describe the generation and transport of error within a finite element framework. This approach was later applied to finite difference and finite volume methods by Ferziger [21], van Straalen, et al. [22], and Zhang, et al. [23,24]. To illustrate, consider a differential operator, L, which represents the governing equations operating on the exact solution, Q:

$$L\left(Q\right) = 0 \tag{1.16}$$

When an approximate solution, Q_h, produced on a grid with spacing h is substituted, it will produce a residual since it will not satisfy the original equations:

$$L(Q_h) = R \tag{1.17}$$

If the differential operator is linear, or linearized, then subtracting Eq. (1.17) from Eq. (1.16) yields the error transport equation,

$$L(e_h) = -R \tag{1.18}$$

where the error is defined as:

$$e_h \equiv Q - Q_h \tag{1.19}$$

Since the error is relative to the exact solution, the error transport equation can account for error generated by both the grid and the numerical scheme. Roache [2] and Qin and Shih [25] note that this method is only valid for finite expansion methods such as finite element and spectral methods. In finite volume and finite difference methods, the differential operator in Eq. (1.17) is replaced by a discrete operator, so subtracting Eq. (1.17) from Eq. (1.16) will not result in Eq. (1.18). Finite difference and finite volume methods can be unified with finite expansion methods in integral form using the method of weighted residuals; however, the differential form in Eq. (1.18) can only be recovered if the weighting function is continuous, as in finite expansion methods.

To address this inconsistency, Qin and Shih [25] take a slightly different approach that derives a set of discrete error transport equations (DETEs) directly from the discretized governing equations, with no regard to the original PDE. As a result, their method cannot account for the error due to the numerical scheme and only provides a measure of the grid-induced error. Instead of the differential operator, Eq. (1.16) can be written as a discrete operator, L_D, operating on a grid with grid spacing H, a time step Δt_H, and a solution obtained on that grid, Q_H,

$$L_D(Q_H, H, \Delta t_H) = 0 \tag{1.20}$$

If a solution from a finer grid, Q_h, is substituted, it will produce a residual because the solution does not satisfy the discretized equations on the coarser grid:

$$L_D(Q_h, H, \Delta t_H) = R_H^h \tag{1.21}$$

The subscript for the residual denotes that it is defined on the coarse grid, and the superscript denotes that it is the result of the fine grid solution. Subtracting Eq. (1.20) from Eq. (1.21) yields the DETE,

$$L_D(e_H, H, \Delta t_H) = R_H^h \tag{1.22}$$

where the error in this case is defined as:

$$e_H = Q_h - Q_H \tag{1.23}$$

In general, the error in Eq. (1.23) is only an estimate of the error for the solution Q_H. If the fine grid solution is a grid-independent solution, the predicted error will be the total grid-induced error. Furthermore, if the grid-independent solution converges to the exact solution for the problem, then the predicted error will also include the discretization error. In any case, the predicted error in Eq. (1.23) can be a useful tool in estimating the accuracy of a given solution as well as the sensitivity of the solution to changes in grid spacing.

Qin and Shih [25-30] showed their method to work well for a number of one-dimensional model equation problems, as well as the two-dimensional Euler equations. They also demonstrated the DETE derived for the Euler equations can predict the error for high Reynolds number viscous flows when properly modified [31], since convection dominates diffusion in these conditions.

DETE Residual Modeling

It is obvious from Eq. (1.22) that the error can be considered a direct function of the residual. If a fine grid solution is available, it is a simple exercise to produce the residual and solve for the error between the coarse grid and fine grid solutions. That fact becomes academic, however, since it would be simpler to difference the two solutions in order to obtain the error. Therefore, for the DETE method to be useful, it would be best to model the residual using a single solution, or if multiple solutions are available, the residual should be defined on the finest grid.

Zhang, et al. [23,24] based their residual model on a modified equation approach, which has been used to estimate the truncation error in classic CFD analysis, and applied it to hyperbolic conservation law equations in one dimension. The error solutions based on this residual model were shown to be inaccurate in regions of large error or large gradients. Celik and Hu [32] presented a general framework for calculating a similar residual, which makes use of the differencing inherent in any numerical scheme and does not require the modified equation to be worked out analytically – a major advantage since the modified equation is entirely dependent on the numerical scheme and can be quite complicated and tedious to derive. This approach showed the same accuracy problems when tested on several different model equations, however.

Shih and Qin [30] proposed a number of residual modeling approaches, including a variation of the modified equation. They also suggest using a higher-order solution in place of the fine grid solution and using a series of refined grids to extrapolate the residual on the finest grid. Most of these methods have not been fully tested.

An approach similar to the DETE, called the method of nearby problems, has recently been introduced by Roy, et al. [33-35]. Conceptually, the procedure of this method is to model the residual, then solve Eq. (1.21) for the fine grid solution using the coarse grid. Their residual model is an approximation to the truncation error (the difference between the original differential equation and the discretized version), which is essentially an evaluation of Eq. (1.17). First, they produce a continuous, multi-zone spline fit of the numerical solution. Then, the spline fit is inserted into the differential form of the original PDE, which yields the residual. Tests on a number of model equation problems, as well as incompressible Navier-Stokes solutions, have shown favorable results. However, the spline fit procedure can be problem dependent in terms of the number of zones required to accurately spline fit the solution and adds some additional complexity compared to other methods.

Research Objective & Approach

The remainder of this dissertation will focus on the research conducted on error estimation using a discrete error transport equation. The goals of this work are:

1. Develop a DETE-based method and code for estimating local values of error in CFD solutions of the Navier-Stokes and Euler equations. The method must be able to provide an estimate of the error in a solution generated on a single grid or in the solution obtained on the finest grid from a series of solutions on increasingly refined grids. This method must also be able to estimate the error in solutions of steady or unsteady flows.
2. Develop and evaluate methods to model residual in the DETE.
3. Demonstrate the usefulness of the DETE method and residual models for both steady and unsteady solutions of the Navier-Stokes and Euler equations.

To this end, a DETE method will be presented in the framework of an unstructured, finite volume scheme, and validated for accuracy. Without a loss of generality, the DETE will be derived for the two-dimensional, laminar Navier-Stokes equations; the Euler equations are obtained by simply eliminating the diffusion terms. The reduced complexity of this approach was chosen to provide a clear demonstration of the DETE, but an extension to three dimensions and turbulent flow would follow naturally. Three different residual models will then be discussed which make use of a single grid and solution, as well as multiple grids and solutions. Finally, these residual models will be evaluated for four different test problems: (1) steady, laminar flow past a circular cylinder; (2) steady, transonic, inviscid flow past an airfoil; (3) unsteady, inviscid flow of a passively convected vortex; (4) unsteady, laminar flow past a circular cylinder with vortex shedding.

Chapter 2. Navier-Stokes Finite Volume Scheme

This chapter presents the two-dimensional laminar Navier-Stokes equations discretized in a second-order-accurate unstructured finite volume scheme with explicit time stepping. Corresponding implementations are derived for no-slip wall, symmetry, and far field boundary conditions. Finally, the formal order of accuracy for the numerical scheme will be verified.

Navier-Stokes Equations

The continuity, momentum, and energy equations for two-dimensional, laminar, compressible flow of a calorically and thermally perfect gas can be written in conservation form as

$$\frac{\partial Q}{\partial t} + \nabla \bullet \boldsymbol{f} + \nabla \bullet \boldsymbol{g} = 0 \tag{2.1}$$

where,

$$Q = \begin{Bmatrix} \rho \\ \rho u \\ \rho v \\ E \end{Bmatrix} \tag{2.2}$$

$$\boldsymbol{f} = \begin{Bmatrix} \rho u \\ \rho u^2 + p \\ \rho uv \\ u\left(E + p\right) \end{Bmatrix} \hat{i} + \begin{Bmatrix} \rho v \\ \rho uv \\ \rho v^2 + p \\ v\left(E + p\right) \end{Bmatrix} \hat{j} \tag{2.3}$$

$$\boldsymbol{g} = -\mu \begin{Bmatrix} 0 \\ \tau_{xx} \\ \tau_{xy} \\ \tau_{xx}u + \tau_{xy}v - q_x \end{Bmatrix} \hat{i} - \mu \begin{Bmatrix} 0 \\ \tau_{yx} \\ \tau_{yy} \\ \tau_{yx}u + \tau_{yy}v - q_y \end{Bmatrix} \hat{j} \tag{2.4}$$

$$\tau_{xx} = \frac{4}{3}\frac{\partial u}{\partial x} - \frac{2}{3}\frac{\partial v}{\partial y}, \qquad \tau_{xy} = \tau_{yx} = \frac{\partial v}{\partial x} + \frac{\partial u}{\partial y}, \qquad \tau_{yy} = \frac{4}{3}\frac{\partial v}{\partial y} - \frac{2}{3}\frac{\partial u}{\partial x} \tag{2.5}$$

$$E = \frac{p}{\gamma - 1} + \frac{1}{2}\rho\left(u^2 + v^2\right), \qquad q = \frac{C_p}{\mathrm{Pr}}T \tag{2.6}$$

Here, ρ is density; p is pressure; u and v are x and y components of velocity, respectively. The heat transfer variable, q, is defined by Fourier's law using the specific heat at constant pressure, C_p, the

Prandtl number, *Pr*, and temperature, *T*. For this implementation, C_p, *Pr*, and the ratio of specific heats, γ, are assumed to be constant. The dynamic viscosity, μ, is calculated as a function of temperature according to Sutherland's model.

Finite Volume Formulation

Integrating Eq. (2.1) over arbitrary control volume *i* with volume, $\forall_i$,

$$\int_{\forall_i}\left(\frac{\partial Q}{\partial t}+\nabla\bullet\boldsymbol{f}+\nabla\bullet\boldsymbol{g}\right)d\forall=0 \tag{2.7}$$

Assuming the control volume does not change in time, and applying Gauss' theorem, Eq. (2.7) becomes:

$$\frac{\partial\bar{Q}_i}{\partial t}+\frac{1}{\forall_i}\oint_{S_i}\left(\boldsymbol{f}\bullet\hat{\boldsymbol{n}}+\boldsymbol{g}\bullet\hat{\boldsymbol{n}}\right)dS=0 \tag{2.8}$$

$$\bar{Q}_i=\frac{1}{\forall_i}\int_{\forall_i}Q\,d\forall \tag{2.9}$$

where *S* denotes the surface of the control volume and *n* is the surface normal vector. If the surface of the control volume is described by J_i number of faces, the surface integral in Eq. (2.8) can be written as a sum of the mean flux across each face,

$$\frac{\partial\bar{Q}_i}{\partial t}+\frac{1}{\forall_i}\sum_{j=1}^{J_i}\left(\bar{\boldsymbol{f}}_{i,j}+\bar{\boldsymbol{g}}_{i,j}\right)S_{i,j}=0 \tag{2.10}$$

$$\bar{\boldsymbol{f}}_{i,j}=\frac{1}{S_{i,j}}\int_{S_{i,j}}\left(\boldsymbol{f}\bullet\hat{\boldsymbol{n}}\right)dS \tag{2.11}$$

Eq. (2.10) is the finite volume form of the Navier-Stokes equations to be solved for each cell. For a finite volume scheme, the value of the conservative variable *Q* will always be referenced to the cell average value, so for convenience, the overbar denoting the average quantity will be dropped from here on.

Numerical Fluxes

Up to this point, the finite volume equations are still exact interpretations of the original PDE. In order to approximate the Riemann problem at each cell face, the inviscid fluxes are evaluated using a Rusanov flux formulation [36]. For first and second order accurate schemes, where *Q* is a constant or

linear function within each cell, the face mean flux is only required to be evaluated at the face center. Hence, the face mean inviscid flux can simply be written as:

$$\bar{\boldsymbol{f}}_{i,j} = \frac{1}{2}\left[\left(\boldsymbol{f}_L + \boldsymbol{f}_R \right) \bullet \hat{\boldsymbol{n}}_j - \left(\left| V_n \right| + a \right)_{avg} \left(Q_R - Q_L \right) \right] \tag{2.12}$$

Here, the subscripts L and R denote that the term is evaluated at the left or right state of the cell face center respectively, as defined by the face normal (see Figure 2.1). The quantity V_n is the velocity in the face normal direction, and a is the speed of sound. These values are averaged across the cell face.

The viscous fluxes at the face are calculated according to a method presented by Wang [37]. First, the solution gradients are found in the cell face tangent direction and the direction connecting the face neighbor cell centers:

$$\frac{dQ}{dm} = \frac{1}{2}\left[\nabla Q_L \cdot \hat{\boldsymbol{m}}_j + \nabla Q_R \cdot \hat{\boldsymbol{m}}_j \right], \qquad \frac{dQ}{d\ell} = \frac{Q_j - Q_i}{\left| \ell_j \right|} \tag{2.13}$$

The solution values and gradients at the face are then approximated as

$$Q_f = \frac{1}{2}\left(Q_L + Q_R \right), \qquad \nabla Q_f = \left(\frac{\frac{dQ}{d\ell} m_y - \frac{dQ}{dm} \ell_y}{m_y \ell_x - m_x \ell_y} \right) \hat{\boldsymbol{i}} + \left(\frac{\frac{dQ}{d\ell} m_x - \frac{dQ}{dm} \ell_x}{m_x \ell_y - m_y \ell_x} \right) \hat{\boldsymbol{j}} \tag{2.14}$$

The viscous flux is evaluated using the values from Eq. (2.14),

$$\bar{\boldsymbol{g}}_{i,j} = \boldsymbol{g}\left(Q_f, \nabla Q_f \right) \bullet \hat{\boldsymbol{n}}_j \tag{2.15}$$

For inviscid flow, the viscous fluxes are simply neglected from Eq. (2.10); the rest of the numerical scheme remains unchanged.

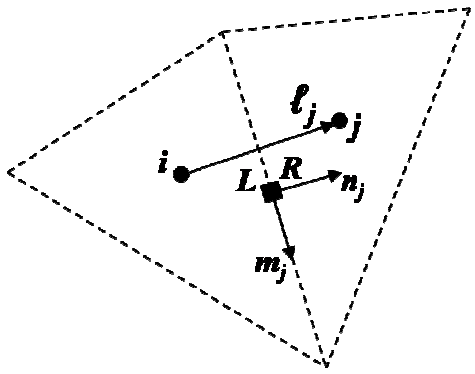

Figure 2.1. Schematic of face neighbor cells; ● – cell centers; ■ – face center

Reconstruction

For second-order spatial accuracy, this scheme calculates the gradients in each cell using a linear least squares reconstruction which is expanded about the cell center, see Appendix B. The reconstruction uses the cell average values of the conservative variables in each cell and its face neighbors. For a two-dimensional problem, the value of Q can then be calculated at any point within the cell according to the expression,

$$Q(x,y) = Q_i + b_i\left(x - x_i\right) + c_i\left(y - y_i\right) \tag{2.16}$$

where x_i and y_i are the coordinates of the cell center, and the coefficients are calculated by

$$b_i = \frac{1}{\psi}\left[I_{yy}\sum_{j=1}^{J_i}\left(Q_j - Q_i\right)\left(x_j - x_i\right) - I_{xy}\sum_{j=1}^{J_i}\left(Q_j - Q_i\right)\left(y_j - y_i\right)\right] \tag{2.17}$$

$$c_i = \frac{1}{\psi}\left[I_{xx}\sum_{j=1}^{J_i}\left(Q_j - Q_i\right)\left(y_j - y_i\right) - I_{xy}\sum_{j=1}^{J_i}\left(Q_j - Q_i\right)\left(x_j - x_i\right)\right] \tag{2.18}$$

$$I_{xx} = \sum_{j=1}^{J_i}\left(x_j - x_i\right)^2 \tag{2.19}$$

$$I_{yy} = \sum_{j=1}^{J_i}\left(y_j - y_i\right)^2 \tag{2.20}$$

$$I_{xy} = \sum_{j=1}^{J_i}\left(x_j - x_i\right)\left(y_j - y_i\right) \tag{2.21}$$

$$\psi = I_{xx}I_{yy} - I_{xy}^2 \tag{2.22}$$

For cells which contain one or more boundary faces, the reconstruction stencil includes ghost cells whose cell center is located by reflecting the boundary cell center across the boundary face. The conservative variable values for the ghost cells are calculated from imposed boundary conditions.

Time Integration

Equation (2.10) can be rewritten to define a residual operator, Γ,

$$\frac{\partial Q_i}{\partial t} = \Gamma_i\left(Q\right) \tag{2.23}$$

$$\Gamma_i\left(Q\right) = -\frac{1}{\forall_i}\sum_{j=1}^{J_i}\left\{\frac{1}{2}\left[\left(\boldsymbol{f}_L + \boldsymbol{f}_R\right)\bullet\hat{\boldsymbol{n}}_j - \left(\left|V_n\right| + a\right)_{avg}\left(Q_R - Q_L\right)\right] + \boldsymbol{g}\left(Q_f, \nabla Q_f\right)\bullet\hat{\boldsymbol{n}}_j\right\}S_{i,j} \tag{2.24}$$

For simplicity, the time derivative in Eq. (2.23) is approximated in an explicit fashion by a two-stage second-order-accurate Runge Kutta scheme:

$$\begin{aligned} Q_i^{(1)} &= Q_i^n + \Delta t_i \, \Gamma_i \left(Q^n \right) \\ Q_i^{n+1} &= \frac{1}{2} \left[Q_i^n + Q_i^{(1)} + \Delta t_i \, \Gamma_i \left(Q^{(1)} \right) \right] \end{aligned} \tag{2.25}$$

where the superscript n denotes the known time level data, $n+1$ is the time level sought, and (1) is an intermediate time step for numerical accuracy. The time step size is calculated as:

$$\Delta t_i = \left(CFL \right) \frac{\forall_i}{\sum_{j=1}^{J_i} \left(\left| V_n \right| + a \right)_j S_{i,j}} \tag{2.26}$$

The *CFL* number coefficient is used to under-relax the numerical scheme to improve stability, and its size is adjusted depending on the characteristics of the problem. For steady state problems, the local value of the time step is used, whereas for unsteady problems, the global minimum time step value is used for every cell.

Boundary Conditions

At any face which comprises part of a domain boundary, the grid convention is such that the normal points outward from the interior cell. Thus, the left state values of the conservative variables, Q_L, at the wall face are found by evaluating Eq. (2.16), which in turn are used to calculate the values of the primitive variables, $\rho_L, u_L, v_L, T_L,$ and p_L. These values yield the right state values through the imposition of the boundary condition and are then used to calculate the face mean flux. In order to find the cell average values for the boundary ghost cell, the boundary condition is simply applied to the cell average values of the interior cell.

No-slip Wall

The no-slip wall boundary condition is used to model walls where the normal and tangential velocity components at the wall are both zero. The right state values of the velocity components are the negative of the left state values, which enforces a zero velocity at the interface:

$$\left(u_R, v_R \right) = -\left(u_L, v_L \right) \tag{2.27}$$

The pressure boundary condition is a zero normal pressure gradient, $\partial p / \partial n = 0$, implemented as

$$p_R = p_L \tag{2.28}$$

The temperature boundary condition can either be modeled as an isothermal wall,

$$T_R = \text{constant} \tag{2.29}$$

or an adiabatic wall, $\partial T/\partial n = 0$,

$$T_R = T_L \tag{2.30}$$

Once these right state quantities are known, the right state density is calculated directly from the perfect gas equation,

$$\rho_R = p_R \Big/ \left(R_{gas} T_R \right) \tag{2.31}$$

Symmetry

The symmetry condition can be used to model either a symmetry plane or an inviscid wall. Flow tangency is enforced by reflecting the left state normal component of velocity at the right state such that the normal component of velocity is zero at the interface,

$$\begin{aligned} u_R &= u_L - 2\left(\boldsymbol{V}_L \bullet \hat{n}\right) n_x \\ v_R &= v_L - 2\left(\boldsymbol{V}_L \bullet \hat{n}\right) n_y \end{aligned} \tag{2.32}$$

The right state values of the density and pressure are set equal to the left state values to enforce zero normal gradients,

$$\rho_R = \rho_L \tag{2.33}$$

$$p_R = p_L \tag{2.34}$$

Far Field

The far field, or characteristic, boundary condition is used at boundaries far from any source of disturbance in the flow where $\mathrm{Re} \gg 1$ locally. In this case, the Navier-Stokes equations collapse to the Euler equations. A characteristic boundary condition neglects the influence of the face tangential flow and treats the boundary as a one-dimensional problem in the face normal direction. Integrating the compatibility equation for the one-dimensional problem along the characteristics (the eigenvalues of the Jacobian matrix, $\partial \boldsymbol{f}/\partial Q$) yields the Riemann invariants:

$$w_1 = \frac{p}{\rho^{\gamma}}, \qquad w_2 = V_n - \frac{2a}{\gamma - 1}, \qquad w_3 = V_n + \frac{2a}{\gamma - 1} \tag{2.35}$$

The Riemann invariants are used to set the boundary values of density, pressure, and the normal components of velocity. The tangential component of velocity is conserved across the boundary face.

Subsonic

For subsonic inflow, two invariants are specified from free stream flow conditions. In this case, w_1 and w_2 are specified because the face normal direction is outward (opposite the flow direction). The remaining invariant, w_3, is specified from the left state values from the interior cell. The right state primitives are then calculated by the following expressions:

$$\begin{aligned} a_R &= \tfrac{1}{4}(\gamma-1)(w_3 - w_2) \\ u_R &= \tfrac{1}{2}(w_2 + w_3)n_x + (\boldsymbol{V}_\infty \bullet \hat{\boldsymbol{m}})m_x \\ v_R &= \tfrac{1}{2}(w_2 + w_3)n_y + (\boldsymbol{V}_\infty \bullet \hat{\boldsymbol{m}})m_y \\ \rho_R &= \left(\frac{a_R^2}{\gamma\, w_1}\right)^{\left(1/\gamma-1\right)} \\ p_R &= w_1\, \rho_R^\gamma \end{aligned} \tag{2.36}$$

For an outflow boundary, the normal direction is aligned with flow, so w_2 is specified from free stream values, and w_1 and w_3 are calculated from interior cell values. The equations to find the right state values of the primitives remain the same.

Supersonic

For supersonic inflow, all invariants are specified by the free stream conditions. Thus, the right state conservative variables are also defined by the free stream:

$$Q_R = Q_\infty \tag{2.37}$$

At a supersonic outflow boundary, the invariants are all defined by the left state values. The right state values are then simply extrapolated from the internal cell:

$$Q_R = Q_L \tag{2.38}$$

Verification of Numerical Accuracy

The numerical scheme outlined here has been designed to have second-order spatial accuracy. This section will present two test problems to verify the order of accuracy of the implemented finite volume scheme for both inviscid and laminar flow.

Isentropic Vortex

First, the passive convection of an isentropic vortex in an inviscid flow is investigated. The domain is a square [0,10] by [0,10], with a non-dimensional mean flow $(u,v) = (1,1)$, $p = \rho = T = 1$, and characteristic boundaries on all sides. The isentropic vortex is initiated with its center at (xc,yc) = (5,5) as perturbations to the mean flow given by:

$$\begin{aligned}(\delta u, \delta v) &= \frac{\beta}{2\pi}\exp\left(\frac{1-r^2}{2}\right)(-\eta,\xi)\\ \delta T &= -\frac{(\gamma-1)\beta}{8\gamma\pi^2}\exp\left(1-r^2\right)\\ r^2 &= \xi^2+\eta^2\\ (\xi,\eta) &= (x,y)-(xc,yc)\end{aligned} \tag{2.39}$$

The vortex strength for this problem was set to $\beta = 5.0$. This problem is time dependant, so the solution was calculated up to $t = 2.0$ and compared with the exact solution in order to verify the order of accuracy. The L_1 and L_∞ norms of the error in u and the associated orders of accuracy are given for a series of four uniformly refined grids in Table 2.1. The second order of accuracy is verified by both the L_1 and L_∞ error for this problem.

Grid Size	L_1 Error	L_1 Order	L_∞ Error	L_∞ Order
20x20	6.83E-003	----	1.45E-001	----
40x40	1.52E-003	2.17	3.02E-002	2.26
80x80	2.84E-004	2.42	6.04E-003	2.32
160x160	5.73E-005	2.31	1.18E-003	2.35

Table 2.1. Error norms and order of accuracy for isentropic vortex propagation problem

Poiseuille Flow

The second problem studied is laminar Poiseuille flow at $Re_D = 1000$ with adiabatic walls. The domain is set to [0,5] by [0,0.5] with a plane of symmetry at $y = 0.5$. In this case, the inflow and outflow boundaries are set to the exact incompressible flow solution, which is described by the following relations:

$$\frac{\partial p}{\partial x} = \text{constant}, \quad \frac{\partial p}{\partial y} = 0$$
$$u = \frac{1}{2\mu}\left(\frac{\partial p}{\partial x}\right)\left(y^2 - Dy\right) \tag{2.40}$$

where D is the representative diameter of the channel.

Steady state solutions were calculated for a series of four uniformly refined grids and compared with the exact solution. The L_1 and L_∞ norms of the error in u and the orders of accuracy are given in Table 2.2. There is a slight loss of accuracy compared to results of the previous problem which may be attributed to the difficulty in achieving a converged solution to this incompressible problem with a compressible formulation. However, the order of the scheme does trend toward full second order accuracy as the grid is refined.

Grid Size	L_1 Error	L_1 Order	L_∞ Error	L_∞ Order
10x10	1.90E-002	----	4.11E-002	----
20x20	6.44E-003	1.57	1.48E-002	1.47
40x40	1.57E-003	2.04	4.19E-003	1.82
80x80	3.61E-004	2.12	9.26E-004	2.18

Table 2.2. Error norms and order of accuracy for Poiseuille flow problem

Chapter 3. DETE Finite Volume Scheme

This chapter will describe how the finite volume scheme developed for the Navier-Stokes equations in the previous chapter is modified to represent the DETE. This includes the linearization of the residual operator in Eq. (2.23), and derivation of the boundary conditions for the error variables which correspond to the boundary conditions for the flow variables.

DETE Equations

Since the DETE is based on the discretized flow equations, the strategy for implementation and solution is nearly identical. Recall from Chapter 1 that the discrete operator, L_D, must be linear. In this case, the residual operator defined in Eq. (2.23) contains non-linear terms in the form of the face mean fluxes. These terms must be linearized in order to make the DETE, Eq. (1.22), valid.

Linearization

The face mean fluxes in Eq. (2.10) are linearized by Taylor series expansion with respect to a coarse grid solution, denoted by the subscript H. The linearized fluxes for an arbitrary solution Q are approximated as:

$$\tilde{\boldsymbol{f}} = \boldsymbol{f}\left(Q_H\right) + \left.\frac{\partial \boldsymbol{f}}{\partial Q}\right|_{Q_H} \left(Q - Q_H\right) \tag{3.1}$$

$$\tilde{\boldsymbol{g}} = \boldsymbol{g}\left(Q_H\right) + \left.\frac{\partial \boldsymbol{g}}{\partial Q}\right|_{Q_H} \left(Q - Q_H\right) + \left.\frac{\partial \boldsymbol{g}}{\partial \nabla Q}\right|_{Q_H} \left(\nabla Q - \nabla Q_H\right) \tag{3.2}$$

The convection, diffusion, and diffusion gradient Jacobian matrices in Eq. (3.2) are provided in Appendix A. Substituting these expressions into Eq. (2.24) yields the linearized residual operator:

$$\tilde{\Gamma}_i\left(Q\right) = -\frac{1}{\forall_i}\sum_{j=1}^{J_i}\left\{\frac{1}{2}\left[\left(\tilde{\boldsymbol{f}}_L + \tilde{\boldsymbol{f}}_R\right)\bullet\hat{\boldsymbol{n}}_j - \left(\left|V_n\right| + a\right)_{avg}\Big|_{Q_H}\left(Q_R - Q_L\right)\right] + \tilde{\boldsymbol{g}}\left(Q_f, \nabla Q_f\right)\bullet\hat{\boldsymbol{n}}_j\right\}S_{i,j} \tag{3.3}$$

The linear operator on the coarse grid can now be defined as:

$$L_D\left(Q, H, \Delta t_H\right) = \frac{\partial Q}{\partial t} - \tilde{\Gamma}\left(Q\right) = 0 \tag{3.4}$$

Rewriting Eq. (1.22) using the linear operator forms the DETE,

$$\frac{\partial e_H}{\partial t} - \tilde{\Gamma}\left(e_H\right) = R_H^h \tag{3.5}$$

Note that the first term of the expansions in the linearized fluxes will drop out when subtracting Eq. (1.20) from Eq. (1.21). The linearized residual operator is simplified in this case, and can be written as,

$$\tilde{\Gamma}_i\left(e_H\right) = -\frac{1}{\forall_i}\sum_{j=1}^{J_i}\left\{\frac{1}{2}\left[\left(\tilde{\boldsymbol{f}}_L^e + \tilde{\boldsymbol{f}}_R^e\right)\bullet\hat{\boldsymbol{n}}_j - \left(\left|V_n\right| + a\right)_{avg}\Big|_{Q_H}\left(e_R - e_L\right)\right] + \tilde{\boldsymbol{g}}^e\left(e_f, \nabla e_f\right)\bullet\hat{\boldsymbol{n}}_j\right\}S_{i,j} \quad (3.6)$$

where the fluxes are now defined for the error variables, denoted by the superscript *e*. Substituting the definition of the error, Q_h - Q_H, into Eqs. (3.1) and (3.2) yields the error fluxes:

$$\tilde{\boldsymbol{f}}^e = \frac{\partial \boldsymbol{f}}{\partial Q}\Big|_{Q_H} e_H \quad (3.7)$$

$$\tilde{\boldsymbol{g}}^e = \frac{\partial \boldsymbol{g}}{\partial Q}\Big|_{Q_H} e_H + \frac{\partial \boldsymbol{g}}{\partial \nabla Q}\Big|_{Q_H} \nabla e_H \quad (3.8)$$

Since it is based on the discretized flow equations, the approach for solving the DETE is the same. The reconstruction of the error variables uses the same linear least squares method outlined previously. The time step is calculated by evaluating Eq. (2.26) with the flow variables from the coarse grid solution.

The DETE is solved on the coarse grid, using the coarse grid flow solution, and does not require any information from a more refined grid or solution, provided the residual can be adequately modeled. Also, because of the similarity to the Navier-Stokes scheme, the DETE can be implemented very efficiently. The main expense of the DETE formulation is the calculation of the flux Jacobians, although these would already be available if an implicit scheme were used for the flow solution.

Boundary Conditions

The DETE requires the boundary conditions derived for the flow problem to be modified. This section describes the error boundary conditions corresponding to no-slip wall, symmetry, and far field boundary conditions. The same system of left state, right state, and ghost cell values used in the flow problem is used for the error variables.

Since the flow boundary conditions are defined in terms of the flow primitive variables, the error boundary conditions must also be defined in terms of the error in these variables. The error in u, v, p, a, and T are calculated using the coarse grid flow primitives:

$$e_u = \frac{\left(e_{\rho u} - u e_\rho\right)}{\left(\rho + e_\rho\right)} \tag{3.9}$$

$$e_v = \frac{\left(e_{\rho v} - v e_\rho\right)}{\left(\rho + e_\rho\right)} \tag{3.10}$$

$$e_p = \left(\gamma - 1\right)\left\{e_E - \frac{1}{2}\left[e_{\rho u} e_u + \left(\rho u\right) e_u + e_{\rho v} e_v + \left(\rho v\right) e_v + u e_\rho + v e_{\rho v}\right]\right\} \tag{3.11}$$

$$e_a = \left[\frac{\gamma\left(p + e_p\right)}{\left(\rho + e_\rho\right)}\right]^{1/2} - a \tag{3.12}$$

$$e_T = \frac{e_p R_{gas}^{-1} - T e_\rho}{\rho + e_\rho} \tag{3.13}$$

No-slip Wall

At a no-slip wall, the flow velocity is specified, so the error in the velocity components must be zero at the interface. Hence, the right state values of the velocity error components are reflected:

$$\left(e_u\right)_R = -\left(e_u\right)_L \tag{3.14}$$

$$\left(e_v\right)_R = -\left(e_v\right)_L \tag{3.15}$$

The zero normal pressure gradient also results in a zero normal gradient for the error in pressure,

$$\left(e_p\right)_R = \left(e_p\right)_L \tag{3.16}$$

Likewise, an adiabatic wall will create a zero normal gradient for the error in temperature,

$$\left(e_T\right)_R = \left(e_T\right)_L \tag{3.17}$$

For an isothermal wall, the right state temperature is constant, so the right state error in temperature is simply zero. Using these conditions, the right state values of the error in the conservative variables can then be evaluated,

$$\left(e_\rho\right)_R = \left[\frac{e_p R_{gas}^{-1} - \rho e_T}{T + e_T}\right]_R \tag{3.18}$$

$$\left(e_{\rho u}\right)_R = \left[\rho e_u + \left(e_u + u\right) e_\rho\right]_R \tag{3.19}$$

$$\left(e_{\rho v}\right)_R = \left[\rho e_v + \left(e_v + v\right) e_\rho\right]_R \tag{3.20}$$

$$\left(e_E\right)_R = \frac{\left(e_p\right)_R}{\gamma - 1} + \frac{1}{2}\left[\left(\rho u + e_{\rho u}\right) e_u + \left(\rho v + e_{\rho v}\right) e_v + u e_{\rho u} + v e_{\rho v}\right]_R \tag{3.21}$$

Symmetry

The flow tangency condition requires zero velocity in the normal direction at the boundary face; it follows that there should also be zero error in the normal component of velocity. The right state values of the error in the velocity components are calculated as:

$$\left(e_u\right)_R = \left(e_u\right)_L - 2\left[e_u n_x + e_v n_y\right]_L n_x \tag{3.22}$$

$$\left(e_v\right)_R = \left(e_v\right)_L - 2\left[e_u n_x + e_v n_y\right]_L n_y \tag{3.23}$$

The right state errors in density and velocity are set equal to the left state values, satisfying the zero normal gradient imposed on the corresponding primitive variables,

$$\left(e_\rho\right)_R = \left(e_\rho\right)_L \tag{3.24}$$

$$\left(e_p\right)_R = \left(e_p\right)_L \tag{3.25}$$

The remaining errors in the conservative variables are found by evaluating Eqs. (3.19) - (3.21).

Far Field

The error far field boundary conditions make use of the errors in the Riemann invariants, which are:

$$e_{w1} = \frac{p + e_p}{\left(\rho + e_\rho\right)^\gamma} - w_1 \qquad e_{w2} = e_u n_x + e_v n_y - \frac{2e_a}{\gamma - 1} \qquad e_{w3} = e_u n_x + e_v n_y + \frac{2e_a}{\gamma - 1} \tag{3.26}$$

Subsonic

For subsonic inflow, the w_1 and w_2 invariants are specified by the free stream conditions, which implies the error in these invariants is zero. The error in the w_3 invariant is calculated from the left state values, and the right state values of the error in the primitive variables are:

$$\left(e_a\right)_R = \frac{1}{4}\left(\gamma - 1\right)\left(e_{w3}\right)_L \tag{3.27}$$

$$\left(e_u\right)_R = \frac{1}{2}\left(e_{w3}\right)_L n_x \tag{3.28}$$

$$\left(e_v\right)_R = \frac{1}{2}\left(e_{w3}\right)_L n_y \tag{3.29}$$

$$\left(e_\rho\right)_R = \left(\frac{1}{\gamma w_1}\right)^{1/\gamma - 1}\left[\left(e_a + a\right)^{2/\gamma - 1} - a^{2/\gamma - 1}\right]_R \tag{3.30}$$

$$\left(e_p\right)_R = w_1\left[\left(\rho + e_\rho\right)^\gamma - \rho^\gamma\right]_R \tag{3.31}$$

As before, the right state errors in the conservative variables are then constructed by evaluating Eqs. (3.19) - (3.21). At an outflow boundary, the w_2 invariant is specified by the free stream conditions, so it follows that e_{w2} is zero. The w_1 and w_3 invariants and their errors are calculated from the left state values, and the right state errors in the primitive variables are:

$$\left(e_u\right)_R = \frac{1}{2}e_{w3}n_x + \left(e_u m_x + e_v m_y\right)_L m_x \tag{3.32}$$

$$\left(e_v\right)_R = \frac{1}{2}e_{w3}n_y + \left(e_u m_x + e_v m_y\right)_L m_y \tag{3.33}$$

$$\left(e_\rho\right)_R = \left[\frac{\left(a + e_a\right)_R^2}{\gamma\left(w_1 + e_{w1}\right)}\right]^{1/\gamma - 1} - \left[\frac{a_R}{\gamma w_1}\right]^{1/\gamma - 1} \tag{3.34}$$

$$\left(e_p\right)_R = \left(w_1 + e_{w1}\right)\left(\rho + e_\rho\right)_R^\gamma - w_1\rho_R^\gamma \tag{3.35}$$

Supersonic

At supersonic boundaries, the invariants are always specified by upstream values. Therefore, at an inflow boundary, where the right state values are defined by the free stream conditions, the right

state error in the conservative variables is zero. The outflow boundary simply extrapolates the error in the conservative variables from the interior boundary cell,

$$e_R = e_L \tag{3.36}$$

Chapter 4. Validation of DETE Solutions

Although the accuracy of the numerical scheme has been verified, the ability of the DETE to solve for the error, $e_H = Q_h - Q_H$, using the exact residual, R_H^h, has not yet been demonstrated. This chapter presents four test problems which will be used to evaluate the accuracy of the DETE solutions. These problems will be tested with multiple grids with several levels of refinement as well as manufactured grid defects in order to illustrate the robustness of the method.

Steady Flow

Circular Cylinder

The problem of steady laminar flow past a circular cylinder (hereafter referred to as steady cylinder) is studied here. The flow has $Re_D = 40$, $T_\infty = 300$ K, and $M_\infty = 0.3$ in order to achieve better convergence with the given compressible finite volume scheme. Adiabatic, no-slip wall conditions are used at the cylinder surface, and characteristic boundaries are used at the far field. These flow conditions produce a stable recirculation zone which extends approximately two diameters downstream of the cylinder, as shown in Figure 4.1. All grids are circular, with the far field located fifteen cylinder diameters from the cylinder surface. Two cases are presented: (1) a series of uniformly refined grids and (2) a single grid with and without a localized defect.

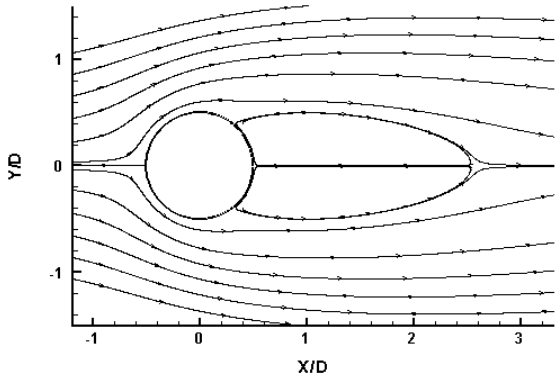

Figure 4.1. Streamlines of steady laminar flow past a circular cylinder, $Re_D = 40$

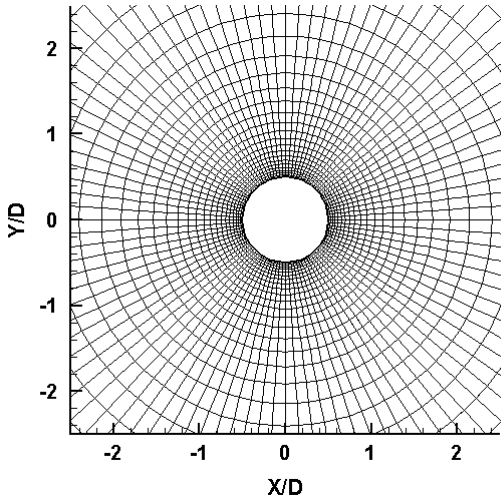

Figure 4.2. Grid 1 for steady cylinder Case 1

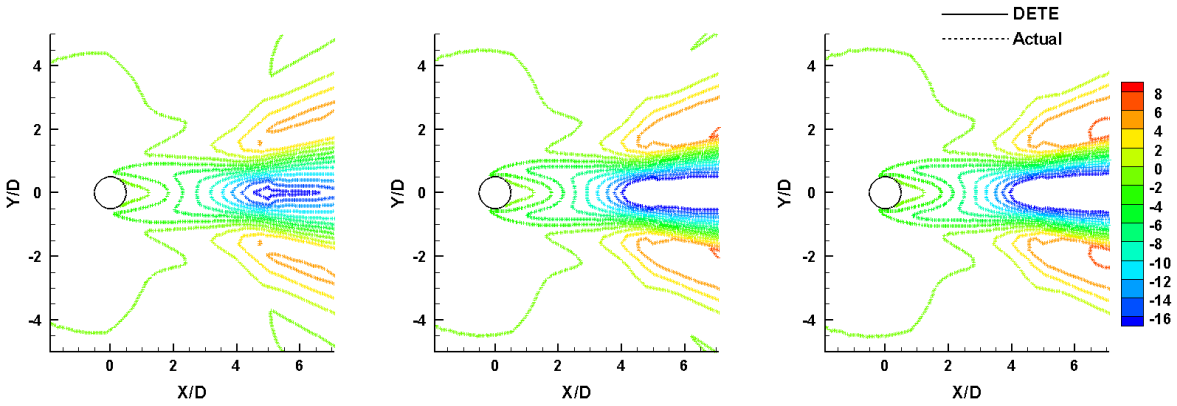

(a) Grid 2 - Grid 1 **(b) Grid 3 - Grid 1** **(c) Grid 4 - Grid 1**

Figure 4.3. Comparison of DETE solution and actual error of x-momentum (kg/m-s) for steady cylinder Case 1

Case 1 uses four grids, which are successively and uniformly refined from the base grid, Grid 1, shown in Figure 4.2. Grids 1 through 4 contain 3,250, 13,000, 52,000, and 208,000 cells respectively. The error on Grid 1 was solved using the DETE with three different residuals resulting from the flow solutions on Grids 2 through 4. A comparison of these DETE solutions with the actual error (found by subtracting the two flow solutions) for the x-momentum conserved variable is shown in Figure 4.3. The contour lines of each DETE solution lie on top of the actual error contours, which indicates the DETE has accurately solved for the error between the two given flow solutions, even where there are multiple levels of refinement between the grids. It should be noted, however, the fine grid solutions have been integrated over the fine grid cells contained in each coarse grid cell in order to be represented on the coarse grid. This procedure produces the correct cell average value on the coarse grid but may cause a loss of detail in the fine grid solution.

For Case 2, Grid 2 from Case 1 is locally coarsened to create a grid defect downstream of the cylinder in an area that interacts with the recirculation zone. This grid is labeled as Grid 2D in Figure 4.4. The DETE is solved on Grid 2D, using the flow solution on Grid 2D with a residual resulting from the solution on Grid 2. The DETE solution is compared with the actual error in the x-momentum in Figure 4.5. Again, the DETE solution agrees well with the actual error, even though the error solution is generated on an imperfect grid. Since the only difference between the two grids is the localized defect, this case also demonstrates how the error is generated at the defect and is then transported by the flow through the DETE.

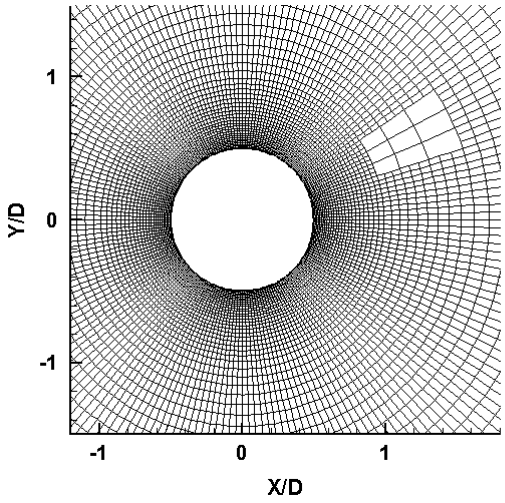

Figure 4.4. Grid 2D for steady cylinder Case 2

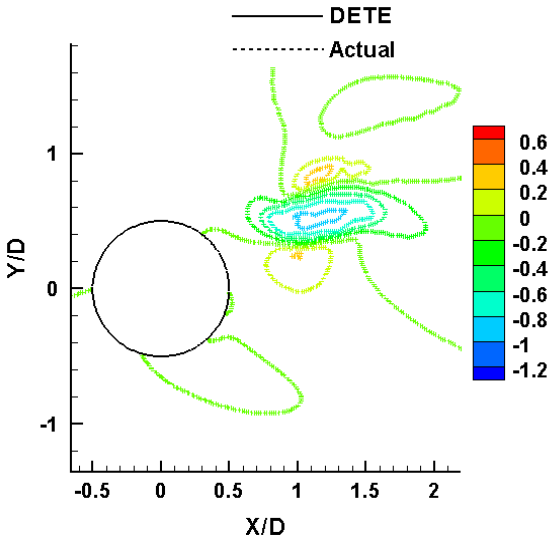

Figure 4.5. Comparison of DETE solution and actual error of x-momentum (kg/m-s) for steady cylinder Case 2

Transonic Airfoil

The next problem is steady, transonic, inviscid flow past a symmetric NACA0012 airfoil (referred to as transonic airfoil). The free stream flow conditions are $M_\infty = 0.85$ and $\alpha = 1^\circ$, which results in a strong shock forming above the airfoil near the 80% chord position, and a weaker shock below near the 60% chord position, as illustrated by the contours of pressure in Figure 4.6. The airfoil surface is represented by a symmetry condition; the far field, located fifteen chord lengths from the airfoil, uses characteristic boundary conditions. Again, a series of four grids are used which are uniformly refined from the base grid, Grid 1, shown in Figure 4.7. Grids 1 through 4 contain 1,800, 7,200, 28,800, and 115,200 cells respectively. The DETE solutions on Grid 1 which were generated by using residuals resulting from flow solutions on Grids 2 through 4 are compared with the actual error of x-momentum in Figure 4.8. In spite of the strong gradients surrounding the shock, the DETE solution matches the actual error very well.

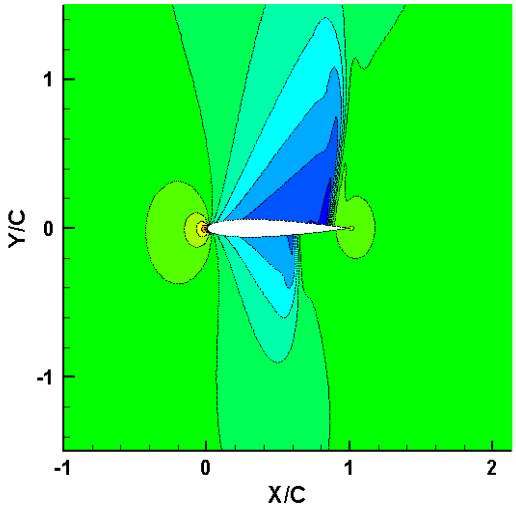

Figure 4.6. Contours of pressure for transonic airfoil at $\alpha = 1^{\circ}$

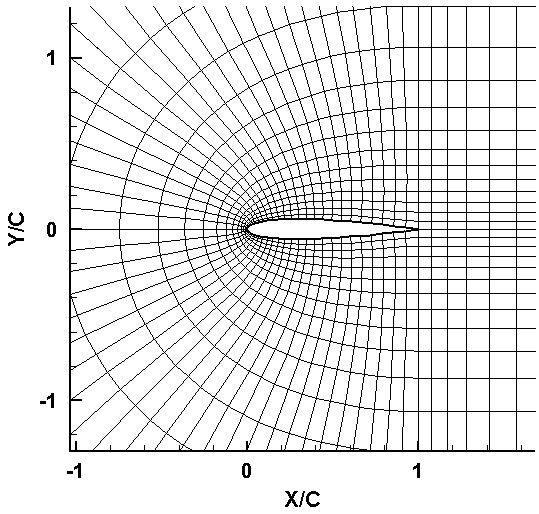

Figure 4.7. Grid 1 for transonic airfoil problem

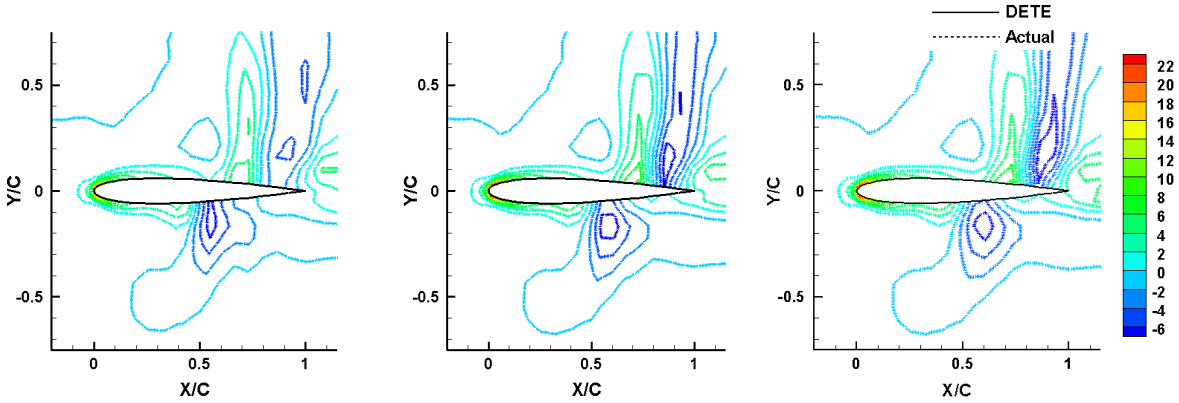

(a) Grid 2 - Grid 1 **(b) Grid 3 - Grid 1** **(c) Grid 4 - Grid 1**

Figure 4.8. Comparison of DETE solutions and actual error of x-momentum (kg/m-s) for transonic airfoil problem

Unsteady Flow

Solving the DETE for unsteady flow requires that the residual be not only spatially accurate, but temporally accurate as well. In order to validate the DETE for this type of problem, the coarse grid and fine grid solutions are generated simultaneously using the smallest time step calculated on either grid. At each step in the time integration, the value of the residual is calculated to update the DETE solution on the coarse grid.

Isentropic Vortex

This problem is a slightly modified version of the passive convection of an isentropic vortex which was presented in Chapter 2 to verify the order of accuracy of the numerical scheme. In this case, the domain is rectangular with dimensions [0,40] by [0,20]. The boundary conditions are far field on all sides. The three grids used for this problem contain 3,200, 12,800, and 51,200 equally spaced, square cells. The same vortex strength is used, initially centered at (10,10), but the mean flow is now defined as $(u,v) = (1,0)$ and $p = \rho = T = 1$ so that the vortex propagation is aligned with the grid. The DETE and flow solutions were integrated up to $t = 20$; the DETE solutions are compared with the actual error in x-momentum at $t = 5.2$, 10, 15.2, and 20 in Figure 4.9. As before, the contours of the DETE solution overlap the actual error. Using the exact residual, the DETE is able to simulate the production and transport of error as the coarse grid flow solution is slowly degraded by numerical diffusion.

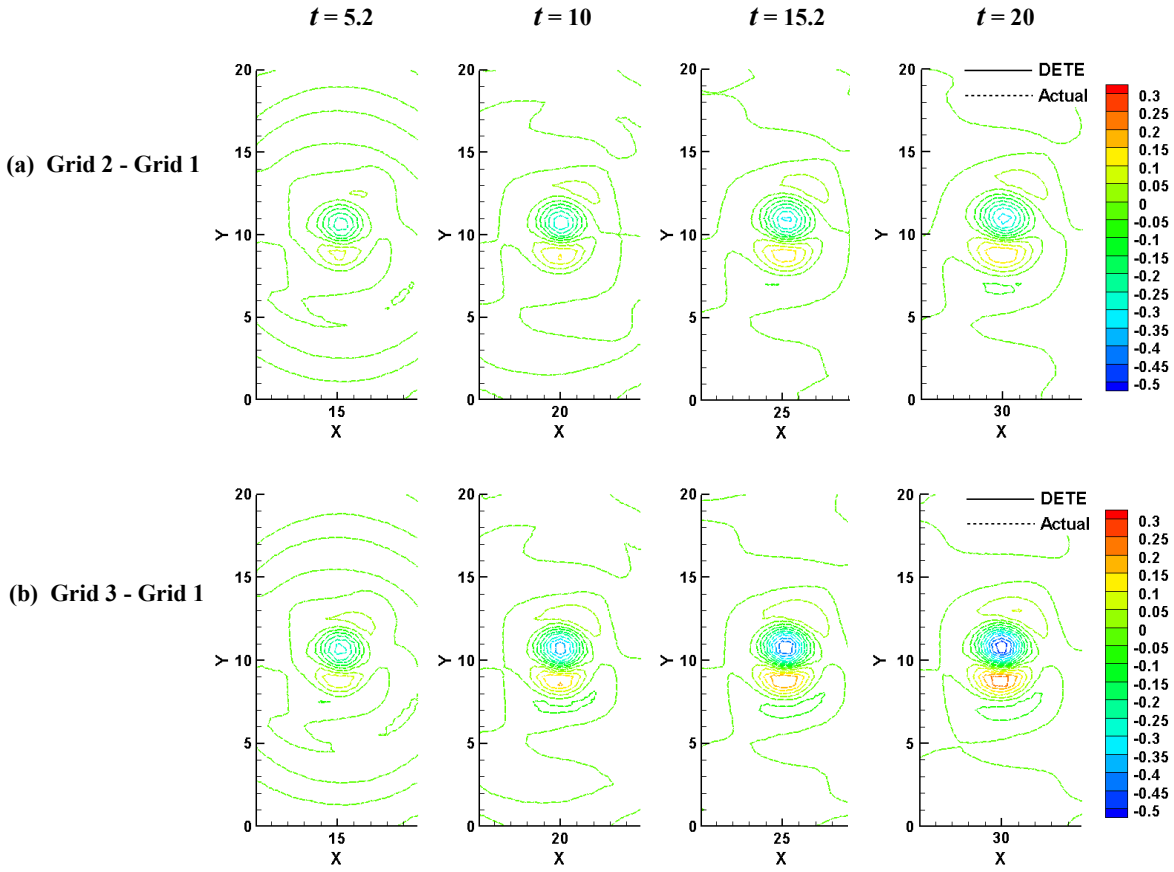

Figure 4.9. Comparison of DETE solutions and actual error of x-momentum (kg/m-s) for isentropic vortex problem

Unsteady Circular Cylinder

The final problem simulates $Re_D = 300$ flow past a circular cylinder, which creates periodic vortex shedding (i.e., a Von Karman vortex street), see Figure 4.10. This problem will be denoted as unsteady cylinder. The cylinder is represented by a no-slip, adiabatic wall; the far field is located fifteen diameters from the cylinder surface, and uses characteristic boundary conditions. Three grids are used for this problem which contain a mix of quadrilateral and triangular cells clustered about the cylinder and wake region to capture the vortex shedding, although only Grid 1 and Grid 2 solutions are considered for this demonstration. Grid 1, shown in Figure 4.11, contains 5,466 cells; Grid 2 and 3 are uniformly refined from Grid 1, and contain 21,864 and 87,456 cells respectively. The mean flow velocity is in the x-direction, but an initial perturbation of 5% of the mean flow velocity is imposed in the y-direction in order to instigate the unsteady, periodic shedding. The flow solutions and DETE solutions were run from $t = 0$ to $t = 2$.

The DETE solutions at $t = 0.5$, 1, 1.5, and 2 are shown in Figure 4.12 and compared with the actual error of x-momentum. Again, the contours of the DETE solutions overlap the actual error showing the high level of accuracy of the DETE. It is also instructive in this case to examine the time history of the lift coefficient for the cylinder. DETE solutions are added to the coarse grid flow solution in order to create a "corrected" solution, which, if accurate, should match the fine grid solution. The flow solutions on the coarse and fine grids, Grid 1 and Grid 2 respectively, are compared with the Grid 1 solution plus the DETE solution on Grid 1 in Figure 4.13. In addition to the magnitude of the lift coefficient, there is a noticeable difference in the frequency of the shedding between flow solutions on Grid 1 and Grid 2. The Grid 1 plus DETE solution matches the Grid 2 solution very well, which indicates that the exact residual accounts for this change in the time-dependent nature of the problem.

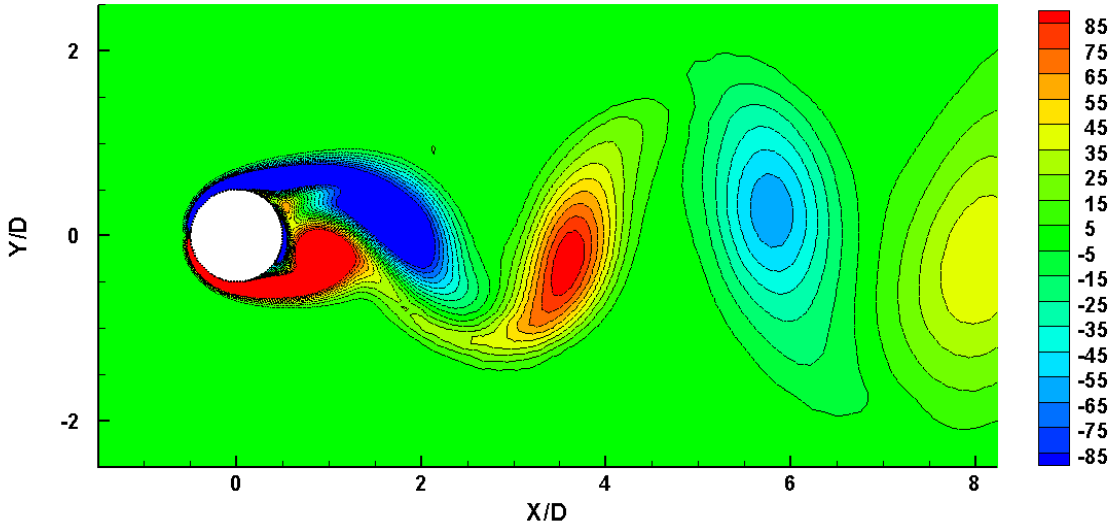

Figure 4.10. Contours of vorticity for Re_D = 300 flow past a circular cylinder

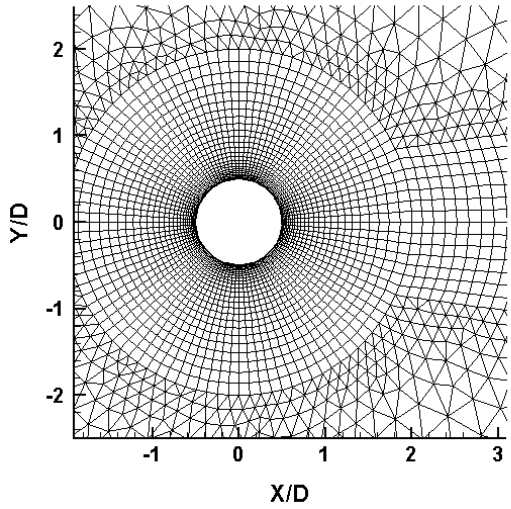

Figure 4.11. Grid 1 for unsteady cylinder problem

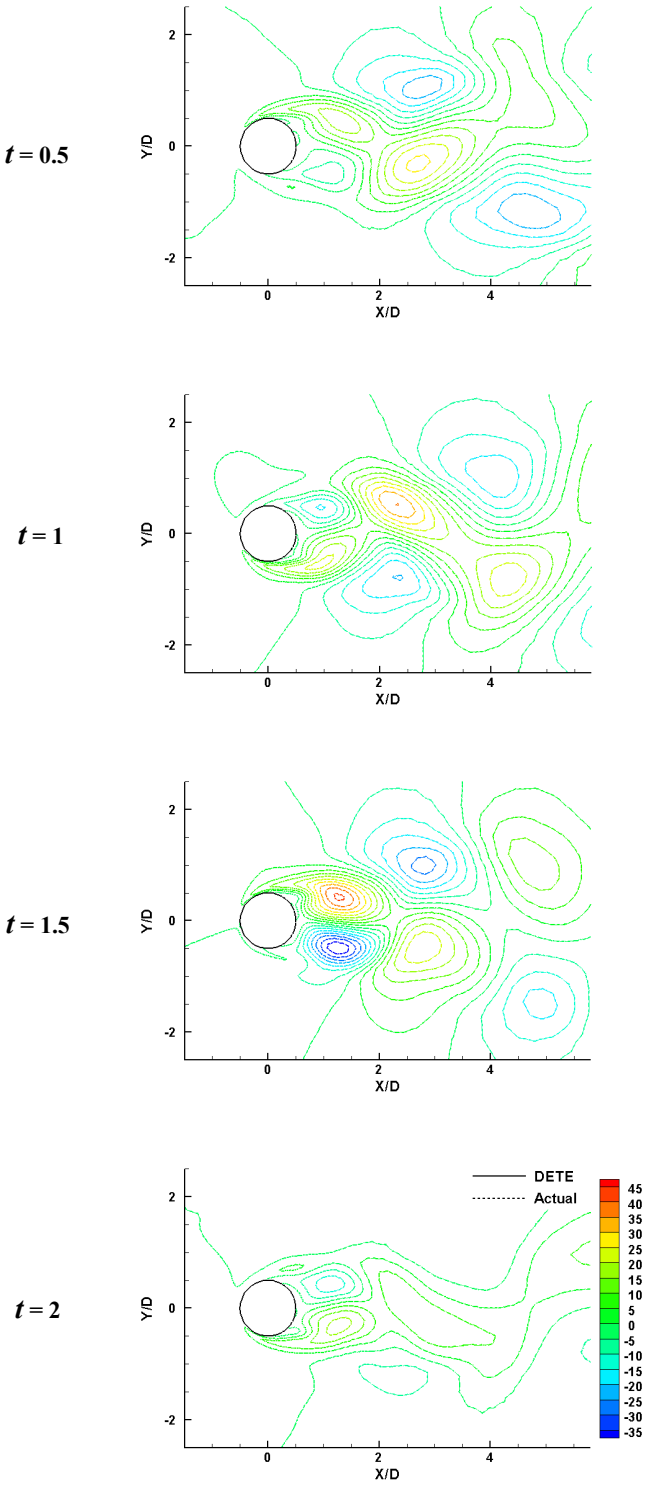

Figure 4.12. Comparison of DETE solution on Grid 1 and actual error of x-momentum (kg/m-s) relative to Grid 2 flow solution for unsteady cylinder problem

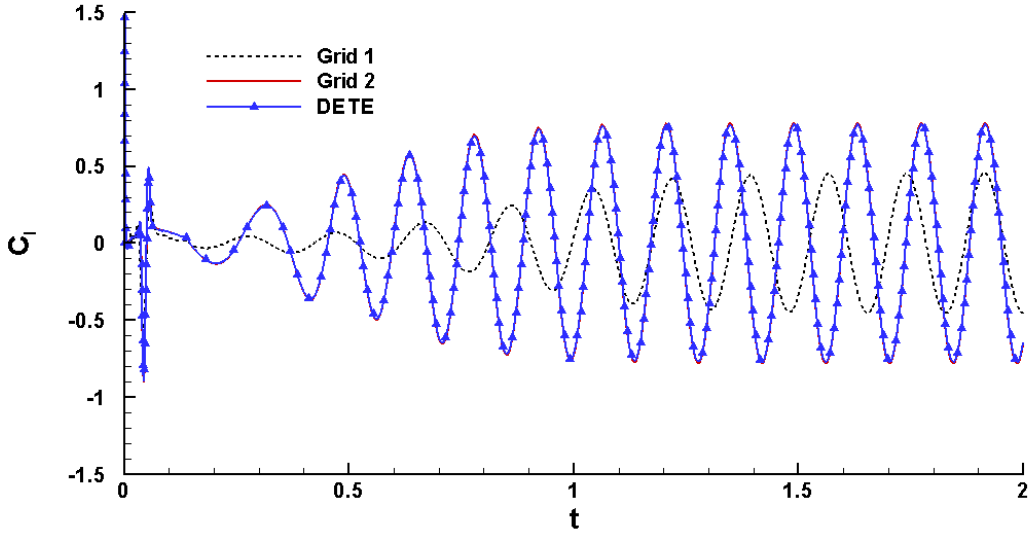

Figure 4.13. Comparison of time history of lift coefficient for unsteady cylinder problem

Chapter 5. Residual Modeling

As noted before, the residual calculated by using a fine grid solution interpolated to the coarse grid is not terribly useful since the error could be obtained by simply differencing the two solutions. Therefore, it is necessary to have a residual model to predict the value of the residual on the finest grid to be used for analysis. Three different residual models will be presented in this chapter; two based on a single grid and solution, one based on multiple grids and solutions.

First, it may useful to explore the characteristics of residual and how it corresponds to the error. To do so, we will make use of the steady cylinder problem presented in the previous chapter. Consider how the location of the error correlates to the location of the residual. Conceptually, the DETE describes how error is generated through the residual. If the residual is zero everywhere in the domain, the error must also be zero. Therefore, the location of non-zero values of the residual should correspond to sources of error.

The steady cylinder case with the intentional grid defect illustrates this concept quite well. If the uniform grid solution is considered a grid independent solution, then the error on the grid with the defect should originate in the area of the defect itself. The grid-induced residual of the x-momentum conserved variable is shown in Figure 5.1, overlaid by the grid defect cells for reference. The contour level range of this plot has been restricted to 10% of the minimum and maximum values to highlight the areas of the greatest residual. Note that the residual is almost entirely contained within the defect cells and their immediate neighbors. Examining the error in x-momentum overlaid

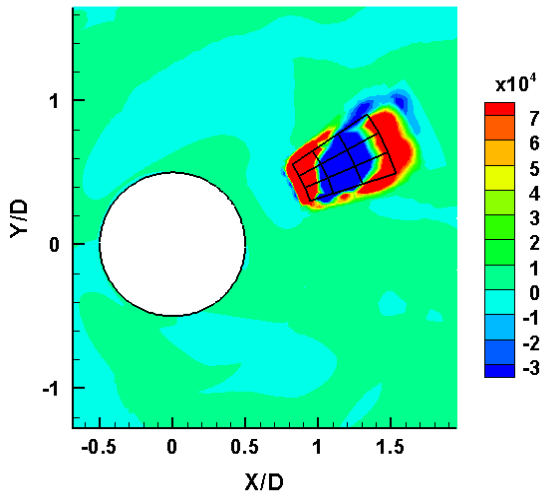

Figure 5.1. Residual of x-momentum for grid with localized defect

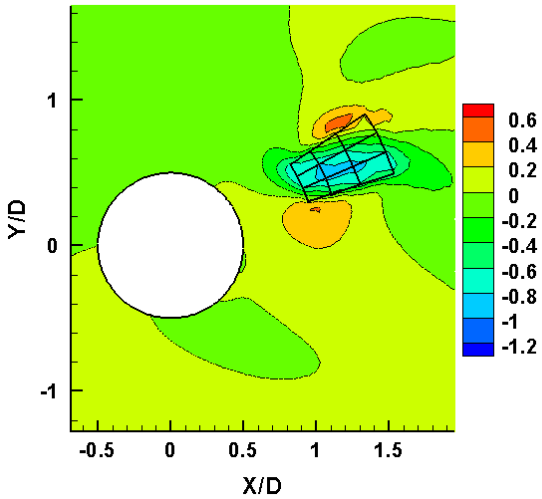

Figure 5.2. Error of x-momentum for grid with localized defect

with the defect cells in Figure 5.2, it is clear that the error is produced at the defect (the area with the largest residual values), and is then transported by the flow. There are areas downstream of the defect, and within the recirculation zone, where error exists, but the values of the residual are quite small. This clearly shows that the location of error does not necessarily correspond to where it is generated.

Identifying the source of error is also a useful idea for adaptive grid refinement. By adapting to the location of error, the grid may be refined unnecessarily in areas that do not produce error. Adapting to areas of large values of the residual, on the other hand, could be used to refine the grid more precisely, using fewer cells than traditional gradient-based adaption schemes.

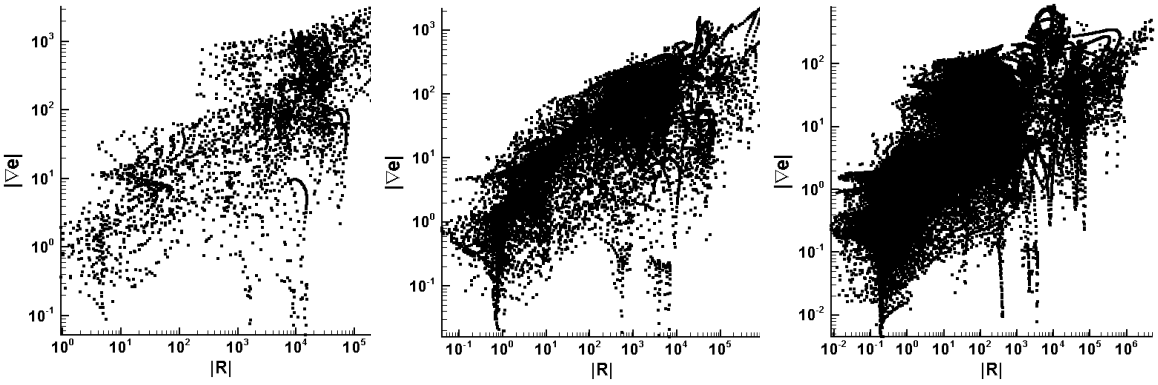

(a) Grid 2 - Grid 1 **(b) Grid 3 - Grid 2** **(c) Grid 4 - Grid 3**

Figure 5.3. Trends of residual magnitude vs. absolute value of error gradient for steady cylinder problem with uniformly refined grids

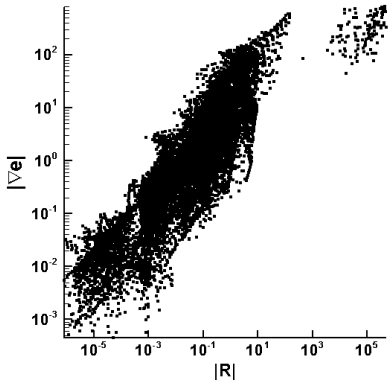

Figure 5.4. Trend of residual magnitude vs. absolute value of error gradient for steady cylinder problem with localized grid defect

Another way to examine the idea of error generation is to compare the magnitude of the gradient of the error with the magnitude of the residual. Figure 5.3 plots the absolute values of the residual and error gradients of x-momentum for the uniformly refined steady cylinder case; the residuals for Grids 1 through 3 were obtained using the solution on the next most refined grid. Figure 5.4 presents the same information for the steady cylinder case with the localized grid defect. There is generally a linear relationship between the magnitudes of the error gradient and the residual. This behavior suggests the residual acts as a point source/sink for the error, injecting error into the solution and allowing it to be convected and diffused away.

As the grid is continually refined and the solution approaches grid independence, the difference between solutions becomes increasingly small. Therefore, the residual from each successively refined solution should also become small, at least in the global sense. Returning to the method of Richardson extrapolation, if a solution is convergent, then estimates of the grid independent solution (*GI*) using solutions on grids with spacing h, $2h$, and $4h$ can be written as:

$$Q_{GI} \simeq Q_{2h} + \frac{1}{\left(4h/2h\right)^{P} - 1}\left(Q_{2h} - Q_{4h}\right) \tag{5.1}$$

$$Q_{GI} \simeq Q_{h} + \frac{1}{\left(2h/h\right)^{P} - 1}\left(Q_{h} - Q_{2h}\right) \tag{5.2}$$

Combining Eqs. (5.1) and (5.2) yields an expression for the rate of convergence and the order of the numerical scheme, P,

$$P = \frac{\ln\left[\dfrac{Q_{2h} - Q_{4h}}{Q_{h} - Q_{2h}}\right]}{\ln\left(2\right)} \tag{5.3}$$

Equation (5.3) is normally used to verify the order of a numerical scheme, but if it is rewritten in terms of the error estimate from Eq. (1.23) and grid spacing,

$$P = \frac{\ln\left(e_{2h}/e_{h}\right)}{\ln\left(2h/h\right)} \tag{5.4}$$

then rearranged,

$$e_{h} = e_{2h}\left(h/2h\right)^{P} \tag{5.5}$$

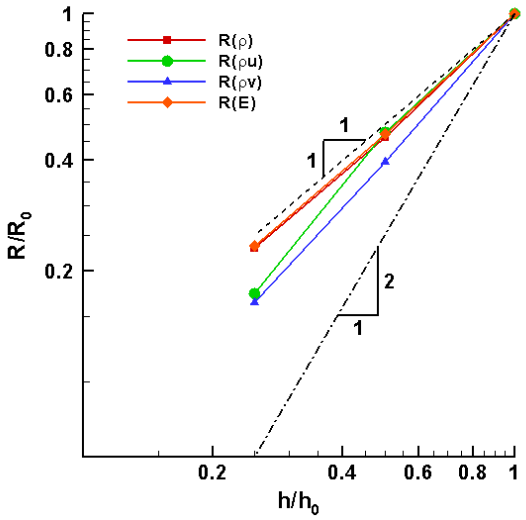

Figure 5.5. Residual relative to a single level of refinement vs. grid spacing

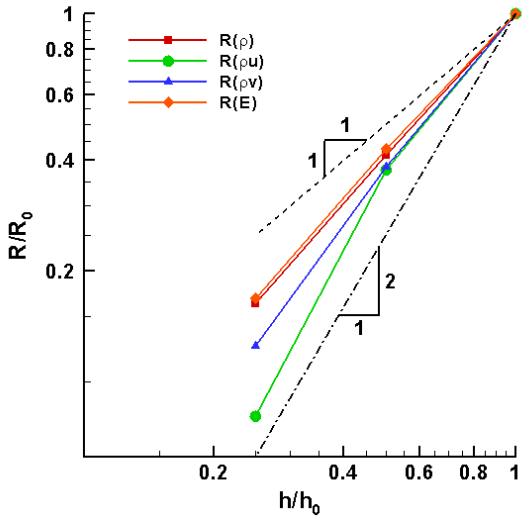

Figure 5.6. Residual relative to finest grid vs. grid spacing

an expression for the behavior of the error as a function of grid spacing is obtained. If these are global measures of error, and the numerical scheme is globally second order accurate, then the error should be a nearly parabolic function of the grid spacing (i.e., $P = 2$). Since the error is a direct function of the residual, it follows that the residual should behave in the same way.

The L1 norms of the residuals (resulting from a solution on the next finest grid) of each conserved variable, normalized by the coarsest grid values, are plotted on a log-log scale as a function of normalized grid spacing for the uniformly refined steady cylinder problem in Figure 5.5. The residuals show a trend approaching zero, but the slopes of the residuals are somewhere between one and two, which implies that the error relative to a single level of refinement is not converging at the expected second-order rate for this numerical scheme.

If the finest grid solution is considered to be grid-independent, then the error and the residual on each coarser grid relative to the finest grid solution should approach zero as the grid spacing approaches that of the finest grid. The L1 norms of the residuals relative to the finest grid solution for the uniformly refined steady cylinder problem are shown in Figure 5.6. As before, the residuals in this case do not quite converge at a second-order rate, but the slopes at $h/h_0 = 0.5$ are much closer to two.

The fact that the L1 norms of the residuals in Figure 5.5 and Figure 5.6 do not converge at the expected second-order rate is not entirely unexpected. It was shown during the validation of the finite

volume scheme that the rate of convergence could be problem dependent, and was not even constant on every grid used in each test problem. However, the residuals for the steady cylinder problem exhibit rates of convergence somewhere between first-order and second-order, which generally agrees with the rate of convergence observed for the laminar Poiseuille flow problem.

Approximate Modified Equation (AME) Model

A natural analogue for the residual may be an expression to calculate the truncation error (TE) – the difference between the original PDE and the discretized version. By expanding the discretized PDE in terms of Taylor series, one can recover the differential form of the original PDE plus some extra terms which are collected and called the truncation error. In simplistic notation, the PDE can be written as the finite volume equation (FVE) plus the truncation error,

$$PDE = FVE + TE \tag{5.6}$$

A solution of the finite volume equation which approximates the PDE is then

$$FVE = -TE \tag{5.7}$$

If Eq.(5.7) is compared with the linear operator on a coarse grid with a fine grid solution (i.e., an approximation of the linear operator on the fine grid with the fine grid solution),

$$L_D\left(Q_h, H, \Delta t_H\right) = R_H^h \tag{5.8}$$

there is an obvious relationship between the terms of the truncation error and the value of the residual.

The classic approach for determining the truncation error for a given numerical scheme is the modified equation. While the modified equation can readily be derived for simple model equations and difference schemes, the process can be quite complicated and tedious for most PDEs and numerical schemes of interest. Therefore, the AME model presented here uses an approximate form of the modified equation, similar to the approach used by Zhang, et al. [23]. It should be noted that this analysis assumes equal grid spacing and regular quadrilateral or equilateral triangular cells. The following derivation will not hold for a completely general unstructured grid. Starting with Eq. (2.10) , and writing the time derivative as a forward Euler difference for simplicity,

$$\frac{Q_i^{n+1} - Q_i^n}{\Delta t_i} + \frac{1}{\forall_i} \sum_{j=1}^{J_i} \left[\overline{\boldsymbol{f}}_{i,j} + \overline{\boldsymbol{g}}_{i,j} \right] S_{i,j} = 0 \tag{5.9}$$

If the n+1 time level solution is written as a Taylor series expanded about the n time level and then substituted, the original differential time derivative is recovered with higher order terms:

$$\frac{\partial Q}{\partial t}+\frac{\Delta t}{2}\frac{\partial^2 Q}{\partial t^2}=-\frac{1}{\forall_i}\sum_{j=1}^{J_i}\left[\bar{\boldsymbol{f}}_{i,j}+\bar{\boldsymbol{g}}_{i,j}\right]S_{i,j}+O\left(\Delta t^2\right) \tag{5.10}$$

The left and right state fluxes in the Rusanov flux formulation are expanded in terms of cell average values,

$$\boldsymbol{f}_L=\boldsymbol{f}_i+\boldsymbol{\ell}_j\cdot\nabla\boldsymbol{f}_i+O\left(\ell^2\right),\qquad \boldsymbol{f}_R=\boldsymbol{f}_j+\boldsymbol{\ell}'_j\cdot\nabla\boldsymbol{f}_j+O\left(\ell^2\right) \tag{5.11}$$

and, using the assumption of a smooth solution, the face neighbor cell average flux is approximated as:

$$\boldsymbol{f}_j\simeq\boldsymbol{f}_i+\left(\boldsymbol{\ell}_j-\boldsymbol{\ell}'_j\right)\cdot\nabla\boldsymbol{f}_i+O\left(\ell^2\right) \tag{5.12}$$

The terms $\boldsymbol{\ell}$ and $\boldsymbol{\ell}'$ are vectors connecting the cell centers and the face center, as defined in Figure 5.7. The convective flux can now be written as:

$$\bar{\boldsymbol{f}}_{i,j}\simeq\frac{1}{2}\left[\left(2\boldsymbol{f}_i+2\boldsymbol{\ell}_j\cdot\nabla\boldsymbol{f}_i+\boldsymbol{\ell}'_j\cdot\left(\nabla\boldsymbol{f}_j-\nabla\boldsymbol{f}_i\right)+O\left(\ell^2\right)\right)\cdot\hat{\boldsymbol{n}}_j-\varphi_j\right] \tag{5.13}$$

where φ_j is the spectral radius term of the Rusanov flux evaluated at the cell face. A similar process is used to expand the diffusive terms, and after carrying out the summation on the $\boldsymbol{\ell}_j$ terms, the gradients of the fluxes reappear,

$$\begin{aligned}&\frac{\partial Q}{\partial t}+\nabla\bullet\boldsymbol{f}+\nabla\bullet\boldsymbol{g}=\\&\quad-\frac{\Delta t}{2}\frac{\partial^2 Q}{\partial t^2}-\frac{1}{2\forall_i}\sum_{j=1}^{J_i}\left[\left(\boldsymbol{\ell}'_j\cdot\left(\nabla\boldsymbol{f}_j+\nabla\boldsymbol{g}_j\right)-\boldsymbol{\ell}'_j\cdot\left(\nabla\boldsymbol{f}_i+\nabla\boldsymbol{g}_i\right)\right)\cdot\hat{\boldsymbol{n}}_j-\varphi_j\right]S_{i,j}+O\left(\ell^2,\Delta t^2\right)\end{aligned} \tag{5.14}$$

For this explicit time integration scheme, the second order time derivative term will be small compared to the summation on the RHS, so it is neglected. Subtracting Eq. (5.14) from the original PDE yields the approximate modified equation. The residual based on the AME model is then defined as:

$$R^{AME}=\frac{1}{2\forall_i}\sum_{j=1}^{J_i}\left[\left(\boldsymbol{\ell}'_j\cdot\left(\nabla\boldsymbol{f}_j+\nabla\boldsymbol{g}_j\right)-\boldsymbol{\ell}'_j\cdot\left(\nabla\boldsymbol{f}_i+\nabla\boldsymbol{g}_i\right)\right)\cdot\hat{\boldsymbol{n}}_j-\varphi_j\right]S_{i,j} \tag{5.15}$$

It should be noted that this residual model has been derived for this numerical scheme only. Other schemes that may use different forms of the convective flux, for example, will produce a different expression.

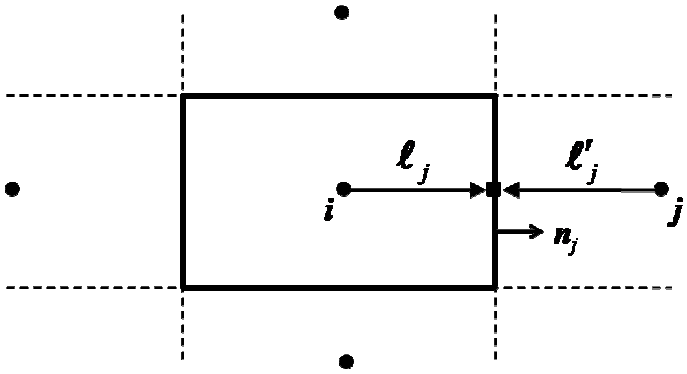

Figure 5.7. Schematic of face neighbor geometry for AME Model; ● – cell centers; ■ – face center

PDE Model

For error estimation using the method of nearby problems (which is functionally similar to the DETE), Roy et al. [33-35] advocate a residual model which evaluates the original governing PDE with a continuous spline fit of the numerical solution. The spline fit requires that the domain be divided into smaller sub-domains in order to properly capture all flow features. Depending on the characteristics of the flow, the number of sub-domains could be quite large, and must be carefully positioned to avoid discontinuities. In this model, we propose using a small, local stencil of face and node neighbor cells to generate a least squares polynomial fit of cell average data for each cell in the domain. The polynomial fits of neighboring cells are not required to be continuous.

In general, any order polynomial may be used, but this investigation is limited to first, second, and third degree polynomials to keep the stencil small (see Figure 5.8). For instance, a first degree polynomial requires at least three cells in the stencil, but a third degree polynomial requires at least ten cells. In order to get a system that is not poorly conditioned, it is better to use more than the minimum number of cells. Thus, the size of the stencil can grow quickly, which is undesirable in areas of large gradients and near discontinuities. Details of the least squares polynomial fit procedure can be found in Appendix B. To find the cell average residual, the governing PDE is integrated over each cell using the polynomial fit of the solution data by way of three point Gauss quadrature; any non-zero integral yields a value for the residual.

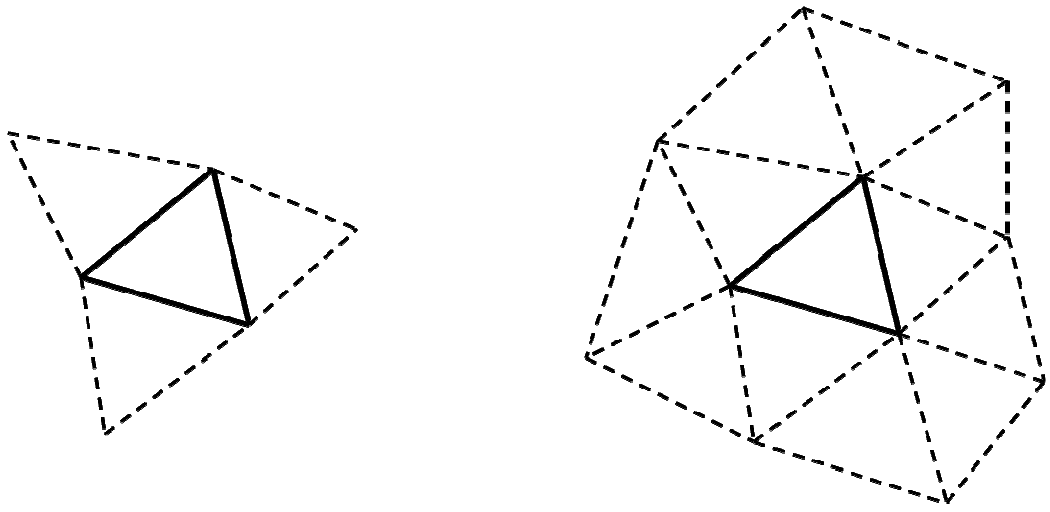

(a) First degree polynomial stencil

(b) Second degree polynomial stencil

Figure 5.8. Computational stencils for least square polynomial fit

While the PDE model uses a potentially expensive least squares fit of the solution data, it does not require any analytical derivations which are dependent on the numerical scheme. Therefore, the PDE model should be much easier to implement than the AME model, especially for numerical schemes which are more complicated than the one used here.

Extrapolation Model

Another possible technique for modeling the residual is to extrapolate the exact residual from the coarse grid to the fine grid. From the analysis of the residual based on Richardson extrapolation presented earlier, the residual can be written as a function of the grid spacing if a problem is convergent. The fine grid residual extrapolated from the coarse grid is written as:

$$R_h^E = R_H^h \left(\frac{h}{H} \right)^P \tag{5.16}$$

Of course, as with Richardson extrapolation, the rate of convergence, P, which should be used with this expression is actually a local value and is problem dependent. However, to calculate P locally would require at least three grids and solutions, and this method would provide no advantage over using Richardson extrapolation. Therefore, two assumptions are made: (1) the solution is globally and locally convergent everywhere; (2) the rate of convergence for any problem is the formal theoretical order of accuracy for the numerical scheme. The first assumption will not hold for every cell in the domain; in areas where the solution is particularly sensitive to grid spacing, the residual

may actually increase as the grid is refined, even when the solution is globally convergent. The second assumption will also not hold for every problem studied. As seen in the verification of the numerical scheme in Chapter 2, and the rate of convergence plots for the residual presented earlier, the actual rate of convergence is quite problem dependent. If the problem does not stray too far from these assumptions though, the added accuracy of using the actual grid-induced residual and solving the DETE on the fine grid may prove useful.

Chapter 6. Evaluation of Residual Models

The accuracy of the residual models will be evaluated for the same set of test problems used to validate the DETE solution accuracy in Chapter 4. Results for this wide array of flow conditions will highlight strengths and weaknesses in each model.

The PDE and extrapolation models have some variability in their implementation. The PDE model may use any degree polynomial in the least squares fit; therefore, first, second, and third degree polynomials will be tested to assess which of those works best. The DETE solutions with each degree polynomial will be denoted as *PDE_1*, *PDE_2*, and *PDE_3* respectively. The extrapolation model relies on the global order of accuracy to scale the residual after it is interpolated from the coarse grid to the fine grid. It has been shown that the current numerical scheme does not exhibit formal second order accuracy for every problem studied, so the extrapolation model will be evaluated using both first-order and second-order convergence rates (i.e., $P = 1$ and $P = 2$). The DETE solutions using the extrapolation model will be denoted as *E_1* and *E_2* for the different convergence rates. Correspondingly, DETE solutions using the AME model will be denoted as *AME*.

Steady Flow

Circular Cylinder

The solutions of the DETE with the AME residual model on Grids 1 through 3 are presented in Figure 6.1(a-c), and are compared with the actual error in x-momentum on each grid relative to a single level of refinement in Figure 6.1(d-f). If the AME model contained all terms of the truncation error, the DETE solutions should compare well with the error relative to the finest grid. However, because of the simplifications made during the derivation of the AME, these results show that the DETE solutions with the AME model generally under-predict the error relative to a single level of refinement. The DETE solutions in Figure 6.1 show better agreement as the grid is refined, but on all grids, the distribution pattern and sign of the error are predicted well.

In order to investigate how well the DETE solution with the AME residual model predicts the error in the boundary layer around the cylinder, it is useful to compare the coarse and fine flow solutions with the coarse grid solution "corrected" by the DETE solution. Profiles of the pressure coefficient on the cylinder surface are presented in Figure 6.2, Figure 6.3, and Figure 6.4. The DETE solutions generally agree well with the fine grid flow solutions, although the DETE solution is not as accurate near the separated flow region found near $0.25 \leq X/D \leq 0.5$. As the grid is refined, the

difference between the flow solutions becomes smaller as expected and the DETE solutions with the AME residual model predict this trend.

The DETE solutions using the PDE residual model with each polynomial fit on Grids 1 through 3 are plotted in Figure 6.5(a-i), and are compared with the actual error in x-momentum in Figure 6.5(j-l). It is immediately apparent that the *PDE_1* results greatly over-estimate the magnitude of the error and do not agree with the actual error. There is less difference between the *PDE_2* and *PDE_3* results, although the *PDE_3* results may be slightly more accurate. As in the *AME* results, the results using the PDE model seem to be more accurate as the grid is refined. Examining the pressure coefficient plots for the PDE models in Figure 6.6, Figure 6.7, and Figure 6.8, the *PDE_1* results are very poor, but the *PDE_2* and *PDE_3* results almost match the fine grid solutions exactly. Even in the separated flow region where the AME model was not as accurate, the higher degree polynomial PDE models exhibit excellent performance.

The DETE solutions using the extrapolation residual model on Grids 2 and 3 are given in Figure 6.9(a-d), and are compared again with the actual error in x-momentum in Figure 6.9(e,f). The *E_1* results appear to over-estimate the magnitude of the error, but the general distribution of error is well represented. This would seem to indicate that the residual is not being scaled correctly for this problem. The *E_2* results on the other hand, agree much better with the actual error. Figure 6.10 and Figure 6.11 show the pressure coefficient plots for the extrapolation models. Both the *E_1* and *E_2* results over-predict the magnitude of the error in the boundary layer region, although the *E_2* results are slightly better.

To directly compare the residual models for this problem, several profiles of the error in x-momentum in the wake region downstream of the cylinder are plotted for the best performers from each model. The *PDE_1* and *E_1* results are omitted since they compared poorly with actual error. Figure 6.12 shows the error along the line Y/D = 0 on Grids 1through 3. On each grid, the single grid AME and PDE residual models agree with the actual error best in the region up to X/D = 5, but the extrapolation model is more accurate further downstream. Figure 6.13 presents the error along several transverse cuts through the wake region for Grids 1 through 3. These plots show the same general behavior; the extrapolation model tends to be more accurate further downstream, and the AME and PDE models perform better in the region closer to the cylinder. This indicates that the AME and PDE residual models are sensitive to grid spacing, much like the actual flow solution, since the grid used in this problem becomes coarser further downstream. The grid spacing is built into both of these models: the AME model uses the distance from the cell center to the face center in the Taylor

series expansion of the fluxes; the PDE model uses a least squares polynomial fit where the data is weighted by the grid spacing. In general, the AME and PDE models become more accurate further downstream as the grid is refined.

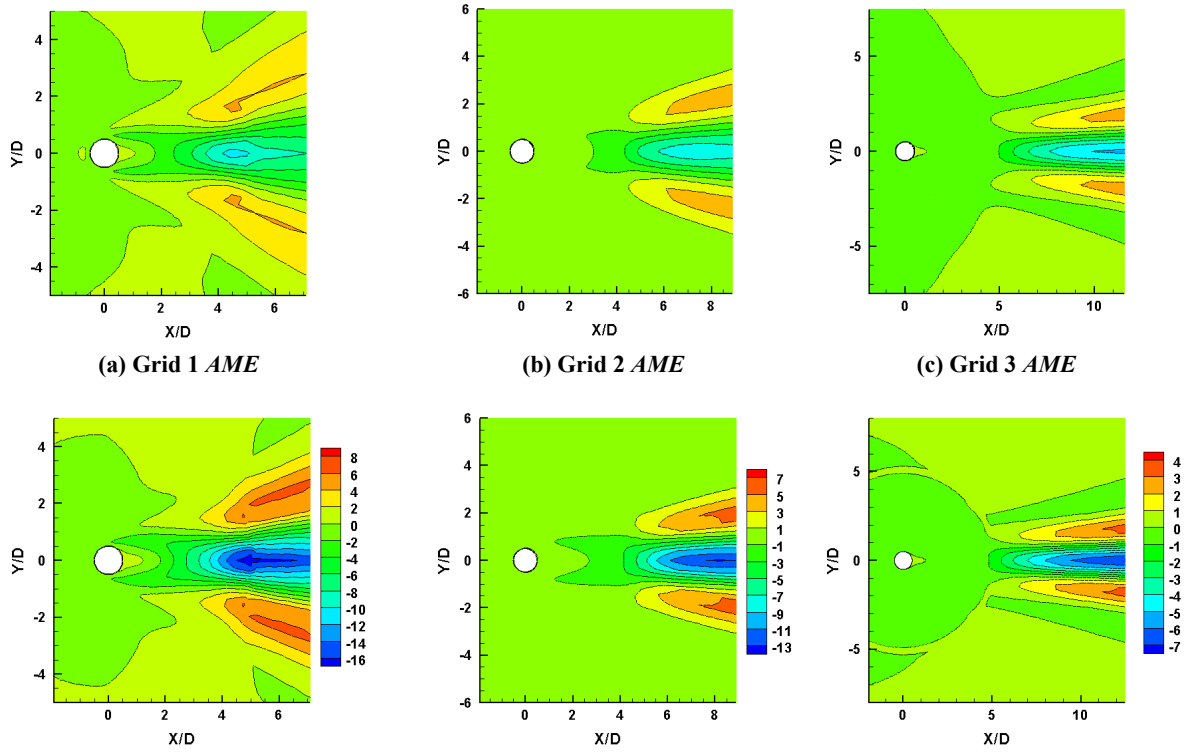

(a) Grid 1 *AME* **(b) Grid 2 *AME*** **(c) Grid 3 *AME***

(d) Grid 2 – Grid 1 **(e) Grid 3 – Grid 2** **(f) Grid 4 – Grid 3**

Figure 6.1. DETE solutions using AME residual model and actual error in x-momentum (kg/m-s) for steady cylinder problem

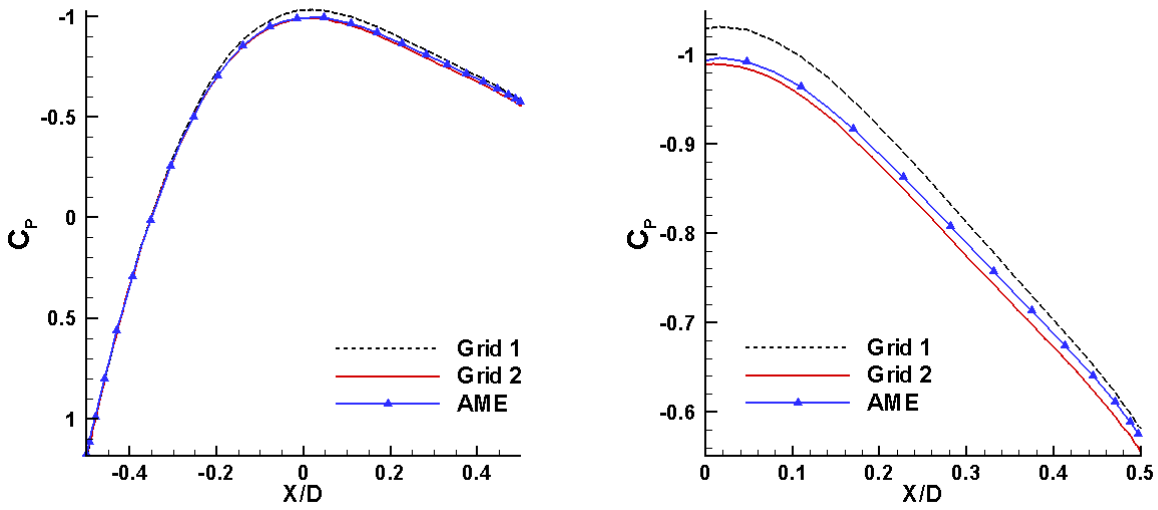

(a) Entire surface **(b) Enlargement of $0 \leq X/D \leq 0.5$**

Figure 6.2. Pressure coefficient on surface of cylinder, DETE results on Grid 1 using AME residual model

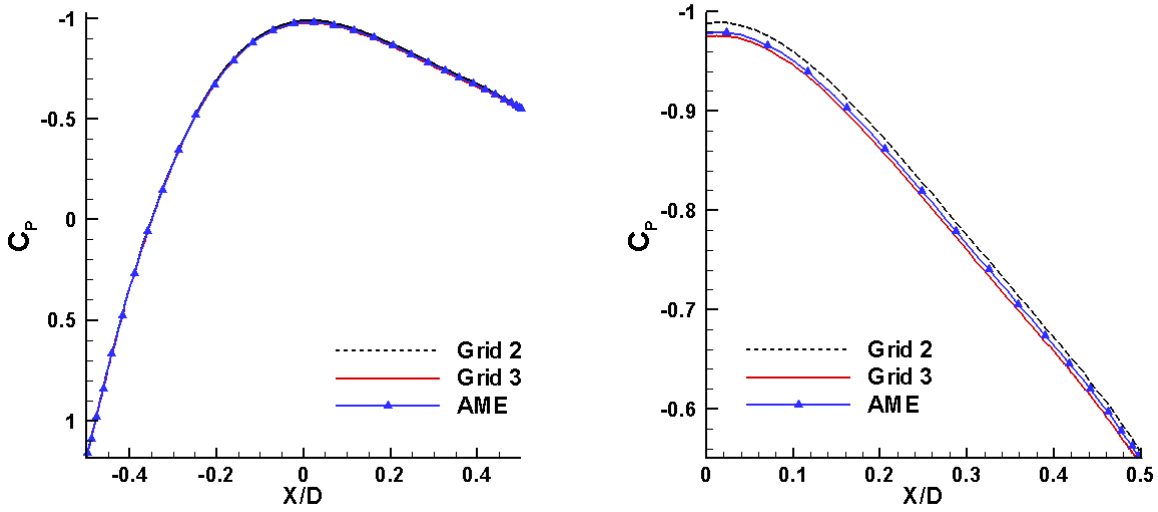

(a) Entire surface **(b) Enlargement of $0 \leq X/D \leq 0.5$**

Figure 6.3. Pressure coefficient on surface of cylinder, DETE results on Grid 2 using AME residual model

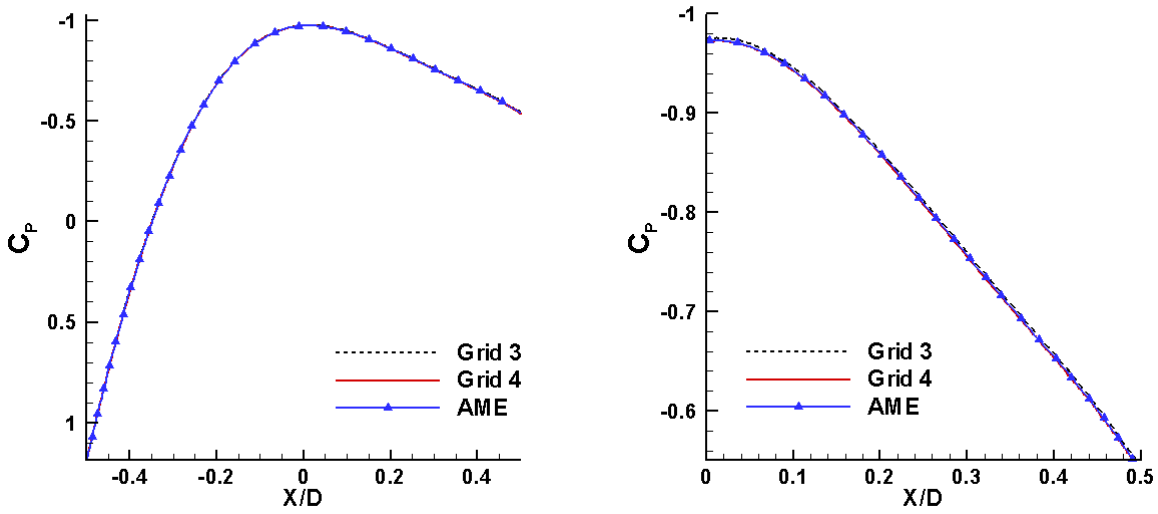

(a) Entire surface **(b) Enlargement of $0 \leq X/D \leq 0.5$**

Figure 6.4. Pressure coefficient on surface of cylinder, DETE results on Grid 3 using AME residual model

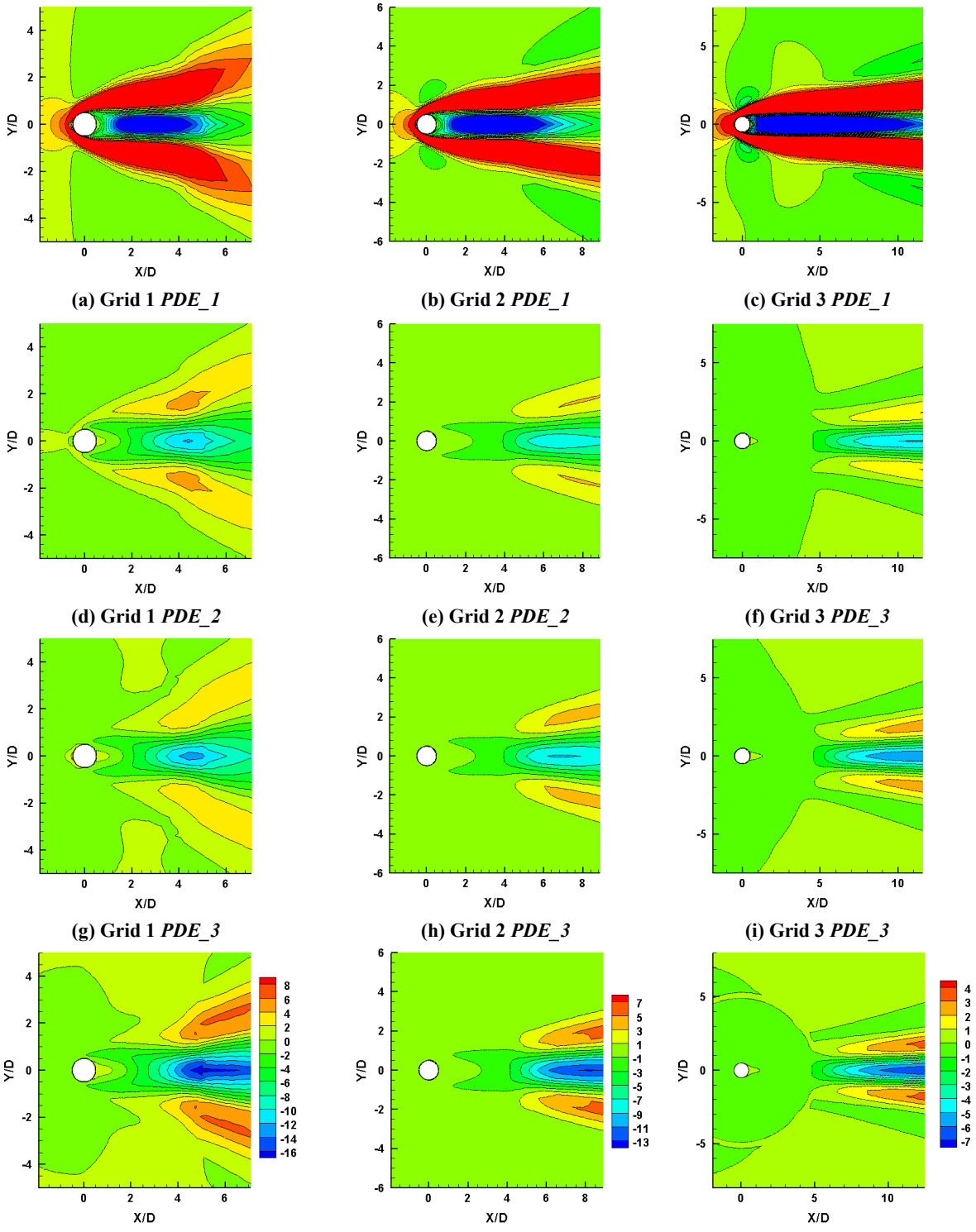

(a) Grid 1 *PDE_1* (b) Grid 2 *PDE_1* (c) Grid 3 *PDE_1*

(d) Grid 1 *PDE_2* (e) Grid 2 *PDE_2* (f) Grid 3 *PDE_3*

(g) Grid 1 *PDE_3* (h) Grid 2 *PDE_3* (i) Grid 3 *PDE_3*

(j) Grid 2 - Grid 1 (k) Grid 3 - Grid 2 (l) Grid 4 - Grid 3

Figure 6.5. DETE solutions using PDE residual model and actual error in x-momentum (kg/m-s) for steady cylinder problem

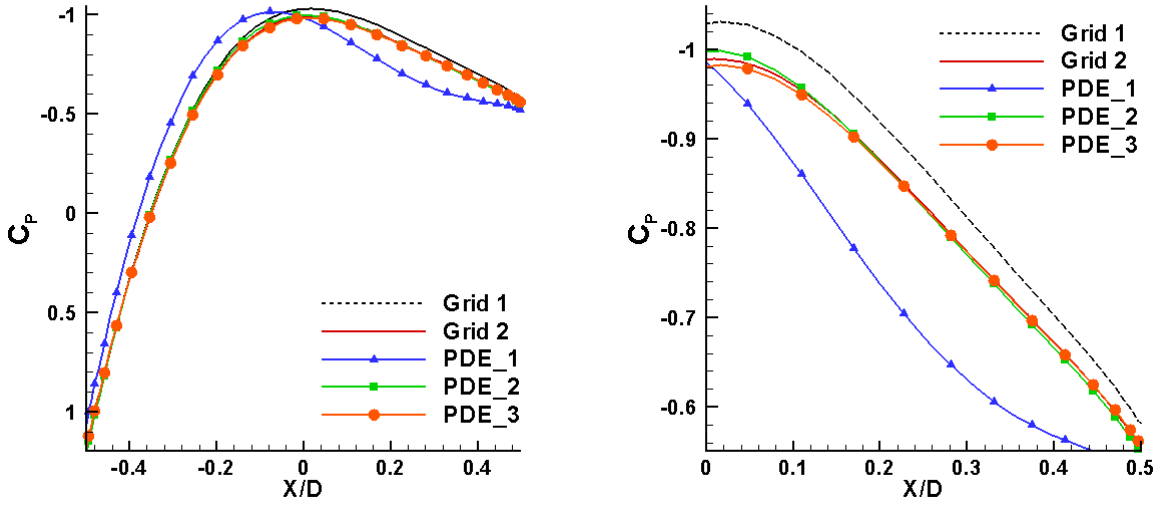

(a) Entire surface (b) Enlargement of $0 \leq X/D \leq 0.5$

Figure 6.6. Pressure coefficient on surface of cylinder, DETE results on Grid 1 using PDE residual model

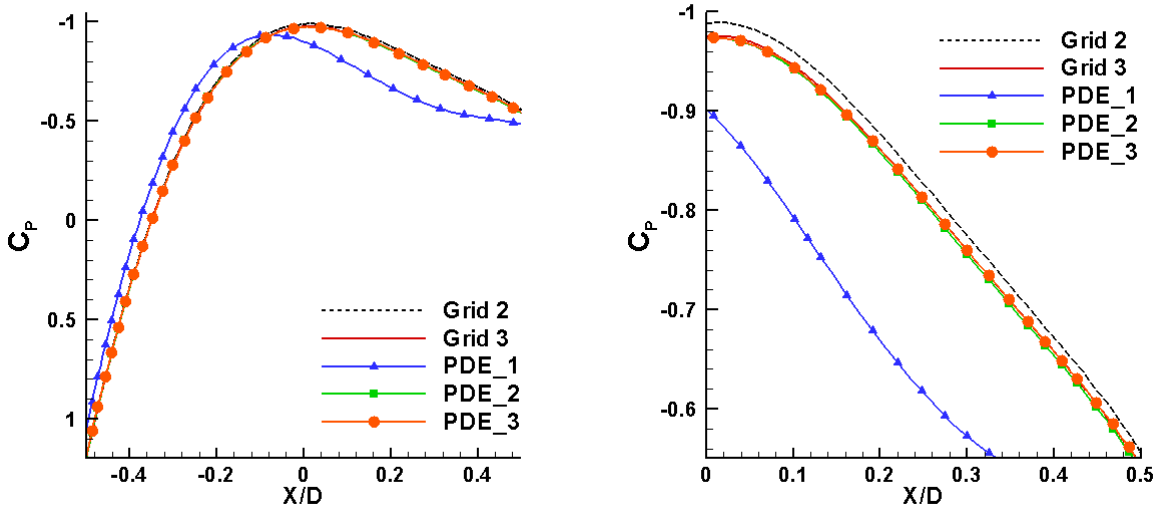

(a) Entire surface (b) Enlargement of $0 \leq X/D \leq 0.5$

Figure 6.7. Pressure coefficient on surface of cylinder, DETE results on Grid 2 using PDE residual model

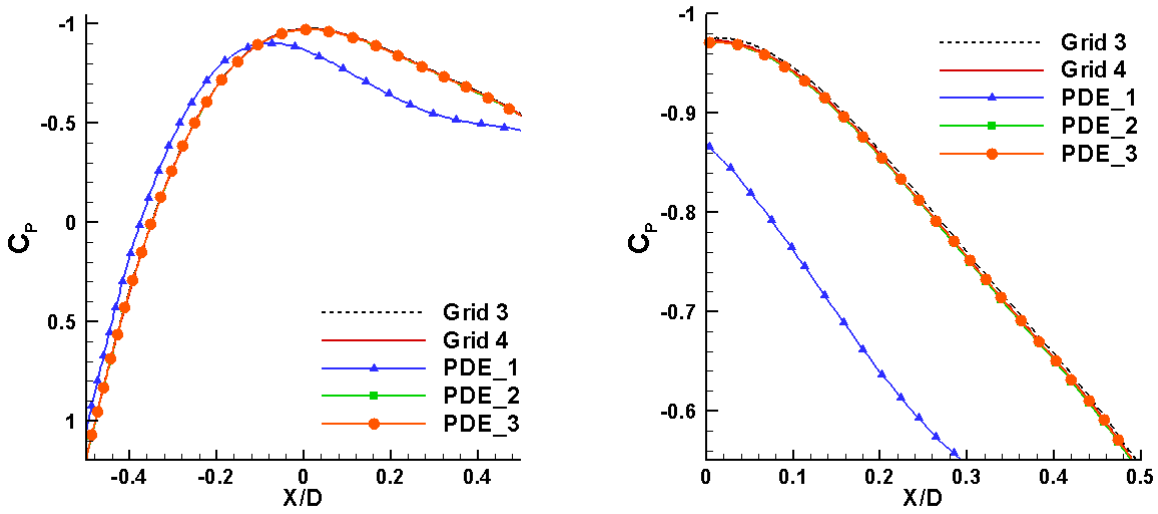

(a) Entire surface **(b) Enlargement of $0 \leq X/D \leq 0.5$**

Figure 6.8. Pressure coefficient on surface of cylinder, DETE results on Grid 3 using PDE residual model

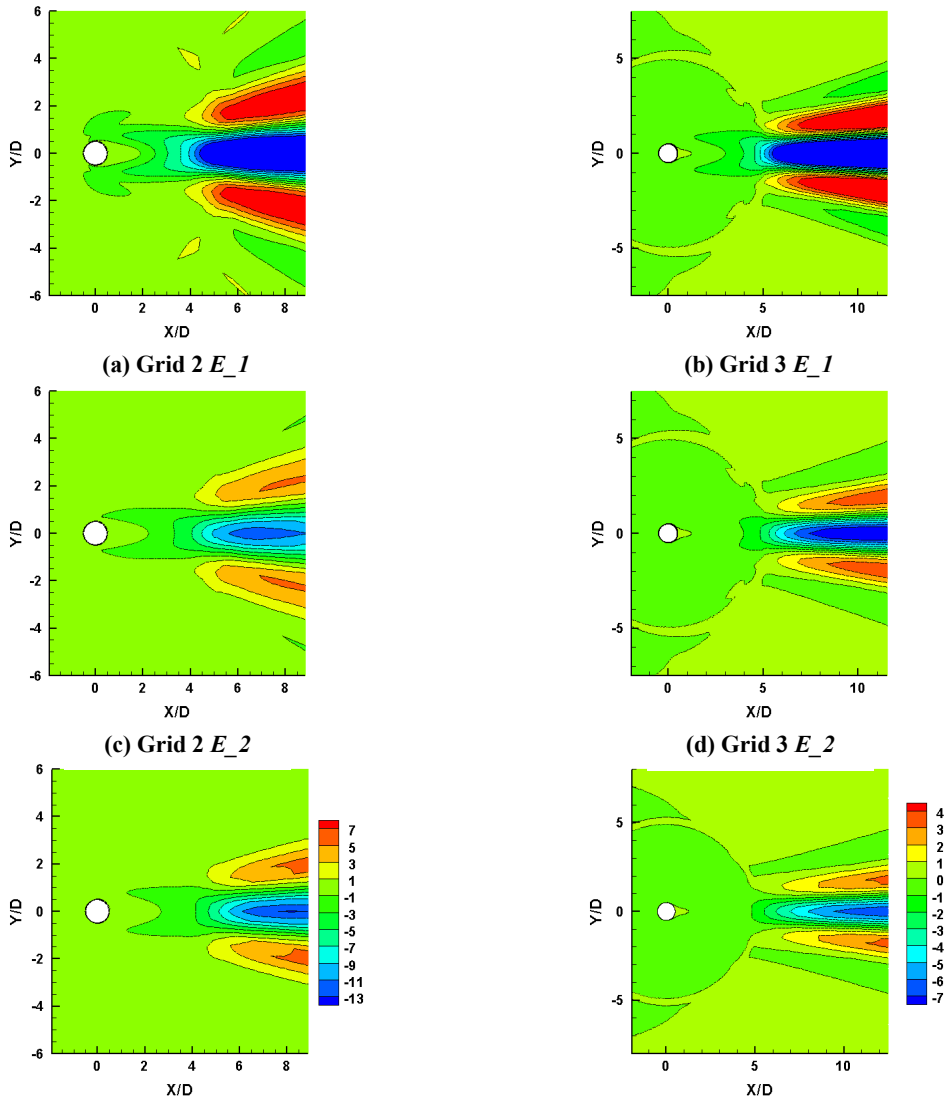

(a) Grid 2 *E_1*

(b) Grid 3 *E_1*

(c) Grid 2 *E_2*

(d) Grid 3 *E_2*

(e) Grid 3 - Grid 2

(f) Grid 4 - Grid 3

Figure 6.9. DETE solutions using extrapolation residual model and actual error in x-momentum (kg/m-s) for steady cylinder problem

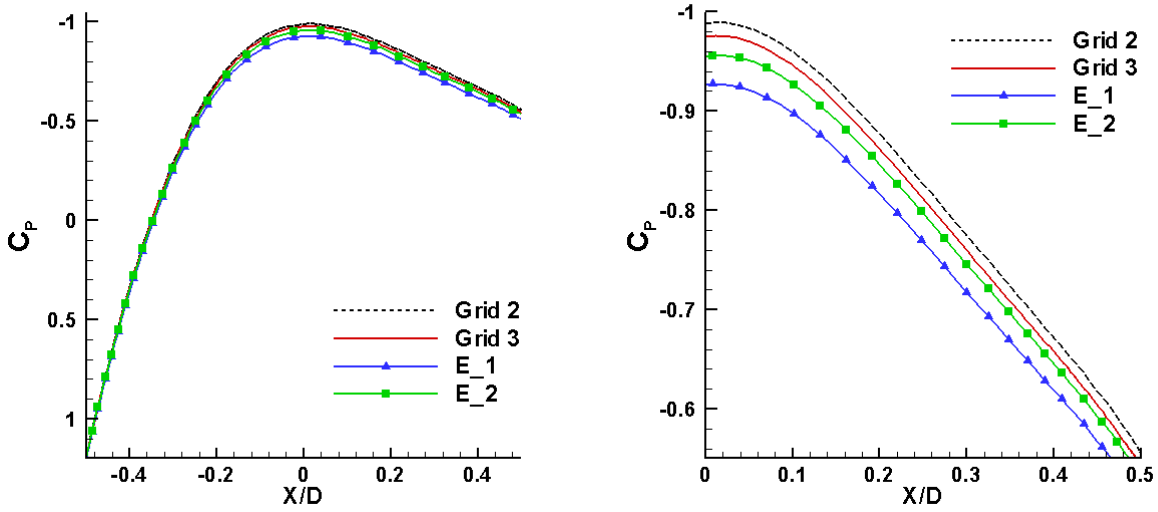

(a) Entire surface **(b) Enlargement of $0 \le X/D \le 0.5$**

Figure 6.10. Pressure coefficient on surface of cylinder, DETE results on Grid 2 using extrapolation residual model

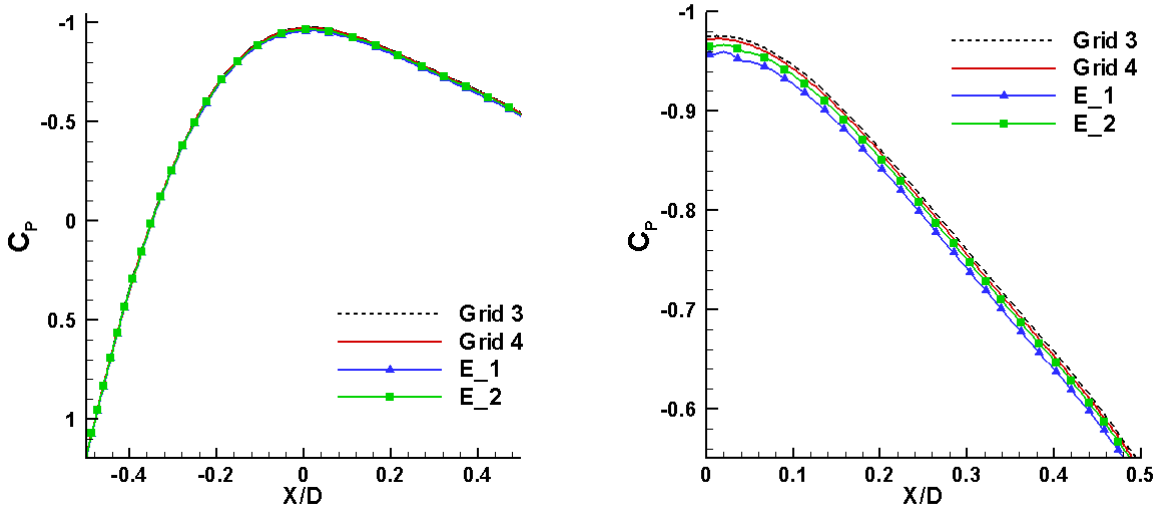

(a) Entire surface **(b) Enlargement of $0 \le X/D \le 0.5$**

Figure 6.11. Pressure coefficient on surface of cylinder, DETE results on Grid 3 using extrapolation residual model

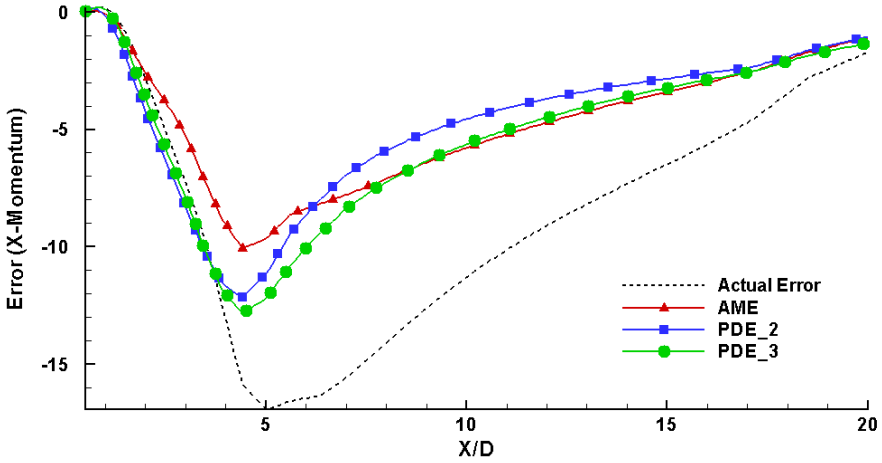

(a) Grid 1

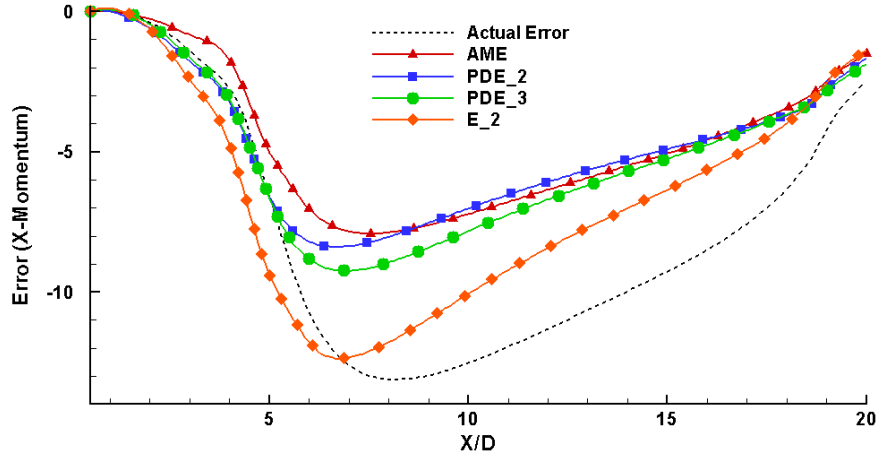

(b) Grid 2

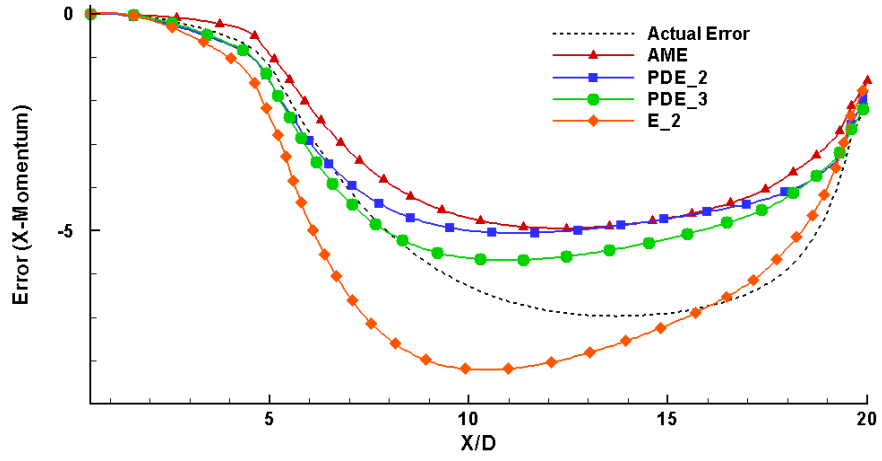

(c) Grid 3

Figure 6.12. Comparison of DETE solutions and actual error in x-momentum (kg/m-s) with various residual models along Y/D = 0

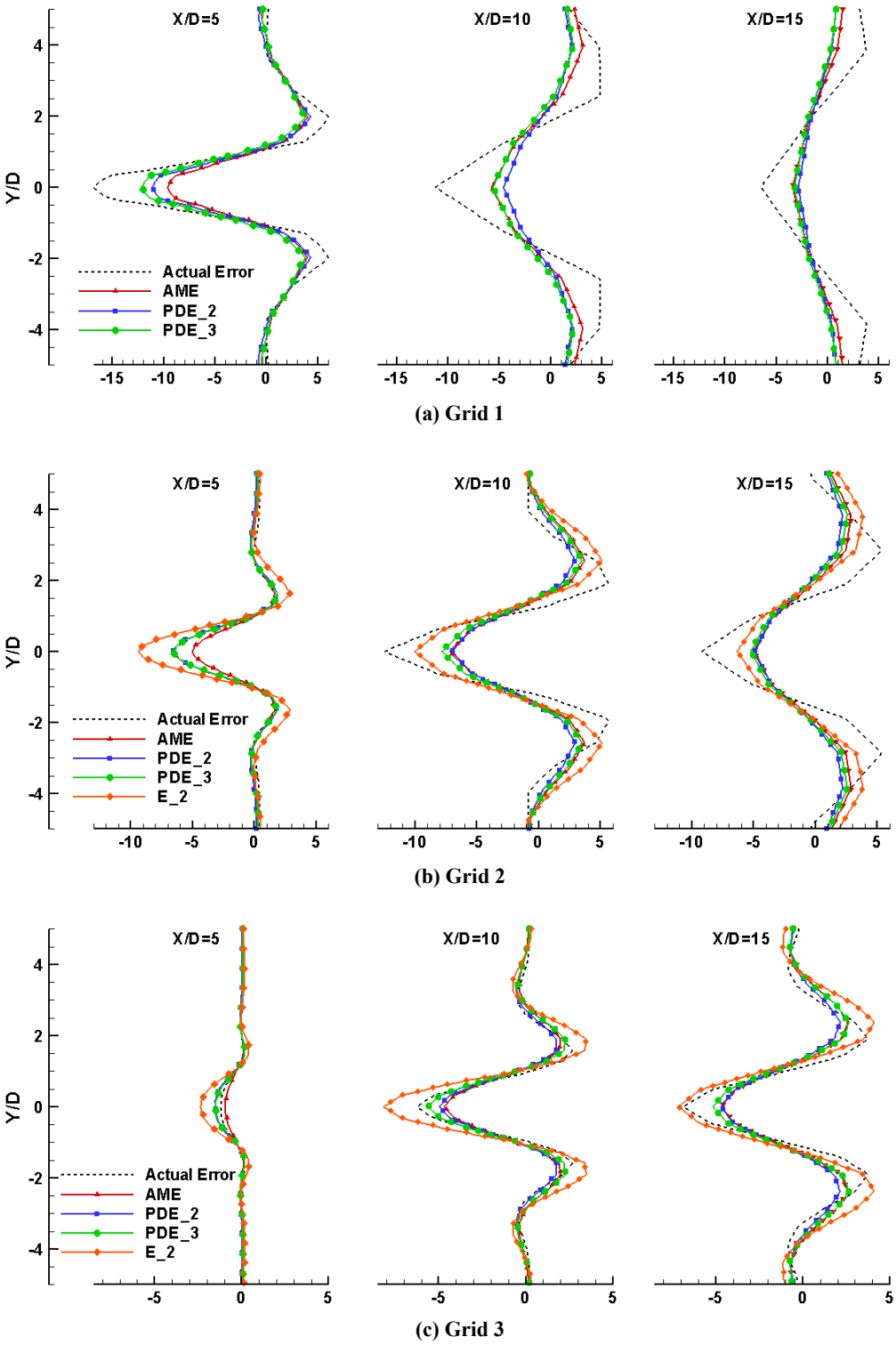

Figure 6.13. Comparison of DETE solutions and actual error in x-momentum (kg/m-s) with various residual models along transverse cuts through wake region

Transonic Airfoil

The solutions of the DETE using the AME model on Grids 1 through 3 are presented in Figure 6.14(a-c), and compared with the actual error in x-momentum for the transonic airfoil problem in Figure 6.14(d-f). As in the steady cylinder problem, the plotted contours of the DETE solution tend to underestimate the magnitude of the error. However, the location and general distribution of error agree with the actual error results. Plots of the pressure coefficient for the DETE solution are compared with the coarse and fine grid solutions in Figure 6.17, Figure 6.16, and Figure 6.15. On each grid, the largest error is found near the shocks on the top and bottom of the airfoil, as would be expected, and the locations of the shocks in the DETE solutions agree well with the fine grid solutions. The DETE solutions on each grid also have a greater slope than the coarse grid flow solutions at the shocks, which is indicative of reducing the numerical dissipation of the shock due to grid spacing.

DETE solutions using the PDE residual model with each polynomial fit on Grids 1 through 3 are given in Figure 6.18(a-i) and are compared with the actual error in x-momentum in Figure 6.18(j-l). At first glance, the DETE solutions from all three PDE residual models appear to over-predict the error near the shocks and/or the leading edge of the airfoil, especially on Grids 2 and 3. Comparing the pressure coefficient profiles on Grids 1 through 3 in Figure 6.19, Figure 6.20, and Figure 6.21, this observation is reinforced. The results on Grid 1 are comparable with the DETE solutions using the AME model, but the Grid 2 and Grid 3 DETE solutions exhibit large oscillations on both sides of the shocks, and the location of the shocks themselves is incorrect. As noted in the discussion of the PDE residual model, using a stencil which includes cells near a discontinuity for the least square polynomial fit can produce poor results. This is the most likely culprit for the inaccuracy of the PDE model results in this case.

The DETE solutions using the extrapolation model on Grids 2 and 3 are shown in Figure 6.22(a-d), and are compared with the actual error in x-momentum in Figure 6.22(e,f). The *E_1* results look similar to the PDE model results for both grids, but the *E_2* results appear to have reasonable agreement with the actual error on Grid 3. Examining the pressure coefficient profiles in Figure 6.23 and Figure 6.24, neither extrapolation model compares well with the flow solutions on Grid 2. On Grid 3 however, both extrapolation models predict the location of the shock well.

The DETE solutions using all residual models appear to have larger oscillations before and after the shock than the flow solutions. The oscillations in the flow solutions are known to be a numerical artifact and are usually eliminated by using a limiting procedure during the reconstruction of the cell

average data; no limiter is used in the current numerical scheme. Since the DETE uses the same reconstruction process as the flow solution, there may be oscillations in the DETE solution that are compounded by those found in the flow solution. It is not immediately known if adding a limiter would reduce the oscillations in both the flow and DETE solutions, or if some additional oscillation may be a result of the residual models themselves.

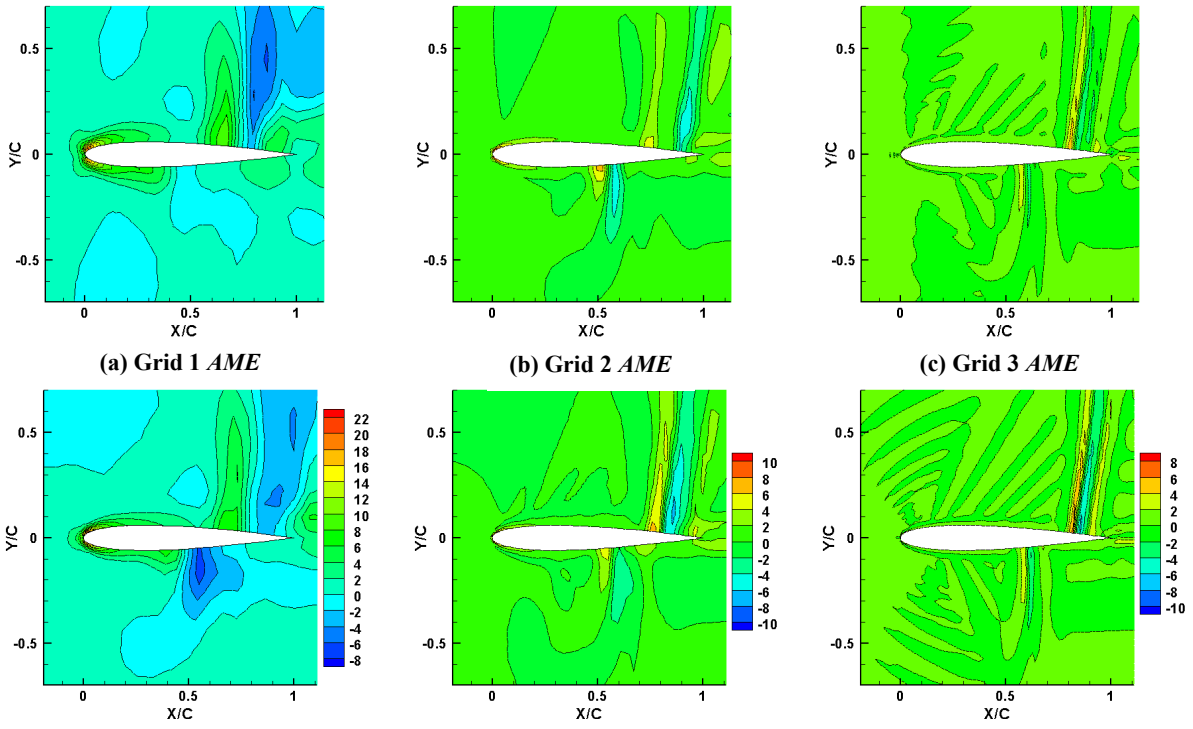

(a) Grid 1 *AME* **(b) Grid 2 *AME*** **(c) Grid 3 *AME***

(d) Grid 2 – Grid 1 **(e) Grid 3 – Grid 2** **(f) Grid 4 – Grid 3**

Figure 6.14. DETE solutions using AME residual model and actual error in x-momentum (kg/m-s) for transonic airfoil problem

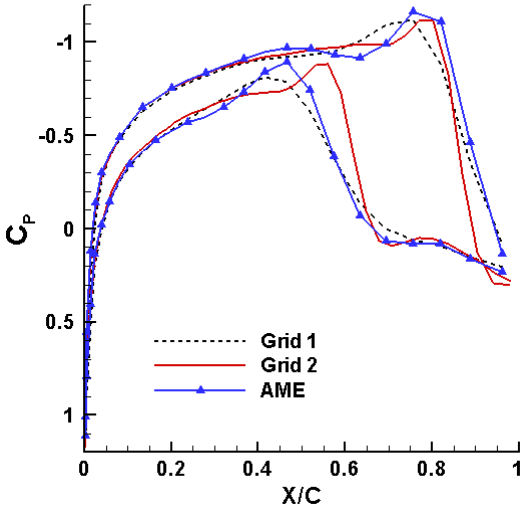

Figure 6.15. Pressure coefficient on surface of airfoil, DETE results on Grid 1 using AME residual model

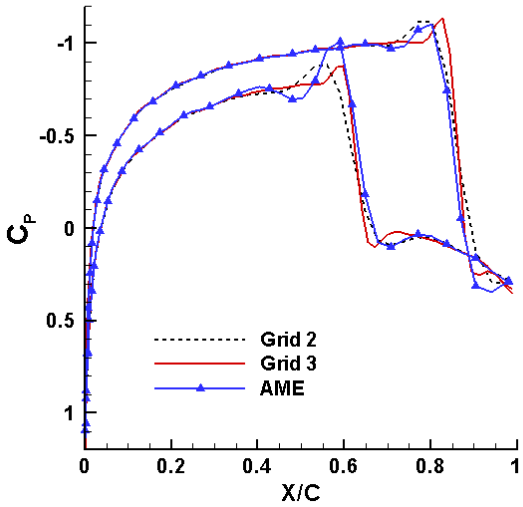

Figure 6.16. Pressure coefficient on surface of airfoil, DETE results on Grid 2 using AME residual model

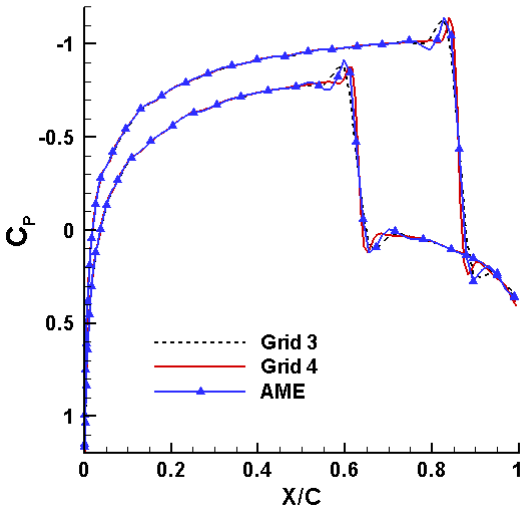

Figure 6.17. Pressure coefficient on surface of airfoil, DETE results on Grid 3 using AME residual model

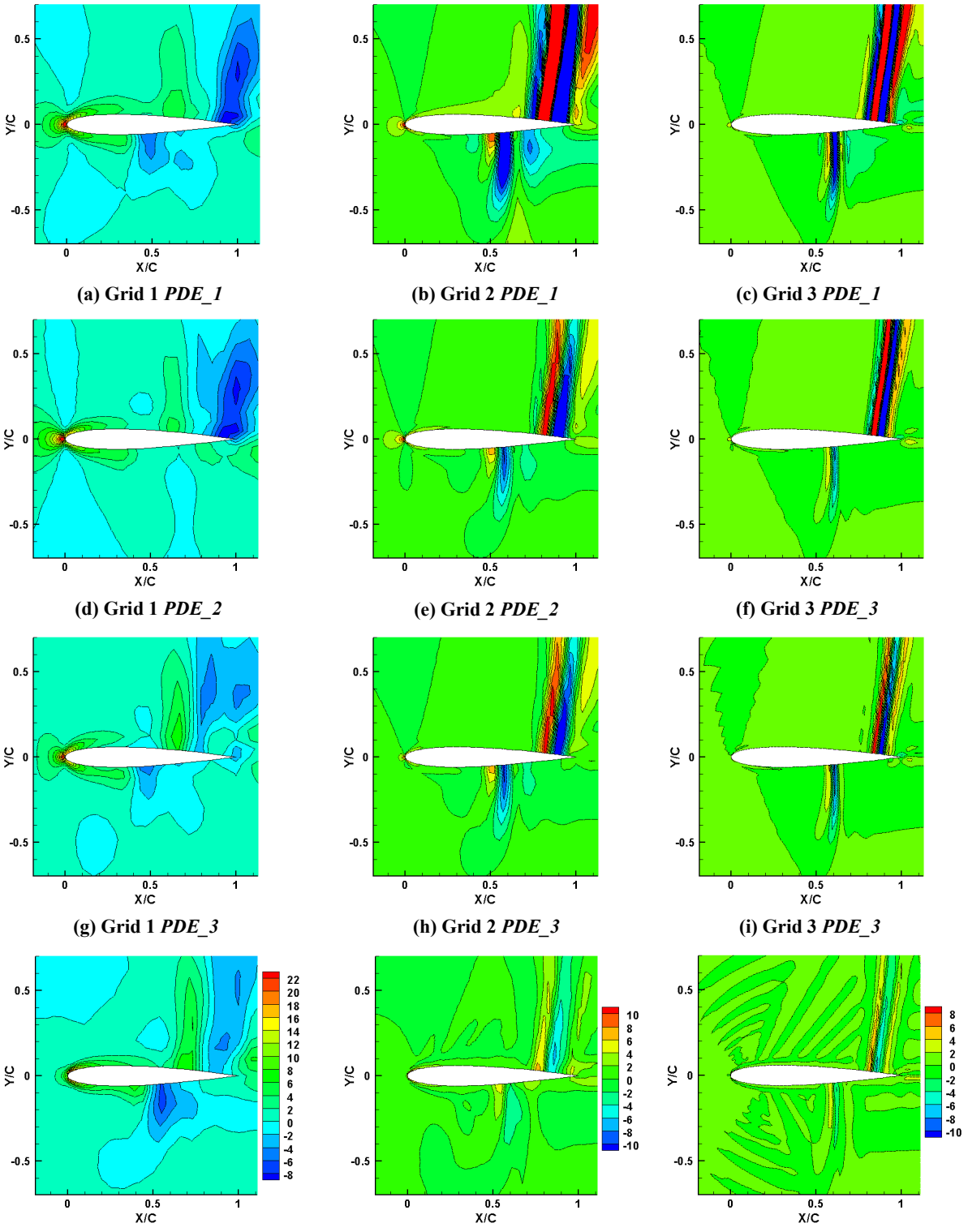

(a) Grid 1 *PDE_1* (b) Grid 2 *PDE_1* (c) Grid 3 *PDE_1*

(d) Grid 1 *PDE_2* (e) Grid 2 *PDE_2* (f) Grid 3 *PDE_3*

(g) Grid 1 *PDE_3* (h) Grid 2 *PDE_3* (i) Grid 3 *PDE_3*

(j) Grid 2 - Grid 1 (k) Grid 3 - Grid 2 (l) Grid 4 - Grid 3

Figure 6.18. DETE solutions using PDE residual model and actual error in x-momentum (kg/m-s) for transonic airfoil problem

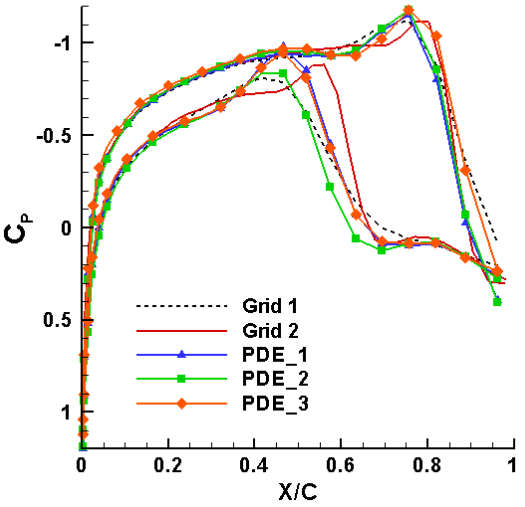

Figure 6.19. Pressure coefficient on surface of airfoil, DETE results on Grid 1 using PDE residual model

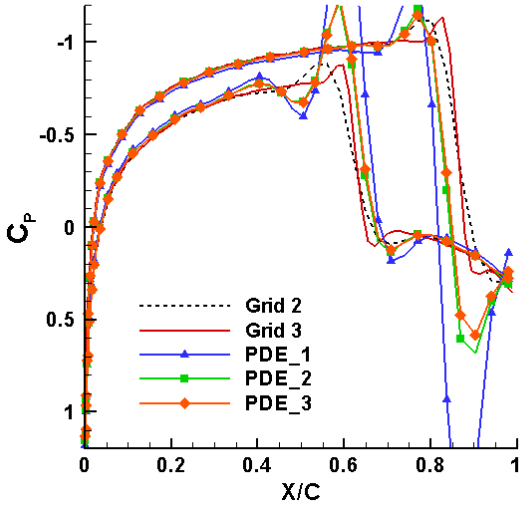

Figure 6.20. Pressure coefficient on surface of airfoil, DETE results on Grid 2 using PDE residual model

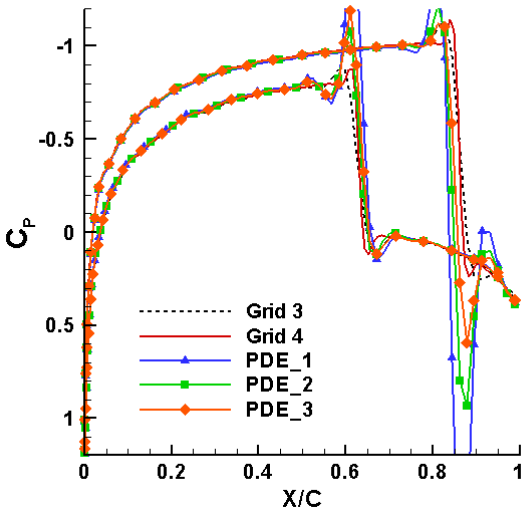

Figure 6.21. Pressure coefficient on surface of airfoil, DETE results on Grid 3 using PDE residual model

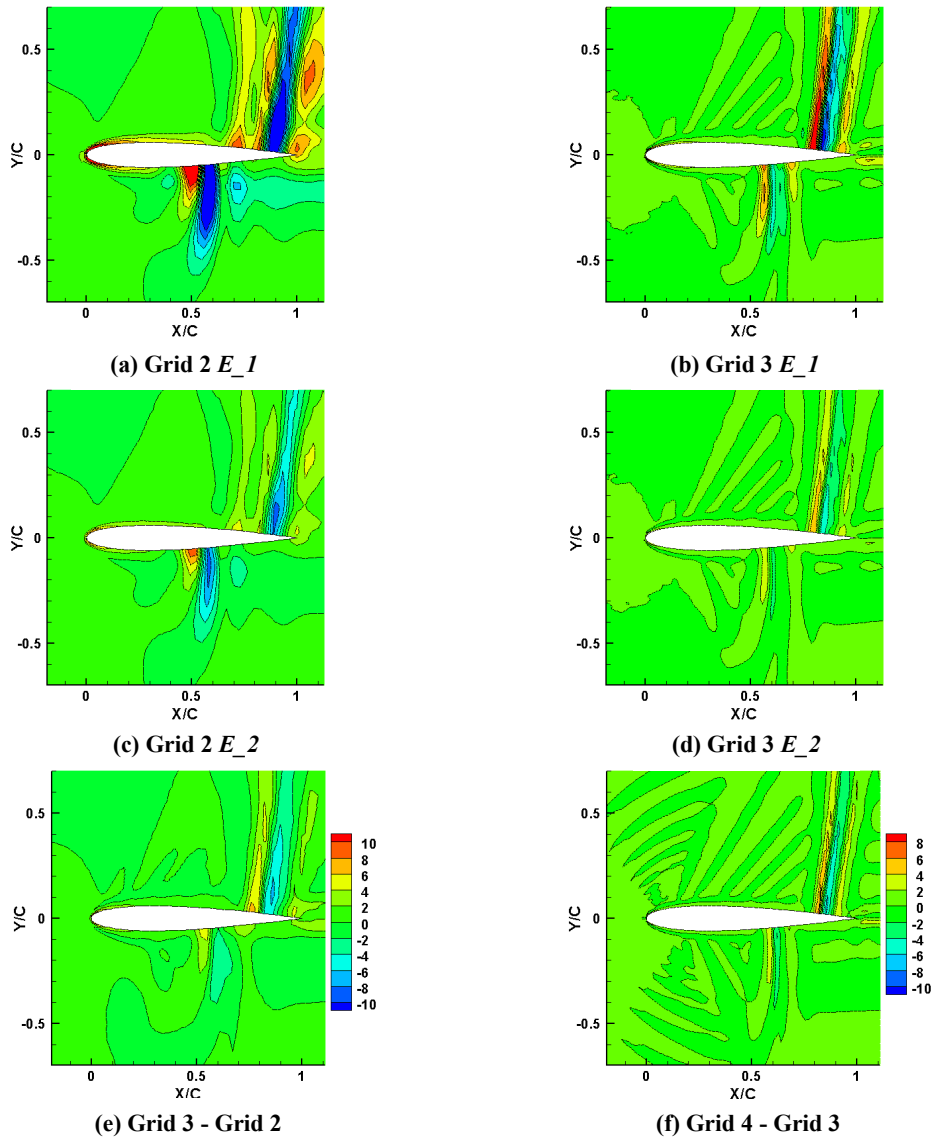

(a) Grid 2 *E_1*

(b) Grid 3 *E_1*

(c) Grid 2 *E_2*

(d) Grid 3 *E_2*

(e) Grid 3 - Grid 2

(f) Grid 4 - Grid 3

Figure 6.22. DETE solutions using extrapolation residual model and actual error in x-momentum (kg/m-s) for transonic airfoil problem

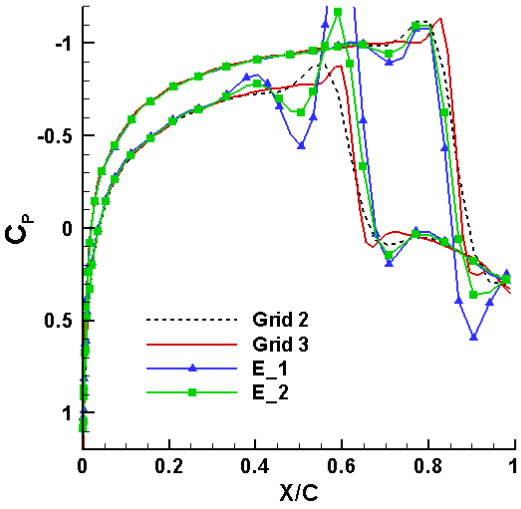

Figure 6.23. Pressure coefficient on surface of airfoil, DETE results on Grid 2 using extrapolation residual model

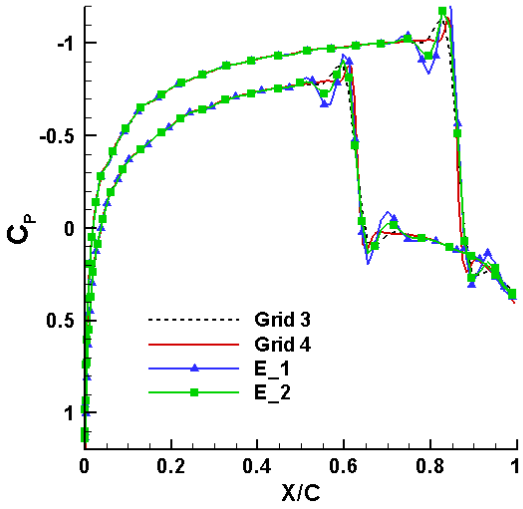

Figure 6.24. Pressure coefficient on surface of airfoil, DETE results on Grid 3 using extrapolation residual model

Unsteady Flow

Isentropic Vortex

Results for the isentropic vortex problem are presented at four different solution times: $t = 5.2$, 10, 15.2, and 20. DETE solutions on Grid 1 using the AME residual model are plotted in Figure 6.25(a), and are compared with the actual error in x-momentum relative to the Grid 2 flow solution in Figure 6.25(b). The DETE solutions on Grid 2 are shown in Figure 6.26(a), and compared with the actual error relative to the Grid 3 flow solution in Figure 6.26(b). The Grid 1 DETE results generally under-predict the magnitude of the error, similar to the steady flow results, but are closer to the actual error values at the earlier solution times. The Grid 2 DETE results, however, slightly over-predict the magnitude of the error, which, again, highlights the grid-dependency of the AME model. DETE solutions on both grids seem to predict the location of error well.

The DETE solutions on Grid 1 using the PDE residual model with each polynomial fit are given in Figure 6.27(a-c), and compared with the actual error in x-momentum relative to the Grid 2 flow solution in Figure 6.27(d). The Grid 2 DETE solutions are shown in Figure 6.28(a-c), compared to the actual error relative to the Grid 3 solution in Figure 6.28(d). For this problem, the *PDE_1* and *PDE_2* solutions behave very similarly, and are much more accurate than the *PDE_3* solution on Grid 1. On Grid 2, however, the *PDE_3* solution agrees better with the actual error than the other two

solutions. This is most likely a result of grid spacing and the stencil used for the least squares polynomial fit. On Grid 1, the stencil required for the third degree polynomial is of comparable size to the vortex itself, so the data variation is smeared out by the least squares fit. As the grid is refined, and the physical size of the stencil is reduced so that it contains a less varied set of data, the least squares fit will be better.

Figure 6.29(a,b) presents the DETE solutions on Grid 2 using the extrapolation model, compared with the actual error in x-momentum relative to the Grid 3 flow solution in Figure 6.29(c). As in the steady flow problems, the *E_1* results greatly over-predict the magnitude of the error. The *E_2* results agree with the actual error best out of all the residual models, which could be expected since it was shown in Chapter 2 that the solution to this problem converges globally at a near second-order rate.

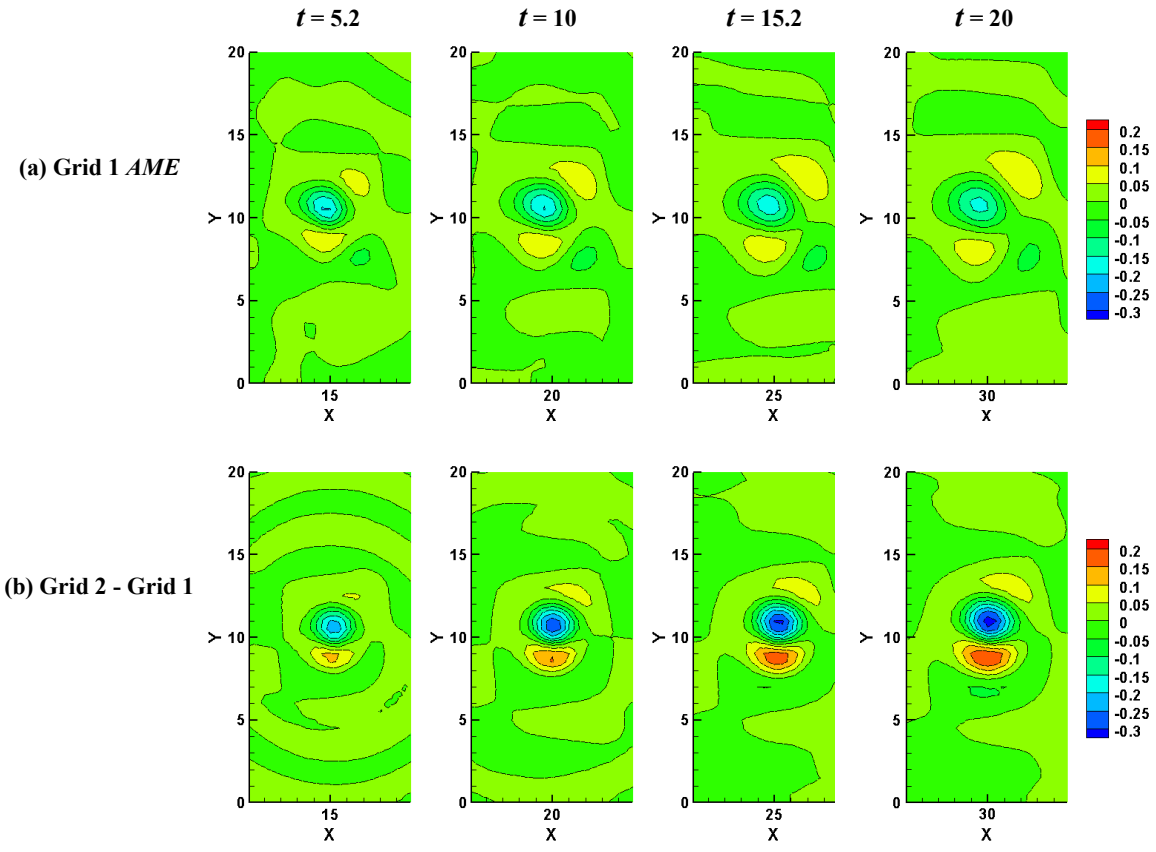

Figure 6.25. DETE solutions on Grid 1 using AME residual model and actual error in x-momentum (kg/m-s) for unsteady isentropic vortex problem

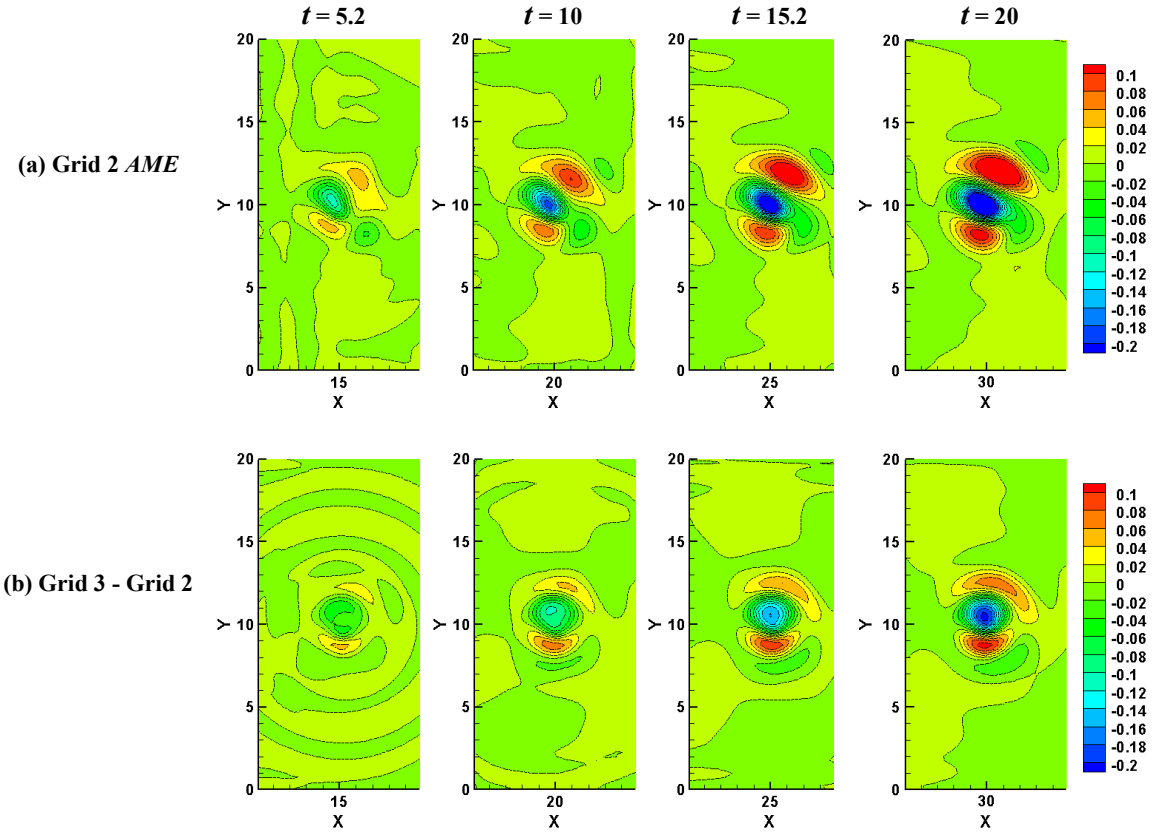

Figure 6.26. DETE solutions on Grid 2 using AME residual model and actual error in x-momentum (kg/m-s) for unsteady isentropic vortex problem

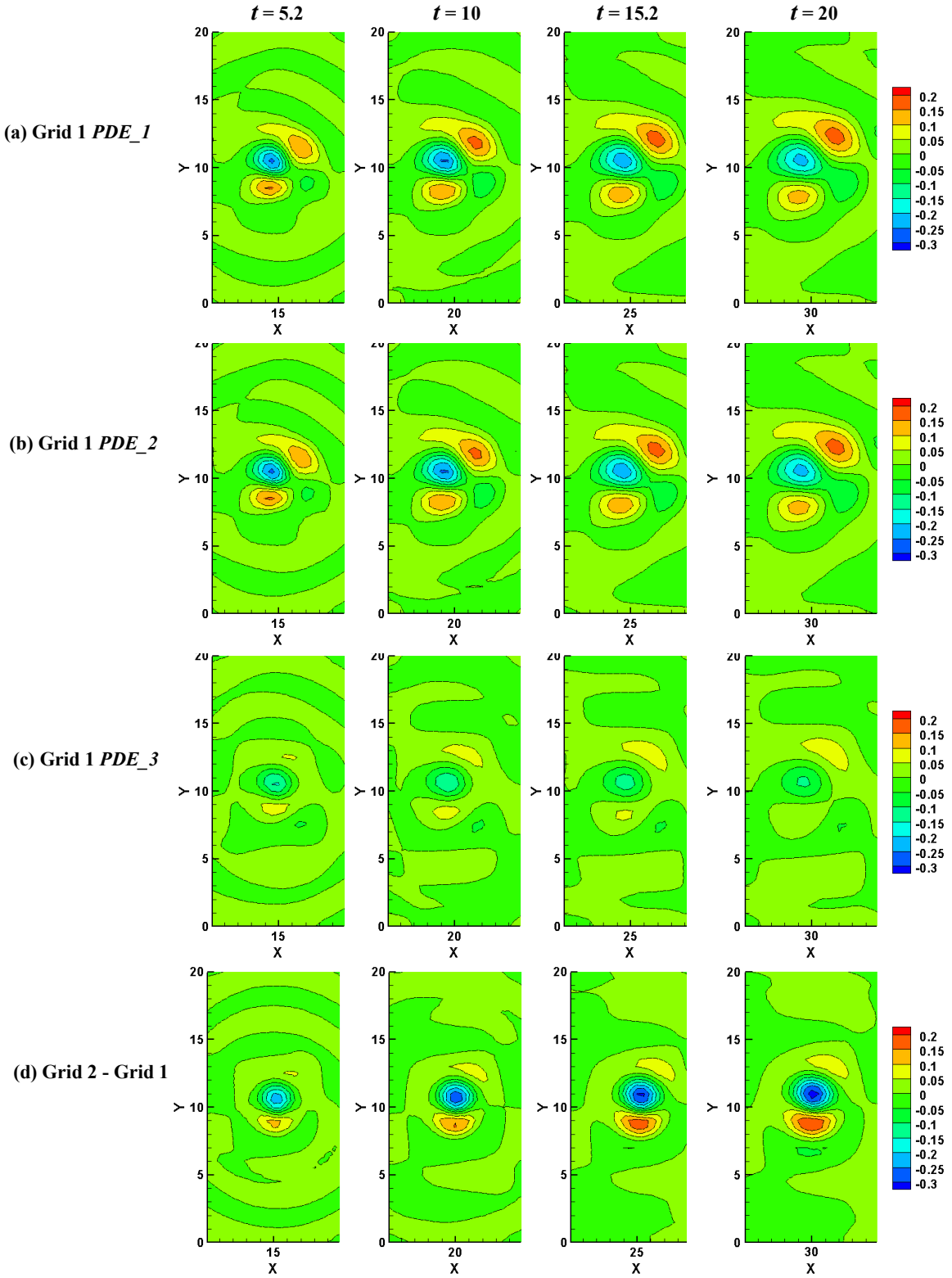

Figure 6.27. DETE solutions on Grid 1 using PDE residual model and actual error in x-momentum (kg/m-s) for unsteady isentropic vortex problem

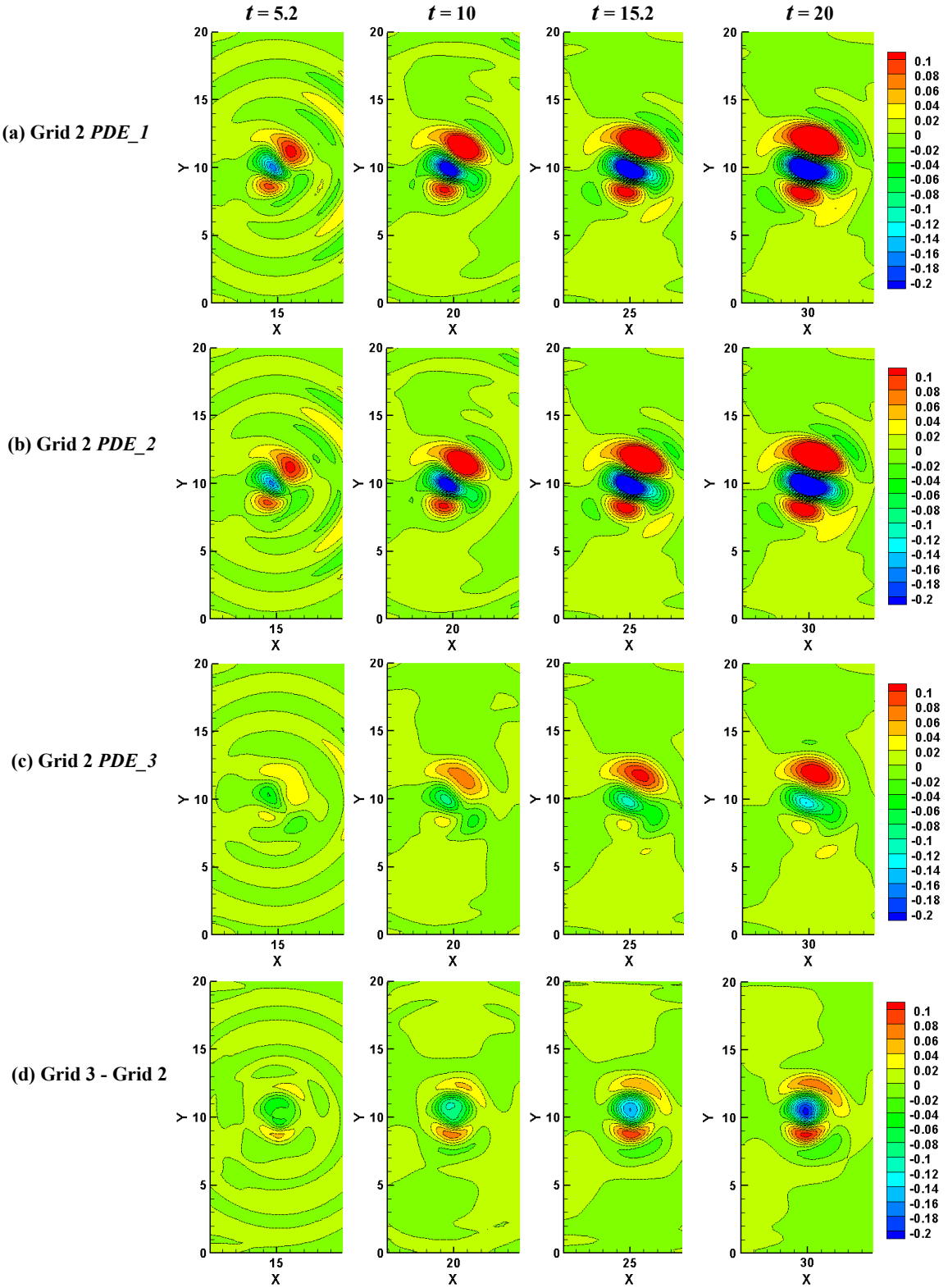

Figure 6.28. DETE solutions on Grid 2 using PDE residual model and actual error in x-momentum (kg/m-s) for unsteady isentropic vortex problem

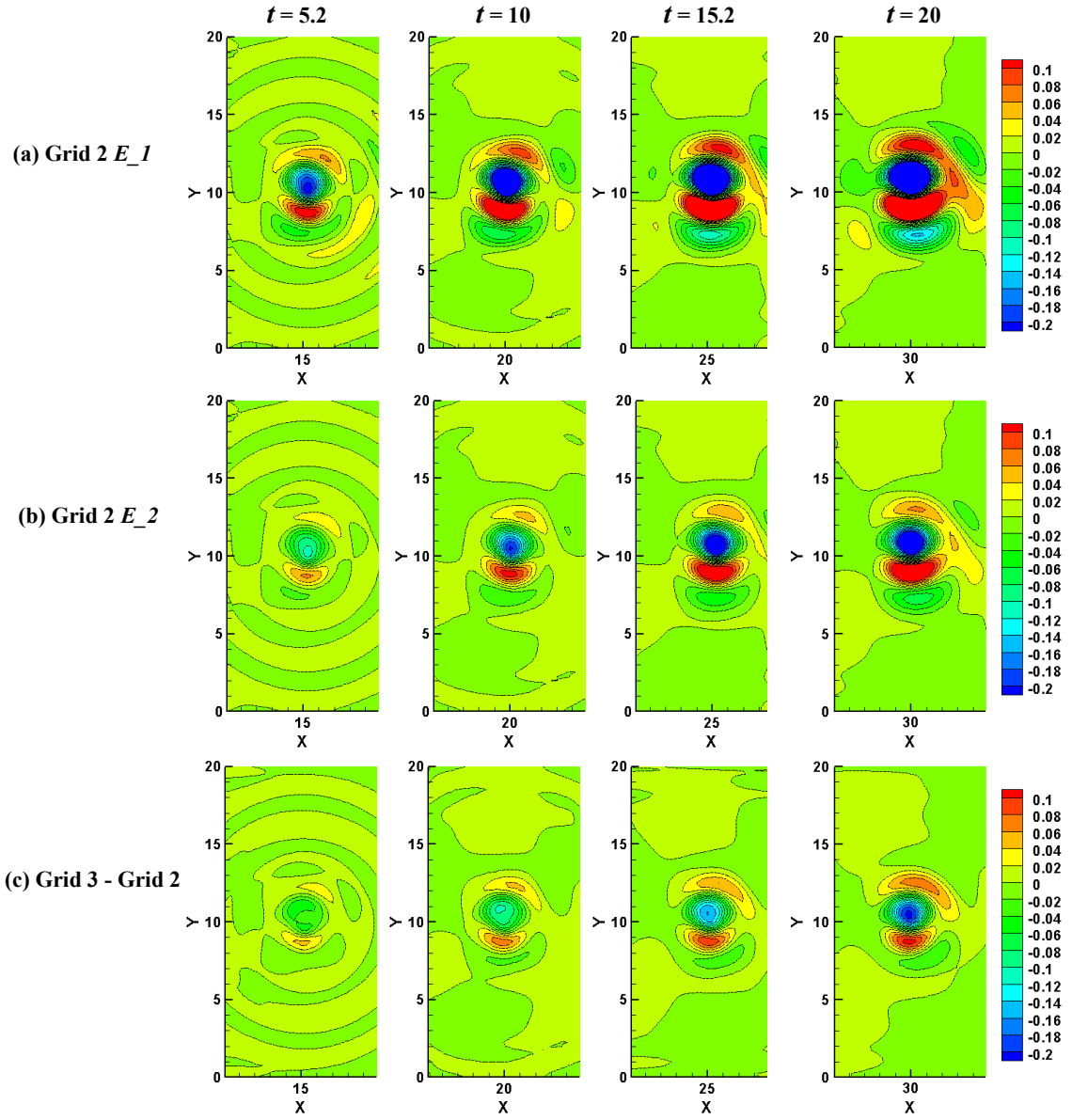

Figure 6.29. DETE solutions on Grid 2 using extrapolation residual model and actual error in x-momentum (kg/m-s) for unsteady isentropic vortex problem

Unsteady Circular Cylinder

The unsteady cylinder problem presents an extra challenge for the residual models. Since the frequency of the vortex shedding is dependent on the grid spacing, the residual model must be able to account for changes in the spatial and temporal behavior of the solution. The DETE solutions for Grid 1 with the *AME* and *PDE_3* residual models are presented for $t = 0.5$, 1, 1.5, and 2 in Figure 6.30(a) and Figure 6.31(a), and are compared with the actual error relative to the Grid 2 solution. These residual models were chosen because they performed well in the previous problems studied, but also because their results for this problem are representative of the other models. The *AME* and *PDE_3* results behave very similarly. Initially, the magnitude of the error is under-predicted, but as the solution progresses, the error magnitude continues to grow and becomes greatly over-predicted. In both sets of solutions, the location and sign of the error are incorrect in some areas, which is likely caused by the residual model not predicting the change in the frequency of the shedding. The lift coefficient time histories of the DETE solutions are compared with the flow solutions in Figure 6.32. While the Grid 1 flow solution reaches a periodic state around $t = 1$, the oscillations of the DETE solution continue to grow in magnitude at what appears to be a steady rate.

The same phenomenon is observed in the Grid 2 lift coefficient time histories of the *AME*, *PDE_3*, and *E_2* DETE solutions in Figure 6.33. It was expected that the *E_2* results would outperform the others because, by using the exact residual on the coarse grid, the extrapolation model contains the difference in time dependent behavior between the coarse and fine grid flow solutions. The grid-induced residual that is scaled in the extrapolation model was also shown to be able to accurately predict the error between the coarse and fine grids during the validation of the DETE in Chapter 4. When the exact residual is interpolated to the fine grid and scaled; however, the accuracy of the residual seems to be lost. In fact, these results show magnitude of the *E_2* error solution grows faster than the solutions using the other two residual models.

Since the residual models perform well in previous problems where the time dependent behavior of the problem is unchanged, it must be assumed that the poor performance of the DETE solutions in this case must be due to this aspect of the solutions. This could be a serious limitation to the usefulness of the DETE for unsteady problems and future research should investigate the time dependency of the residual models.

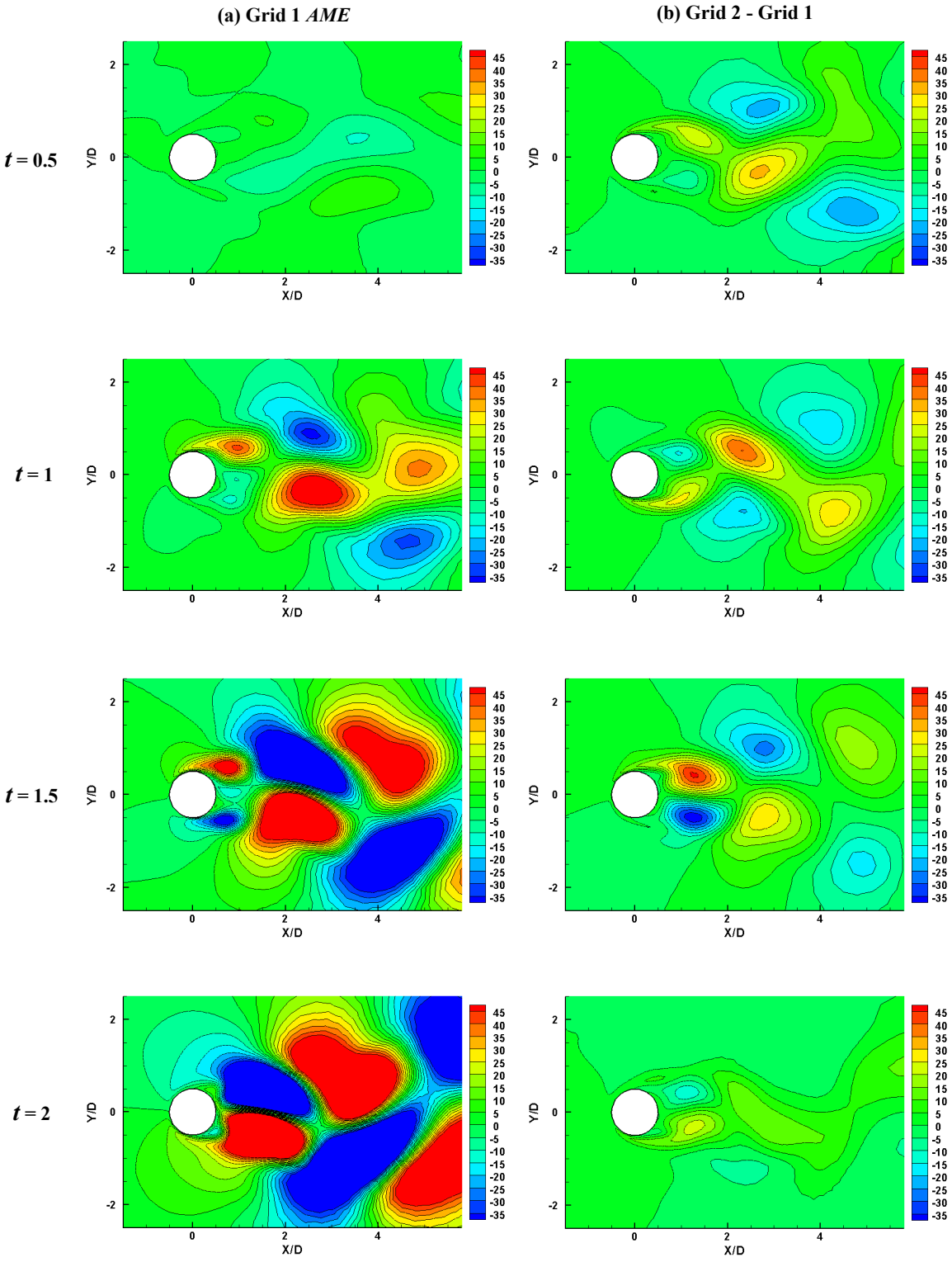

Figure 6.30. DETE solutions on Grid 1 using AME residual model and actual error in x-momentum (kg/m-s) for unsteady cylinder problem

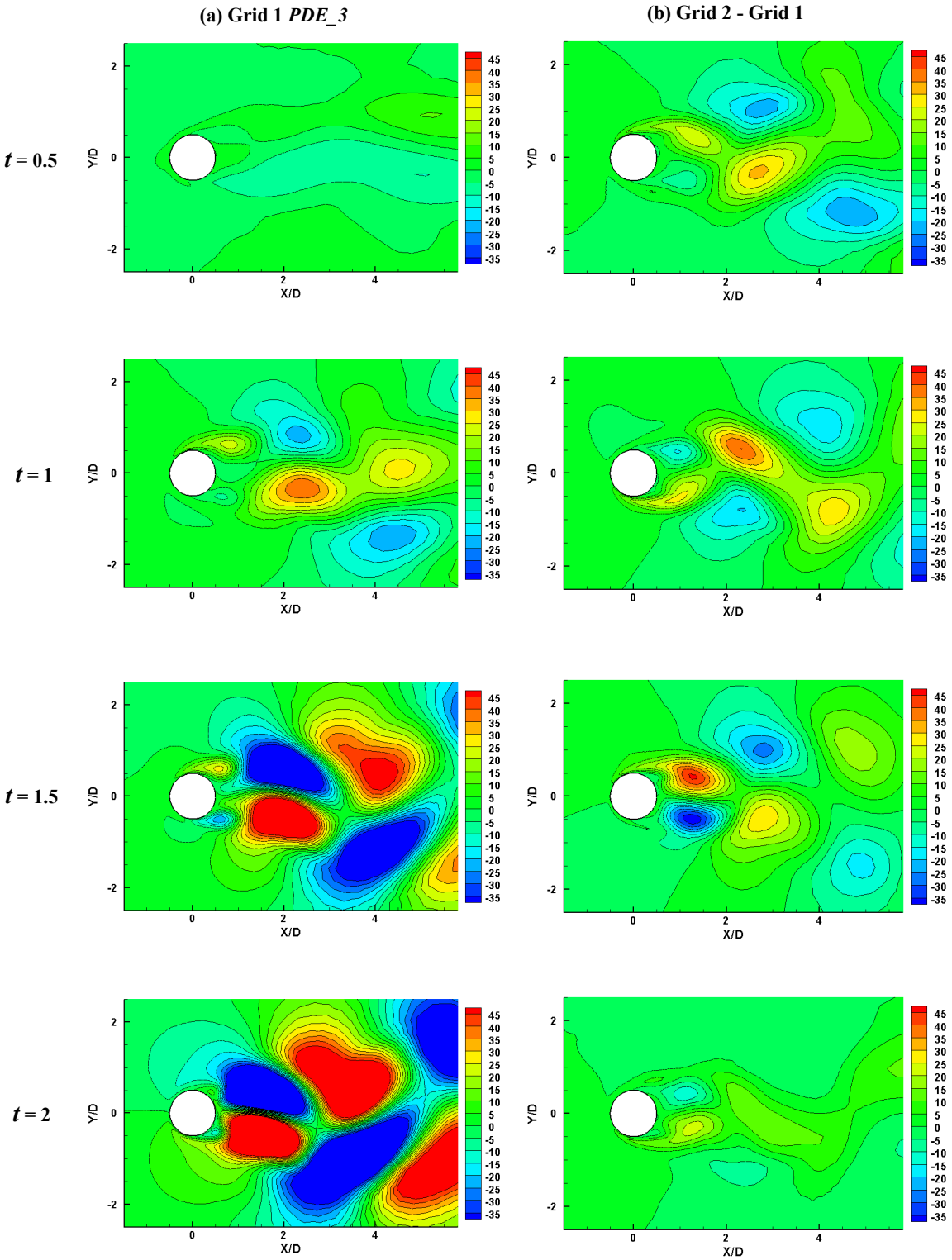

Figure 6.31. DETE solutions on Grid 1 using PDE residual model and actual error in x-momentum (kg/m-s) for unsteady cylinder problem

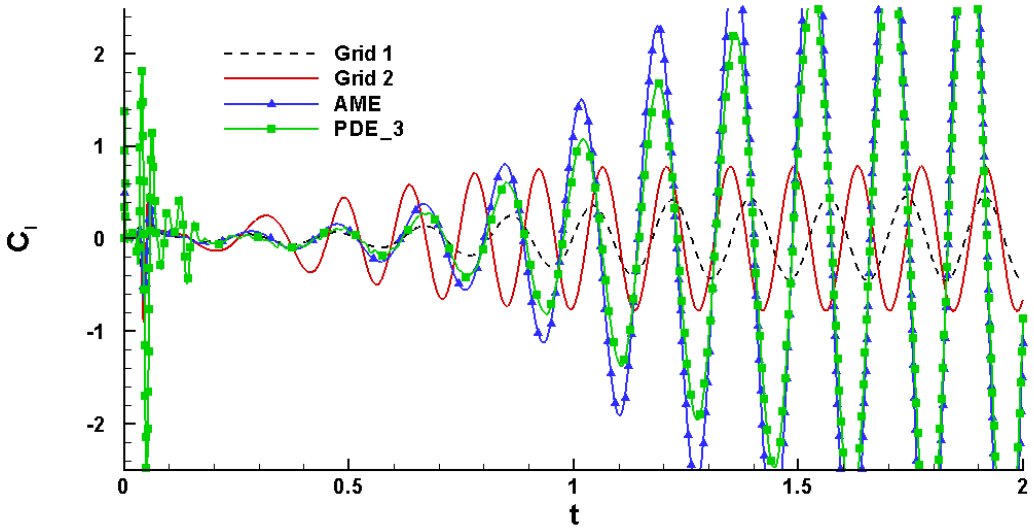

Figure 6.32. Time history of lift coefficient, DETE solutions on Grid 1 using AME and PDE residual models

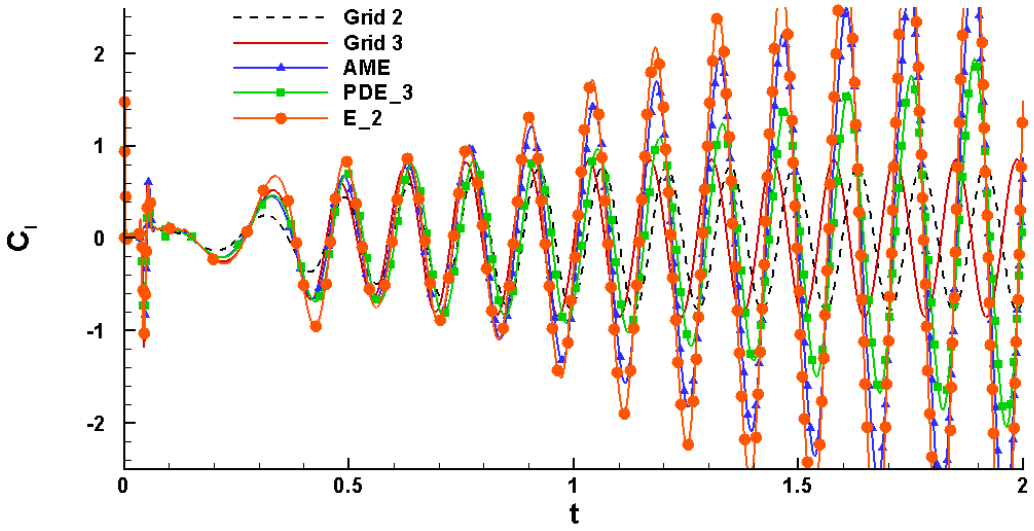

Figure 6.33. Time history of lift coefficient, DETE solutions on Grid 2 using AME and PDE residual models

Chapter 7. Summary

For computational fluid dynamics (CFD) to become a widely accepted design tool, some quantification of the numerical uncertainty in a solution must be available. Error sources include improper modeling of flow physics or boundary conditions, spatial and temporal inaccuracies in the numerical scheme, and computational grids with insufficient resolution or poor-quality cells. While an experienced engineer can easily choose the correct physical models, boundary conditions, and numerical scheme, it is often impossible to attenuate the effects of the grid à priori. One could certainly create a grid which is fine enough to generate a grid-independent solution and eliminate the grid as a source of error, but time and computational resource limitations make this approach impractical. Therefore it is necessary to have a method of estimating the uncertainty of a CFD solution for the types of problems and grids used in engineering applications.

This study presents an approach for estimating the grid-induced error of CFD solutions which is based on the discrete error transport equation (DETE). The DETE is derived on the discretized flow equations, and describes the transport of error throughout the computational domain which is generated by the grid-induced residual. A DETE for the laminar, compressible, Navier-Stokes equations has been derived within the framework of an unstructured finite volume scheme which is second-order accurate in space and time. The accuracy of the DETE scheme was then demonstrated through a series of test problems by using exact values of the residual.

The usefulness of the DETE depends on the accuracy with which the grid-induced residual can be modeled. Three different residual models were presented; two based on a single grid and flow solution, and one based on two grids and solutions. The approximate modified equation (AME) model uses the difference between the differential and discretized forms of the governing PDE to estimate the residual in a computational cell. The PDE model creates a least squares polynomial fit of the data in a localized stencil surrounding each cell and then evaluates the differential form of the governing PDE with that polynomial fit. Wherever the polynomial fit does not satisfy the governing PDE, the model produces a residual. The extrapolation model uses the exact value of the grid-induced residual which may be found using two different grids and solutions and then extrapolates that residual from the coarse grid to the fine grid by scaling it according to the formal order of accuracy of the numerical scheme.

Each residual model was evaluated with four test problems: (1) steady, laminar flow past a circular cylinder; (2) steady, transonic, inviscid flow past an airfoil; (3) unsteady, inviscid flow of an isentropic vortex; (4) unsteady, laminar flow past a circular cylinder.

For the steady cylinder problem, the AME and PDE residual models performed best in the region near the cylinder where the grid resolution was quite fine. While these models still predicted the general distribution of error elsewhere, the extrapolation model was more accurate in predicting the magnitude of the error in the wake region downstream of the cylinder where the grid was coarser.

The results for the transonic airfoil problem showed the AME residual model worked best overall, although the extrapolation model worked equally well as the grid was more refined. The PDE model introduced large oscillations in the solution near the shocks on the top and bottom of the airfoil. This is most likely due to the fact that the stencil of cells used to create the polynomial fit straddled the discontinuity of the shock, creating a poor least squares representation of the data. In the future, this problem could be avoided using strategies common to high-order finite volume schemes which alter the stencils of cells near shock so that they do not include the discontinuity.

In the case of the isentropic vortex, the extrapolation model performed best of all the models tested on the finer grid. This problem was shown to converge at (or above) a second-order rate; therefore, it should be expected in this case that the exact residual from the coarse grid scaled by the formal order of accuracy would approximate the exact residual on the fine grid. On the coarsest grid, where the extrapolation model cannot be used, results were mixed for the AME and PDE models. The size of the stencil used for the third degree polynomial fit on the coarse grid seemed to smear out the variation of the data, since it was approximately the same size as the vortex itself. In this case, the PDE model with first and second degree polynomial fits worked best since the stencil is much smaller. Both the AME model and the PDE model with a third degree polynomial fit worked better on the fine grid, however.

The unsteady cylinder problem with periodic vortex shedding draws attention to one of the current limitations of these residual models. The frequency of the vortex shedding changes with the grid resolution, which means the problem is both spatially and temporally dependent on the grid. During the validation of the DETE, it was shown that the error would reach a stable periodic state along with the flow, and the fine grid solution could be recovered using the exact residual. Each of the residual models produced a DETE solution that became periodic, but the magnitude of the oscillations grew in time. The appearance is similar to what one would expect if error were accumulating: new error is continually produced but never dissipated, so it continues to add to the existing error. Since the DETE was shown to work well with the exact residual, and the residual models are fairly accurate for the other problems studied, it seems straightforward to assume the residual models do not properly account for the changing time dependent behavior of this problem.

Future research should be conducted to better understand the nature of the time dependency of the residual, and improve the state of residual modeling.

Overall, the PDE model using a first degree polynomial fit and the extrapolation model with a first-order rate of convergence performed poorly in comparison to the actual error and the DETE results using other residual models.

The DETE using the various residual models has been shown to provide meaningful error estimates for a variety of flow problems. While the predicted error was not the total grid-induced error (the error relative to a grid-independent solution), the DETE solution does generally compare well with the actual error relative to a single level of uniform grid refinement. This estimation can supply valuable information about the sensitivity of the solution to changes in grid spacing, and therefore can be used to decide whether further grid refinement is necessary.

Appendix A

The Jacobian matrices used in the linearization of the residual operator for the DETE are detailed here, reproduced from information provided in a textbook by Chung [38]. Beginning with the convective terms:

$$\left(\frac{\partial \boldsymbol{f}}{\partial Q}\right)_x = \begin{bmatrix} 0 & 1 & 0 & 0 \\ \frac{\gamma-3}{2}u^2+\frac{\gamma-1}{2}v^2 & (3-\gamma)u & (1-\gamma)v & \gamma-1 \\ -uv & v & u & 0 \\ (\gamma-1)\left(u^2+v^2\right)u-\frac{\gamma uE}{\rho} & \frac{1-\gamma}{2}\left(3u^2+v^2\right)+\frac{\gamma E}{\rho} & (1-y)uv & \gamma u \end{bmatrix} \tag{A.1}$$

$$\left(\frac{\partial \boldsymbol{f}}{\partial Q}\right)_y = \begin{bmatrix} 0 & 0 & 1 & 0 \\ -uv & v & u & 0 \\ \frac{\gamma-3}{2}v^2+\frac{\gamma-1}{2}u^2 & (1-\gamma)u & (3-\gamma)v & \gamma-1 \\ (\gamma-1)\left(u^2+v^2\right)v-\frac{\gamma vE}{\rho} & (1-\gamma)uv & \frac{1-\gamma}{2}\left(3v^2+u^2\right)+\frac{\gamma E}{\rho} & \gamma v \end{bmatrix} \tag{A.2}$$

For the diffusion terms, define the following quantities:

$$\lambda = -2/3\,\mu \tag{A.3}$$

$$\vartheta = \lambda + 2\mu \tag{A.4}$$

Then the diffusion term Jacobians are:

$$b^1 = \left(\frac{\partial \boldsymbol{g}}{\partial Q}\right)_x = \begin{bmatrix} 0 & 0 & 0 & 0 \\ b_{21}^1 & b_{22}^1 & b_{23}^1 & 0 \\ b_{31}^1 & b_{32}^1 & b_{33}^1 & 0 \\ b_{41}^1 & b_{42}^1 & b_{43}^1 & b_{44}^1 \end{bmatrix}, \quad b^2 = \left(\frac{\partial \boldsymbol{g}}{\partial Q}\right)_y = \begin{bmatrix} 0 & 0 & 0 & 0 \\ b_{21}^2 & b_{22}^2 & b_{23}^2 & 0 \\ b_{31}^2 & b_{32}^2 & b_{33}^2 & 0 \\ b_{41}^2 & b_{42}^2 & b_{43}^2 & b_{44}^2 \end{bmatrix} \tag{A.5}$$

where,

$$b_{21}^1 = -\frac{1}{\rho^2}\left[-\vartheta\left(\rho u\right)_x - \lambda\left(\rho v\right)_y + 2\vartheta u\rho_x + 2\lambda v\rho_y\right] \tag{A.6}$$

$$b_{22}^1 = \frac{\vartheta}{\rho^2}\rho_x \tag{A.7}$$

$$b_{23}^{1} = \frac{\lambda}{\rho^2}\rho_y \tag{A.8}$$

$$b_{31}^{1} = -\frac{\mu}{\rho^2}\left[-\left(\rho v\right)_x - \left(\rho u\right)_y + 2u\rho_y + 2v\rho_x\right] \tag{A.9}$$

$$b_{32}^{1} = \frac{\mu}{\rho^2}\rho_y \tag{A.10}$$

$$b_{33}^{1} = \frac{\mu}{\rho^2}\rho_x \tag{A.11}$$

$$\begin{aligned} b_{41}^{1} = {} & u b_{21}^{1} + v b_{31}^{1} - \frac{1}{\rho^2}\left[\left(\rho u\right)\tau_{xx} + \left(\rho v\right)\tau_{xy}\right] \\ & + \frac{\mu\gamma}{\rho^2\,\mathrm{Pr}}\left[-E_x + 2\mu\left(\rho u\right)_x + 2v\left(\rho v\right)_x + \left(2\frac{E}{\rho} - 3u^2 - 3v^2\right)\rho_x\right] \end{aligned} \tag{A.12}$$

$$b_{42}^{1} = -\frac{\tau_{xx}}{\rho} + u b_{22}^{1} + v b_{32}^{1} + \frac{\mu\gamma}{\rho^2\,\mathrm{Pr}}\left[-\left(\rho u\right)_x + 2u\rho_x\right] \tag{A.13}$$

$$b_{43}^{1} = -\frac{\tau_{xy}}{\rho} + u b_{23}^{1} + v b_{33}^{1} - \frac{\mu\gamma}{\rho^2\,\mathrm{Pr}}\left[-\left(\rho v\right)_x + 2v\rho_x\right] \tag{A.14}$$

$$b_{44}^{1} = \frac{\mu\gamma}{\rho^2\,\mathrm{Pr}}\rho_x \tag{A.15}$$

$$b_{21}^{2} = b_{31}^{1} \tag{A.16}$$

$$b_{22}^{2} = b_{32}^{1} \tag{A.17}$$

$$b_{23}^{2} = b_{33}^{1} \tag{A.18}$$

$$b_{31}^{2} = \frac{1}{\rho^2}\left[\lambda\left(\rho u\right)_x + \vartheta\left(\rho v\right)_y + \vartheta u\rho_x - \vartheta v\rho_y\right] \tag{A.19}$$

$$b_{32}^{2} = \frac{\lambda}{\rho^2}\rho_x \tag{A.20}$$

$$b_{33}^{2} = \frac{\vartheta}{\rho^2}\rho_y \tag{A.21}$$

$$b_{41}^2 = ub_{21}^2 + vb_{31}^2 + \frac{1}{\rho^2}\left[(\rho u)\tau_{xy} + (\rho v)\tau_{yy}\right] - \frac{\mu\gamma}{\rho^2 \,\mathrm{Pr}}\left[-E_y + 2u(\rho u)_x + 2v(\rho v)_y + \left(2\frac{E}{\rho} - 3u^2 - 3v^2\right)\rho_y\right] \tag{A.22}$$

$$b_{42}^2 = -\frac{\tau_{xy}}{\rho} + ub_{22}^2 - vb_{32}^2 + \frac{\mu\gamma}{\rho^2 \,\mathrm{Pr}}\left[-(\rho u)_y + 2u\rho_y\right] \tag{A.23}$$

$$b_{43}^2 = -\frac{\tau_{yy}}{\rho} + ub_{23}^2 + vb_{33}^2 - \frac{\mu\gamma}{\rho^2 \,\mathrm{Pr}}\left[-(\rho v)_y + 2v\rho_y\right] \tag{A.24}$$

$$b_{44}^2 = \frac{\mu\gamma}{\rho^2 \,\mathrm{Pr}}\rho_y \tag{A.25}$$

The diffusion gradient Jacobians are written as:

$$c^{11} = \left(\frac{\partial \boldsymbol{g}}{\partial \nabla Q_x}\right)_x = -\begin{bmatrix} 0 & 0 & 0 & 0 \\ c_{21}^{11} & c_{22}^{11} & 0 & 0 \\ c_{31}^{11} & 0 & c_{33}^{11} & 0 \\ c_{41}^{11} & c_{42}^{11} & c_{43}^{11} & c_{44}^{11} \end{bmatrix} \qquad c^{12} = \left(\frac{\partial \boldsymbol{g}}{\partial \nabla Q_y}\right)_x = -\begin{bmatrix} 0 & 0 & 0 & 0 \\ c_{21}^{12} & 0 & c_{23}^{12} & 0 \\ c_{31}^{12} & c_{32}^{12} & 0 & 0 \\ c_{41}^{12} & c_{42}^{12} & c_{43}^{12} & 0 \end{bmatrix}$$

$$c^{21} = \left(\frac{\partial \boldsymbol{g}}{\partial \nabla Q_x}\right)_y = -\begin{bmatrix} 0 & 0 & 0 & 0 \\ c_{21}^{21} & 0 & c_{23}^{21} & 0 \\ c_{31}^{21} & c_{32}^{21} & 0 & 0 \\ c_{41}^{21} & c_{42}^{21} & c_{43}^{21} & 0 \end{bmatrix} \qquad c^{22} = \left(\frac{\partial \boldsymbol{g}}{\partial \nabla Q_y}\right)_y = -\begin{bmatrix} 0 & 0 & 0 & 0 \\ c_{21}^{22} & c_{22}^{22} & 0 & 0 \\ c_{31}^{22} & 0 & c_{33}^{22} & 0 \\ c_{41}^{22} & c_{42}^{22} & c_{43}^{22} & c_{44}^{22} \end{bmatrix} \tag{A.26}$$

where,

$$c_{21}^{11} = -\vartheta\frac{u}{\rho} \tag{A.27}$$

$$c_{22}^{11} = \frac{\vartheta}{\rho} \tag{A.28}$$

$$c_{31}^{11} = -\mu\frac{v}{\rho} \tag{A.29}$$

$$c_{33}^{11} = \frac{\mu}{\rho} \tag{A.30}$$

$$c_{41}^{11} = -\vartheta\frac{u^2}{\rho} - \mu\frac{v^2}{\rho} + \frac{\mu\gamma}{\rho\,\mathrm{Pr}}\left[\frac{E}{\rho} + u^2 + v^2\right] \tag{A.31}$$

$$c_{42}^{11} = \left(\vartheta - \frac{\mu\gamma}{\mathrm{Pr}}\right)\frac{u}{\rho} \tag{A.32}$$

$$c_{43}^{11} = \left(\mu - \frac{\mu\gamma}{\mathrm{Pr}}\right)\frac{v}{\rho} \tag{A.33}$$

$$c_{44}^{11} = \frac{\mu\gamma}{\rho\,\mathrm{Pr}} \tag{A.34}$$

$$c_{21}^{12} = -\lambda\frac{v}{\rho} \tag{A.35}$$

$$c_{23}^{12} = \frac{\lambda}{\rho} \tag{A.36}$$

$$c_{31}^{12} = -\mu\frac{u}{\rho} \tag{A.37}$$

$$c_{32}^{12} = \frac{\mu}{\rho} \tag{A.38}$$

$$c_{41}^{12} = -\left(\mu + \lambda\right)\frac{uv}{\rho} \tag{A.39}$$

$$c_{42}^{12} = \mu\frac{v}{\rho} \tag{A.40}$$

$$c_{43}^{12} = \lambda\frac{u}{\rho} \tag{A.41}$$

$$c_{21}^{21} = -\mu\frac{v}{\rho} \tag{A.42}$$

$$c_{23}^{21} = \frac{\mu}{\rho} \tag{A.43}$$

$$c_{31}^{21} = -\lambda\frac{u}{\rho} \tag{A.44}$$

$$c_{32}^{21} = \frac{\lambda}{\rho} \tag{A.45}$$

$$c_{41}^{21} = -\left(\mu + \lambda\right)\frac{uv}{\rho} \tag{A.46}$$

$$c_{42}^{21} = \lambda\frac{v}{\rho} \tag{A.47}$$

$$c_{43}^{21} = \mu\frac{u}{\rho} \tag{A.48}$$

$$c_{21}^{22} = -\mu\frac{u}{\rho} \tag{A.49}$$

$$c_{22}^{22} = \frac{\mu}{\rho} \tag{A.50}$$

$$c_{31}^{22} = -\vartheta\frac{v}{\rho} \tag{A.51}$$

$$c_{33}^{22} = \frac{\vartheta}{\rho} \tag{A.52}$$

$$c_{41}^{22} = -\vartheta\frac{v^2}{\rho} - \mu\frac{u^2}{\rho} + \frac{\mu\gamma}{\rho\,\mathrm{Pr}}\left[-\frac{E}{\rho} + u^2 + v^2\right] \tag{A.53}$$

$$c_{42}^{22} = \left(\mu - \frac{\mu\gamma}{\mathrm{Pr}}\right)\frac{u}{\rho} \tag{A.54}$$

$$c_{43}^{22} = \left(\vartheta - \frac{\mu\gamma}{\mathrm{Pr}}\right)\frac{v}{\rho} \tag{A.55}$$

$$c_{44}^{22} = \frac{\mu\gamma}{\rho\,\mathrm{Pr}} \tag{A.56}$$

Appendix B

This section derives the least squares reconstruction technique used to fit cell average data on the computational grid. If some set of data, $F(\bar{x},\bar{y})$, is to be represented by a first degree polynomial, $G(\bar{x},\bar{y})$, centered about coordinates (x_c, y_c),

$$G(\bar{x},\bar{y}) = a_0 + a_1\bar{x} + a_2\bar{y} \tag{B.1}$$

where,

$$(\bar{x},\bar{y}) = (x,y) - (x_c, y_c) \tag{B.2}$$

then the least squares problem is described by:

$$E = \sum_{i=1}^{N}\left[F(\bar{x}_i,\bar{y}_i) - G(\bar{x}_i,\bar{y}_i)\right]^2 \tag{B.3}$$

$$\frac{\partial E}{\partial a_j} = 0 \tag{B.4}$$

Here, *N* denotes the number of data points to be used, and *j* is the index of the coefficients. Evaluating Eq. (B.4) for each coefficient creates a set of linear algebraic equations,

$$\begin{bmatrix} N & \sum\bar{x} & \sum\bar{y} \\ \sum\bar{x} & \sum\bar{x}^2 & \sum\bar{x}\bar{y} \\ \sum\bar{y} & \sum\bar{x}\bar{y} & \sum\bar{y}^2 \end{bmatrix}\begin{Bmatrix} a_0 \\ a_1 \\ a_2 \end{Bmatrix} = \begin{Bmatrix} \sum F \\ \sum F\bar{x} \\ \sum F\bar{y} \end{Bmatrix} \tag{B.5}$$

Solving Eq. (B.5) yields the values of the coefficients for the least squares function *G*. In this case, however, we wish to constrain these equations such that the coefficient a_0 is the value of the data at (x_c, y_c). Adding this constraint, the system becomes:

$$\begin{bmatrix} \sum\bar{x}^2 & \sum\bar{x}\bar{y} \\ \sum\bar{x}\bar{y} & \sum\bar{y}^2 \end{bmatrix}\begin{Bmatrix} a_1 \\ a_2 \end{Bmatrix} = \begin{Bmatrix} \sum\bar{F}\bar{x} \\ \sum\bar{F}\bar{y} \end{Bmatrix} \tag{B.6}$$

where,

$$\bar{F} = F(\bar{x},\bar{y}) - F(0,0) \tag{B.7}$$

This simple system can be solved algebraically for the coefficients,

$$a_1 = \frac{1}{\sum \bar{x}^2 \sum \bar{y}^2 - \left(\sum \bar{x}\bar{y}\right)^2}\left[\sum \bar{y}^2 \sum \bar{F}\bar{x} - \sum \bar{x}\bar{y} \sum \bar{F}\bar{y}\right] \tag{B.8}$$

$$a_2 = \frac{1}{\sum \bar{x}^2 \sum \bar{y}^2 - \left(\sum \bar{x}\bar{y}\right)^2}\left[\sum \bar{x}^2 \sum \bar{F}\bar{y} - \sum \bar{x}\bar{y} \sum \bar{F}\bar{x}\right] \tag{B.9}$$

It is possible to use this same procedure for higher order polynomial representations of G where it becomes more convenient to numerically solve for the coefficients. In this case, the greater number of unknowns not only increases the size of the algebraic system but can also cause conditioning problems with the left hand side matrix.

References

[1] J.C. Tannehill, D.A. Anderson, and R.H. Pletcher, *Computational Fluid Mechanics and Heat Transfer*, Taylor & Francis Group, 1997.

[2] P.J. Roache, *Verification and Validation in Computational Science and Engineering*, Albuquerque, NM: Hermosa, 1998.

[3] I. Celik and W.M. Zhang, "Calculation of Numerical Uncertainty Using Richardson Extrapolation: Application to Some Simple Turbulent Flow Calculations," *Journal of Fluids Engineering*, vol. 117, 1995, p. 439.

[4] I. Celik, C.J. Chen, P.J. Roache, and G. Scheurer, "Quantification of Uncertainty in Computational Fluid Dynamics," *Symposium on Quantification of Uncertainty in Computational Fluid Dynamics*, Washington, D.C.: ASME FED, vol. 158, 1993, pp. 20-24.

[5] R. Wilson and F. Stern, "Verification and Validation for RANS Simulation of a Naval Surface Combatant," *40th AIAA Aerospace Sciences Meeting & Exhibit*, AIAA Paper 2002-0904, 2002.

[6] I. Babuska and W.C. Rheinboldt, "Error Estimates for Adaptive Finite Element Computations," *SIAM Journal on Numerical Analysis*, vol. 15, 1978, pp. 736-754.

[7] G.F. Carey, *Computational Grids: Generation, Adaptation, and Solution Strategies*, CRC Press, 1997.

[8] J. Mackenzie, T. Sonar, and E. Suli, "Adaptive Finite Volume Methods for Hyperbolic Problems," *The Mathematics of Finite Elements and Applications*, John Wiley & Sons, 1993, pp. 289-298.

[9] J.T. Oden, "Error Estimation and Control in Computational Fluid Dynamics," *The Mathematics of Finite Elements and Applications*, John Wiley & Sons, 1993, pp. 1–23.

[10] J. Peraire, M. Vahdati, K. Morgan, and O.C. Zienkiewicz, "Adaptive Remeshing for Compressible Flow Computations," *Journal of Computational Physics*, vol. 72, 1987, pp. 449-466.

[11] T. Sonar, "Strong and Weak Norm Refinement Indicators Based on the Finite Element Residual for Compressible Flow Computation," *Impact of Computing in Science and Engineering*, vol. 5, 1993, pp. 111-127.

[12] D.A. Venditti and D.L. Darmofal, "Adjoint Error Estimation and Grid Adaptation for Functional Outputs: Application to Quasi-One-Dimensional Flow," *Journal of Computational Physics*, vol. 164, 2000, pp. 204-227.

[13] O.C. Zienkiewicz and J.Z. Zhu, "A Simple Error Estimator and Adaptive Procedure for Practical Engineerng Analysis," *International Journal for Numerical Methods in Engineering*, vol. 24, 1987, pp. 337-357.

[14] T.I. Shih, X. Gu, and D. Chu, "Grid-Quality Measures and Error Estimates," *Numerical Grid Generation in Computational Field Simulations*, The International Society of Grid Generation, 2000, pp. 799-808.

[15] X. Gu and T.I. Shih, "Differentiating Between Source and Location of Error for Solution-Adaptive Mesh Refinement," *15th AIAA Computational Fluid Dynamics Conference*, AIAA Paper 2001-2660, 2001.

[16] X. Gu, H.J. Schock, T.I.P. Shih, E.C. Hernandez, and D. Chu, "Grid-Quality Measures for Structured and Unstructured Meshes," *39th Aerospace Sciences Meeting and Exhibit*, AIAA Paper 2001-0652, 2001.

[17] I. Babuska, T. Strouboulis, and C.S. Upadhyay, "A Model Study of the Quality of a Posteriori Error Estimators for Linear Elliptic Problems: Error Estimation in the Interior of Patchwise Uniform Grids of Triangles," *Computer Methods in Applied Mechanics and Engineering*, vol. 114, 1994, pp. 307-378.

[18] I. Babuska, T. Strouboulis, S.K. Gangaraj, and C.S. Upadhyay, "Pollution Error in the h-Version of the Finite Element Method and the Local Quality of the Recovered Derivatives," *Computer Methods in Applied Mechanics and Engineering*, vol. 140, 1997, pp. 1-37.

[19] L.F. Richardson, "The approximate arithmetical solution by finite differences of physical problems including differential equations, with an application to the stresses in a masonry dam," *Philosophical Transactions of the Royal Society of London, Series A*, vol. 210, 1910, pp. 307–357.

[20] N.A. Pierce and M.B. Giles, "Adjoint recovery of superconvergent functionals from PDE approximations," *SIAM Review*, vol. 42, 2000, pp. 247-264.

[21] J.H. Ferziger, "Estimation and Reduction of Numerical Error," *Symposium on Quantification of Uncertainty in Computational Fluid Dynamics*, ASME FED, vol. 158, 1993, pp. 1-8.

[22] B.P. Van Straalen, R.B. Simpson, and G.D. Stubley, "A Posteriori Error Estimation for Finite Volume Simulations of Fluid Flow Transport," *Proceedings of the 3rd Annual Conference of the CFD Society of Canada*, Banff, Alberta: 1995.

[23] X.D. Zhang, J.Y. Trepanier, and R. Camarero, "A Posteriori Error Estimation for Finite-Volume Solutions of Hyperbolic Conservation Laws," *Computer Methods in Applied Mechanics and Engineering*, vol. 185, 2000, pp. 1-19.

[24] X.D. Zhang, D. Pelletier, J.Y. Trepanier, and R. Camarero, "Numerical Assessment of Error Estimators for Euler Equations," *AIAA Journal*, vol. 39, 2001, pp. 1706-1715.

[25] Y. Qin and T.I. Shih, "A Discrete Transport Equation for Error Estimation in CFD," *40th AIAA Aerospace Sciences Meeting*, AIAA Paper 2002-0906, 2002.

[26] Y. Qin and T.I. Shih, "A Method for Estimating Grid-Induced Errors in Finite-Difference and Finite-Volume Methods," *41st Aerospace Sciences Meeting*, AIAA Paper 2003-0845, 2003.

[27] Y. Qin and T.I. Shih, "Analysis and Modeling of the Residual in the Discrete Error Transport Equation," *16th AIAA Computational Fluid Dynamics Conference*, AIAA Paper 2003-3850, 2003.

[28] Y. Qin, P.S. Keller, R.L. Sun, E.C. Hernandez, C.Y. Perng, N. Trigui, Z. Han, F.Z. Shen, T. Shieh, and T.I. Shih, "Estimating Grid-Induced Errors in CFD by Discrete-Error-Transport Equations," *42nd Aerospace Sciences Meeting*, AIAA Paper 2004-0656, 2004.

[29] Y. Qin, X. Chi, and T.I. Shih, "Modeling the Residual in Error-Transport Equations for Estimating Grid-Induced Errors in CFD Solutions," *44th AIAA Aerospace Sciences Meeting and Exhibit*, AIAA Paper 2006-0892, 2006.

[30] T.I. Shih and Y.C. Qin, "A Posteriori Method for Estimating and Correcting Grid-Induced Errors in CFD Solutions Part 1: Theory and Method," *45th AIAA Aerospace Sciences Meeting and Exhibit*, AIAA Paper 2007-100, 2007.

[31] Y. Qin, X. Chi, and T. Shih, "Estimating Grid-Induced Errors in Navier-Stokes Solutions by Euler Discrete-Error-Transport Equations," *43rd AIAA Aerospace Sciences Meeting*, AIAA Paper 2005-0567, 2005.

[32] I. Celik and G. Hu, "Single Grid Error Estimation Using Error Transport Equation," *Journal of Fluids Engineering*, vol. 126, 2004, pp. 778-790.

[33] C.J. Roy, A. Raju, and M.M. Hopkins, "Estimation of Discretization Errors Using the Method of Nearby Problems," *AIAA journal*, vol. 45, 2007, p. 1232.

[34] C.J. Roy and A.J. Sinclair, "On the Generation of Exact Solutions for Evaluating Numerical Schemes and Estimating Discretization Error," *Journal of Computational Physics*, vol. 228, 2009, pp. 1790-1802.

[35] C.J. Roy, "Strategies for Driving Mesh Adaptation in CFD," *47th AIAA Aerospace Sciences Meeting*, AIAA Paper 2009-1302, 2009.

[36] V.V. Rusanov, "Calculation of the interaction of unsteady shock waves with obstacles," *J. Comput. Math. and Math. Phys. (USSR)*, vol. 1, 1961, pp. 267-279.

[37] Z.J. Wang, "A Quadtree-Based Adaptive Cartesian/Quad Grid Flow Solver for Navier-Stokes Equations," *Computers & Fluids*, vol. 27, 1998, pp. 529-549.

[38] T.J. Chung, *Computational Fluid Dynamics*, Cambridge University Press, 2002.

Acknowledgements

I would like to thank Dr. Tom I-P. Shih for his guidance during my graduate career, as well as my committee members who have been valuable resources and teachers: Dr. Mark Bryden, Dr. Ambar Mitra, Dr. Thomas Rudolphi, and Dr. Zhi J. Wang. Thank you also to my wife, Kelly, and my family for their support and encouragement during my research and writing this dissertation.

This work has been partially funded by the National Energy Technology Laboratory of the Department of Energy with Charles Alsup and Rich Dennis as technical monitors. I am grateful for this support.